UNIVERSITY OF GHANA, LEGON

SYNTHESIS AND CHARACTERIZATION OF CUPRIC OXIDE NANOPARTICLES FOR PHOTOVOLTAIC APPLICATIONS

BY

ALFRED ATO YANKSON

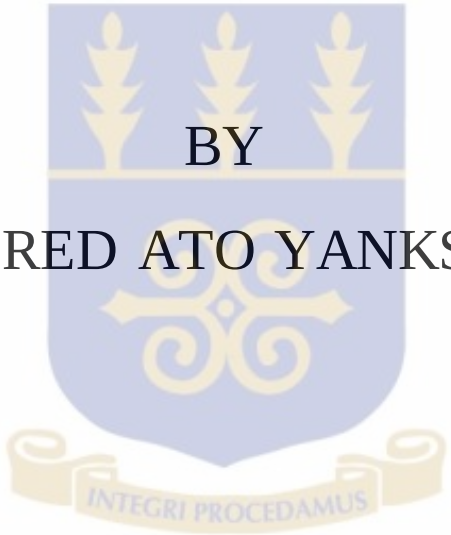

This thesis is submitted to the University of Ghana, Legon in partial fulfillment of the requirements for the award of PhD Physics degree

MARCH 2015

DECLARATION

Candidate's Declaration

I hereby declare that except for references to work by others, which have been duly cited, this thesis is the result of my own research and that it is neither in part nor whole been presented for the award of any degree elsewhere.

……..

CANDIDATE: ALFRED ATO YANKSON

DATE: ……

……

DR. A. KUDITCHER

DATE: ……

……

PROF. J. K. A. AMUZU

DATE: ……

……

DR. G. G. HAGOSS

DATE: ……

ABSTRACT

A simple inexpensive chemical route has been identified and used to synthesize cupric oxide nanoparticles suitable for photovoltaic applications. X-ray diffraction analysis showed the synthesized nanoparticles to be a pure cupric oxide phase. The particle size and particle size distribution of the cupric oxide nanoparticles were obtained by transmission electron microscopy (TEM) whereas the crystallite size and crystallite size distribution were obtained by X-ray diffraction peak broadening analysis. The particle size was found to be between 20 nm and 60 nm, an indication that cupric oxide nanoparticles are dominant in the sample produced and analysed. The particle size distribution obtained from cumulative percentage frequency plots features a log-normal function. Absorbance measurements and analysis show that the material has an absorbance peak around 314 nm and an average energy bandgap of 1.48 eV, making it a good candidate for photovoltaic applications. A thin film of average thickness of 1.47 microns made, was used to determine the conductivity of the material, which is $8.541 \times 10^{-2}\ \Omega^{-1}\text{cm}^{-1}$. Incident radiation of various wavelengths from the highest (600 nm) to the lowest (300 nm), caused decrease in resistance of the thin film sample, an indication that the material responds favourably to visible radiation making it suitable for photovoltaic and photo electronic applications. We emphasize that a low cost approach has been used successfully to synthesize cupric oxide nanoparticles with the suitable optical and electrical properties required for application in the photovoltaic and photo electronic industries.

ACKNOWLEDGEMENTS

I wish to thank my supervisors at the Department of Physics, namely, Dr. A. Kuditcher, Prof. J. K. A. Amuzu, and Dr. G. G. Hagoss for all the guidance, encouragement and the support they gave. I am grateful to the Carnegie Next Generation of Academics in Africa Project for funding this work; I am personally indebted to Prof. Yaa Ntiamoa-Baidu, Director of the Carnegie Next Generation of Academics in Africa Project, and I thank Dr. G. K. Nkrumah-Buandoh for the part he played as Head of Department in making the Carnergie grant possible. I am full of appreciation for the contributions made by Professors; K. G Adanu, R. B. Baeta and K. Oduro-Afriyie.

I am grateful to Dr. M. N. Y. H. Egblewogbe, former lab mate, for all the cooperation and to Dr. M. K Addae-Kagyah for offering to support this work in his own style. I appreciate all the support I enjoyed from all senior members at the Department of Physics, University of Ghana. The technicians at the department, led by the Chief Technician, Mr. Harry Ntumi, cooperated and helped in many ways in getting the work done; to all of them I say thank you.

The electron microscopy department at the Nuguchi Memorial Institute for Medical Research gave me access to the transmission electron microscope. I express my appreciation to all the technicians there, headed by Mr. Doudu.

To God be the Glory, great things He has done.

DEDICATION

This thesis is dedicated to Prof. and Mrs. E. K. Agyei and to Dr. A. Kuditcher.

To God be the Glory

TABLE OF CONTENTS

CHAPTER TWO: BAND THEORY, ELECTRICAL CONDUCTION AND THE SOLAR CELL

LIST OF FIGURES

Figure

List of Symbols

Symbols

γ	Surface energy	1.2
ε	The energy equivalent for the atom to return to its original position	1.3
Ω	Atomic volume	1.7
$\Delta\mu$	Work done per atom transferred	1.8
μ_r	The chemical potential of a vapour atom	1.11
μ_∞	The chemical potential of an atom on a flat surface	1.11
P_∞	The equilibrium vapour pressure of the flat solid surface	1.11
K	Boltzmann constant	1.11
μ_c	The chemical potential of an atom on a curved surface	1.12
P_c	The equilibrium vapour pressure	1.12
S_c	Solubility of a curved surface	1.16
S_∞	Solubility of flat surface	1.16
E	Electrical charge density	1.18
E_0	Standard electrode potential when concentration of ions is unity	1.18
Φ_R	Electrostatic repulsion between two equally sized spherical particles	1.23

Φ_A	Vander Waals attraction	1.25
U_{ng}	Thermal equilibrium rate	2.17
τ_n	Lifetime of electrons in the steady state regime	2.27
τ_p	Lifetime of holes in the steady state regime	2.27
n_c^{ind}	Excess electrons in the conduction band induced by absorption of light	2.51
E_+^{sw}	Incident energy on a solar cell	2.55
R_{SH}	Shunt resistance	2.60

CHAPTER 1

INTRODUCTION

1.1 Overview

Energy is important in all activities of life and the energy consumption rate of a society is correlated with the quality of life members of that society enjoy. Both advanced and emerging economies have depended on conventional sources of energy, which are associated with environmental pollution, global warming with its attendant dangers, and sustainability concerns. Although renewable energy resources are unlimited and renewable energy does not irreparably harm the environment, the present global energy mix incorporates only a small fraction of renewable sources, as can be seen in figure 1, which shows the sources of energy for the year 2006 [1].

In 2011, the International Energy Agency reported that "the development of affordable, inexhaustible and clean solar energy technologies will have huge longer-term benefits. It will increase countries' energy security through reliance on an indigenous, inexhaustible and mostly import-independent resource, enhance sustainability, reduce pollution, lower the costs of mitigating climate change, and keep fossil fuel prices lower than otherwise." [2]

A clean energy source is one that contributes a negligible amount of greenhouse gases into the atmosphere. It barely contributes other pollutants into the atmosphere, therefore it is more preferred to other sources of energy which heavily pollute the atmosphere. This advantage of environmental friendliness continues to make clean energy sources very attractive to Governments, businesses and researchers. Imperatively, enormous efforts are being put into developing and harnessing clean

energy sources all over the globe. Clean energy sources are referred to as renewable or nonconventional. The development of these possibly holds the key to unlocking the energy potential of the earth to meet the ever-growing energy need to sustain civilization. Among renewable energy sources, solar energy stands out with

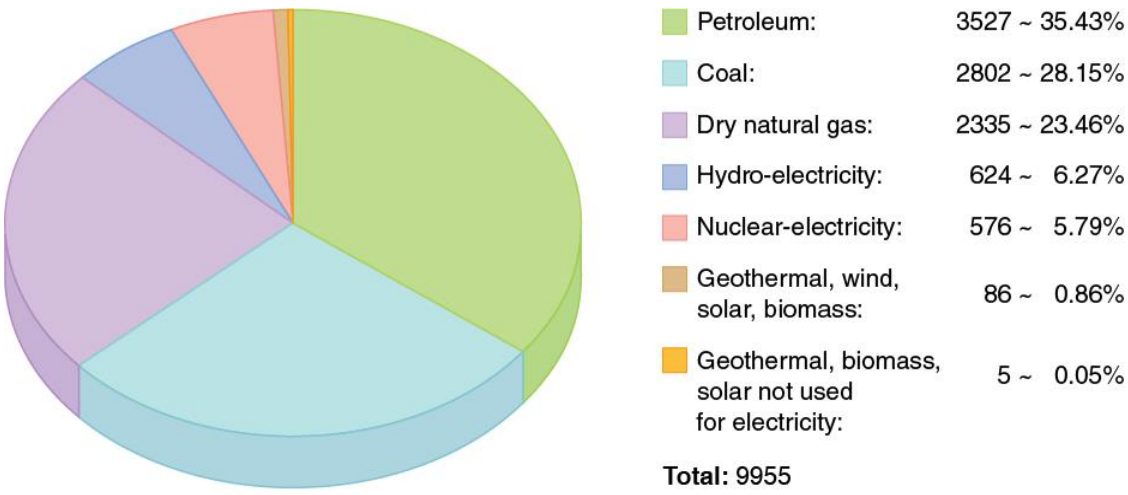

Figure 1: A pie chart showing percentage contributions of various sources of energy to the world's energy consumption for 2006 [1]. The figures are in units of billions of kilowatt hours.

prominence, pointing to a future of clean, affordable, and sustainable electricity production.

According to the International Energy Agency (IEA) in its 2012 edition of the *World Energy Outlook*, it is becoming increasingly difficult and expensive to restrict global warming to 2 °C with each passing year and if action is not taken before 2017, energy infrastructure existing in 2017 will account for all the permissible CO_2 emissions [3].

The quest for sustainable energy must go hand in hand with the fight against environmental pollution; it is therefore imperative to pay attention to energy sources

that are less polluting in contemporary situations. For many centuries, man has depended on energy from the sun for heating, warming and drying. It is fitting that the sun must again play a central role in efforts to address the energy sustainability and environmental issues that confront contemporary society

The sun is a medium yellow star, with hydrogen accounting for almost its entire volume. The hydrogen is at such high temperatures as to cause nuclear fusion. Four hydrogen nuclei combine to produce a helium nucleus, with the release of some radiation. In this process, deuterons are formed when two pairs of protons fuse. The deuterons fuse again with protons resulting in the formation of helium-3. If two helium-3 nuclei combine or fuse, a beryllium-6 nucleus is achieved. This final nuclide is so unstable that it splits up into a helium-4 nucleus and two protons.

$$\begin{aligned} {}^{1}\mathrm{H} + {}^{1}\mathrm{H} &\rightarrow {}^{2}\mathrm{H} + \beta^{+} + \nu \\ {}^{2}\mathrm{H} + {}^{1}\mathrm{H} &\rightarrow {}^{3}\mathrm{He} + \gamma \\ {}^{3}\mathrm{He} + {}^{3}\mathrm{He} &\rightarrow {}^{4}\mathrm{He} + {}^{1}\mathrm{H} + {}^{1}\mathrm{H} \end{aligned} \qquad 1.1$$

Equation 1.1 summarizes the nuclear fusion process that occurs in the sun.

The net effect of the process is thus the production of two neutrons, two positrons, and gamma rays and the energy released is accounted for by the mass difference between the helium nucleus and the four hydrogen nuclei through the well-known mass-energy equivalence $E = mc^2$ and represents a tremendous amount of energy. Table 1 shows some properties of the sun [4].

Figure 2 shows the incoming radiant solar energy and the processes that account for its removal from the earth [5]. It can be seen that about 174 PW of solar radiation

reaches the upper atmosphere. This radiation has a spectrum which is nearly that of a blackbody at a temperature of about 5800 K. The radiation reaching the surface of the earth is modified by scattering in the atmosphere and approximately 30% of the total insolation is returned to space.

Solar radiation reaching the surface of the earth can be harnessed for the production of electricity in two ways: either through a solar thermal power plant or by means of photovoltaic devices. In a solar thermal power plant, energy from the sun is used to raise steam, which is utilized by heat engines to generate electricity. Here,

Table 1: Some bulk parameters of the sun [4].

Parameter	Value
Mass	1.9885×10^{30} kg
Volume	1.412×10^{18} km^3
Mean density	1.408×10^{3} kg/m^3
Luminosity	3.846×10^{26} J/s
Mean energy production	1.937×10^{-4} J/kg
Surface emission	6.329×10^{7} J/ m^2 s
Central temperature	1.571×10^{7} K

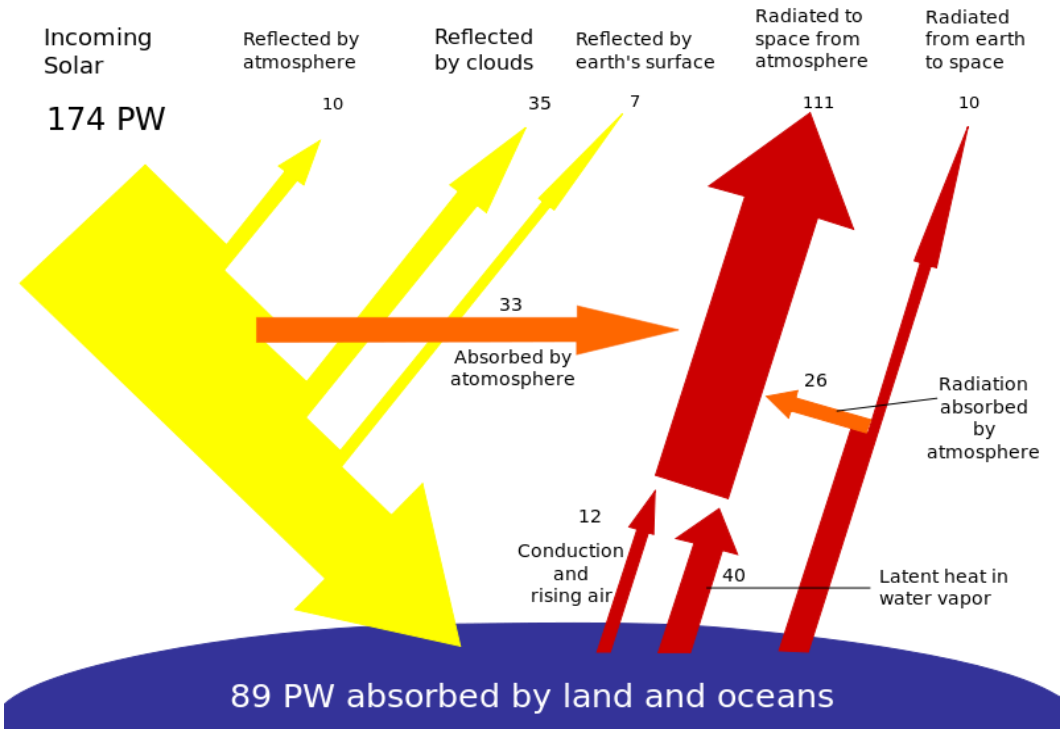

Figure 2: Breakdown of incoming solar energy in petawatt (10^{15} watts). Each number is in petawatt and represents a certain percentage of the total incoming solar energy [5].

solar concentrators are used to focus radiation from the sun to a point or along a line (usually a metal tube) containing water for the production of steam. The radiation from the sun reaching the earth is converted into thermal energy corresponding to temperatures in the range of between 200 ℃ and 1000 ℃ via concentrating parabolic dish systems at large-scale solar fields. Heat engines with steam turbines coupled to a generator convert the heat energy of the steam to electricity. It has to be mentioned that this system of power generation from a renewable source can be said not to be intermittent because of the fact that the steam generated can be stored in a relatively inexpensive manner and used when necessary to produce need-based electricity.

Photovoltaic (PV) solar power production involves conversion of solar radiation into electricity using photovoltaic devices. Photovoltaic power systems employ solar panels containing semiconductor photovoltaic cells. The world is increasingly turning its attention to photovoltaic power because of its non-depleting source of energy and because it helps bring down the levels of greenhouse gases in the atmosphere. Photovoltaic power is also useful for supporting activities such as health delivery, education and lighting in very remote parts of the world due to its ease of handling after installation, with little or no skill required at all, and its potential for realizing stand-alone systems.

Photovoltaic systems hold the potential to increase the world's energy fraction of clean energy. The International Energy Agency has indicated that by 2012, the world solar PV installed capacity had risen by 50% per year over the last decade. In 2013, the total installed capacity of solar PV capacity increased by 43% or 29.4 GW, representing 15% of total growth in global power generation capacity. Germany alone accounted for more than one quarter of the increase with 7.6 GW of additions. Other countries with major additions include Italy (3.6 GW), China (3.5 GW), USA (3.3 GW), Japan (2.0 GW), and India (1.1 GW) [6].

Energy conversion and charge collection in a PV cell determine its efficiency. These are higher in PV devices based on inorganic materials due to better tolerance of inorganic materials to upward surges in temperature during operation. Solar cells made from inorganic nanomaterials can produce heterojunction cells with an advantage that the photo-generated charge carriers travel short distances that can be smaller than the carrier diffusion length, thereby reducing the incidence of carrier recombination which is a major factor affecting the efficiency of solar cells [7].

Nanomaterials hold a promise for ushering in a new era of high-performance devices that can mitigate the environmental cost associated with the processing of conventional solar PV devices. Consequently, it is of paramount importance to appreciate the technology of nanomaterials, the contributions they can make to solving some of the pressing energy and environmental problems, and their limitations. In the rest of this chapter, a general description of nanotechnology together with synthesis approaches and their challenges is presented. This is followed by the objectives of the work presented in this thesis.

1.2 Nanotechnology

Nanotechnology comprises the study and understanding of fundamentals of physics, chemistry, biology and technology at the nanometer scale and the application of nanometer scale structures in various fields to positively affect human life. The manipulation of materials at the nanometer scale brings about different properties as compared to the bulk material. The difference between the behavior of material in bulk and the behavior of the same material at the nanometer scale is the reason for the interest in the study of nanoscale structures. The applications of nanotechnology span a wide spectrum of human endeavour including medicine, electronics, food, fuel cells, underground water purification, chemical sensors, and the fabrication of solar cells.

Bulk inorganic materials are heavy and have a small surface to volume ratio, which make the use of bulk inorganic materials in the fabrication of solar cells problematic. At the nanometer scale, the same material will have a very large surface to volume ratio, which means that more electrons will be involved in photoelectric interaction,

the basic mechanism underlying the operation of a solar cell. Nanometer size also means short propagation distance compared to carrier diffusion length for the photo ejected charge carriers, leading to low recombination rate and thereby improving the conversion rate of the solar cell. The small size also means that solar cells produced from such materials are lighter, which is good for portable and mobile electronic and electrical gadgets that depend on such cells for electrical power.

Nanotechnology brings about the reduction of the size of bulk materials, inducing size-dependent effects arising from:

- a significant increase of the surface to volume ratio involving a huge increase of the interfacial area and of the fraction of the species at the surface;
- a change of the physico-chemical properties of the species at the surface and in the nanoparticle interior in comparison with that in the bulk or with isolated molecules of the material;
- changes of the electronic structure of the species composing the nanoparticle and the nanoparticle as a whole;
- changes in the arrangement (lattice structure, interatomic distances) of the species in the nanoparticle and presence of defects;
- and confinement and quantum-size effects (due to confinement of charge carriers in a particle having a size comparable with the electron or hole de Broglie wavelength).

The fabrication and processing of nanomaterials is the paramount step in nanotechnology. Nanostructured materials are those with at least one dimension falling within the nanometer scale. They include nanoparticles, nanorods, and nanowires. Many technologies exist for the fabrication of nanostructures and nanomaterials. These

technologies can be grouped in several ways. One of the fruitful ways is to group them by the phase of the growth media: vapour phase growth, liquid phase growth, solid phase formation, and hybrid growth. The synthesis of nanomaterials can further be classified into bottom-up and top-down approaches. The bottom-up approach has been known and used in materials synthesis for many years. In this approach, the material is built up from the bottom: atom-by-atom, molecule-by-molecule, or cluster –by-cluster. The bottom-up approach provides a better chance to produce nanostructures with fewer defects, improved homogenous chemical composition, and better short- and long-range order. The bottom-up approach is facilitated by the reduction of Gibbs free energy such that the nanomaterials and nanostructures so produced are in a state very close to thermodynamic equilibrium. The top-down approach entails trimming down the size of materials to obtain nanostructures. An exemplary process in this approach is attrition or milling. This approach has a surface imperfection challenge. It is well known that the conventional top-down techniques such as lithography can cause crystallographic damage to the processed patterns and additional defects may be introduced during etching steps. [8, 9].

No single synthesis type exists that is best for all nanomaterials or for all applications. To select the most suitable synthesis route that suits a specific nanomaterial for a given purpose, a good knowledge of the challenges associated with synthesis of nanomaterials in general is needed. The challenges associated with the synthesis of nanomaterials can be traced to the large surface energy due to the enormous surface to volume ratio, Ostwald ripening, and challenges associated with obtaining a desired size, size distribution, morphology, crystallinity, and chemical composition which

taken together result in desired physical properties. Issues surrounding surface energy and chemical potential are considered in turn.

1.2.1 Surface energy

On a solid surface, atoms or molecules have fewer nearest neighbours or coordination numbers than atoms or molecules within the interior of the solid. This leads to dangling bonds on the surface, and surface atoms or molecules are subject to a force directed inward. The bond length between surface atoms or molecules and subsurface atoms or molecules is smaller than that between interior atoms or molecules. When a solid particle is small, such a decrease in bond length between the surface atoms and interior atoms becomes very significant and the leads to a pronounced reduction in the lattice constant of the entire solid particle. All of these lead to increased excess surface energy for the surface particles of nanoparticles [10].

It is well known that the energy associated with atoms or molecules on the surface of a solid or liquid is different from that associated with atoms or molecules within the bulk. Surface energy is defined by

$$\gamma = \left[\frac{\partial G}{\partial A}\right]_{n_i,T,P} \qquad 1.2$$

and represents the energy required to create an element of surface [11]. In equation 1.2, A is the surface area, G is the Gibbs free energy, T is temperature and P is pressure. Consider a rectangular solid subdivided into two pieces as shown in figure 3. On the newly created surfaces, the surface atoms are subject to forces directed towards the

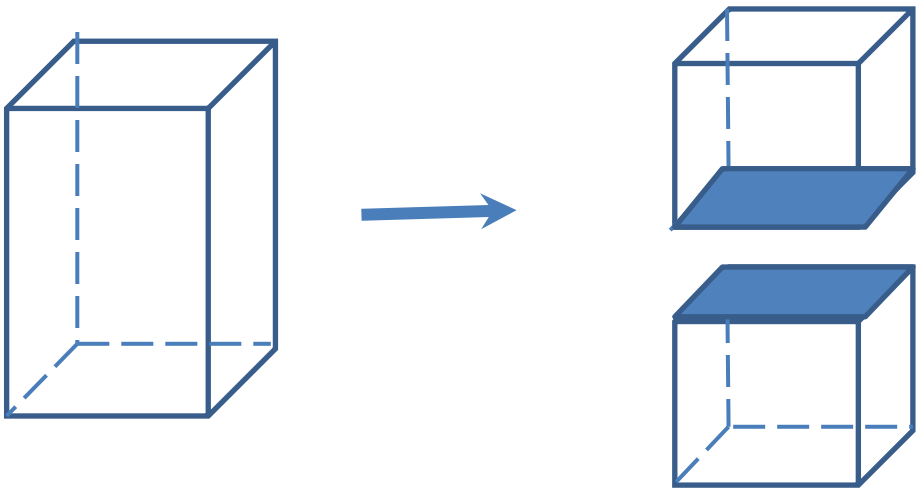

Figure 3. Schematic drawing showing two new surfaces created by breaking a rectangle into two pieces.

bulk. The energy required to get the surface atoms back to their original positions is given by the surface energy

$$\gamma = \frac{1}{2} N_b \varepsilon \rho_a \qquad 1.3$$

where half the bond strength ε is equivalent to the energy required to get the atom back to its original position, N_b is the number of broken bonds, and ρ_a is the surface atomic density, the number of atoms per unit area in the new surface. This assumes that the value of ε is the same for surface and bulk atoms, ignoring contributions from higher order neighbours. Equation 1.3 gives a rough estimate of the true surface energy of a solid surface and is only applicable to rigid solids. Surface relaxation will lead to a surface energy less than what has been estimated by the equation above.

Consider an elemental crystal with a face-centered cubic (fcc) structure and lattice constant a as an example for illustrating the surface energy on various facets.

Each atom in the FCC structure has a coordination number of 12, and those on the (100) planes have four broken bonds. The surface energy of a (100) plane can be obtained using equation 2:

$$\gamma_{\{100\}} = \left(\frac{1}{2}\right)\left(\frac{2}{a^2}\right)4\varepsilon = \frac{4\varepsilon}{a^2} \qquad 1.4$$

In the same manner, each atom on a (110) surface has five broken chemical bonds, each atom on a (111) surface has three and the respective surface energies for these planes are thus

$$\gamma_{\{110\}} = \frac{5}{\sqrt{2}}\frac{\varepsilon}{a^2} \qquad 1.5$$

and

$$\gamma_{\{111\}} = \frac{2}{\sqrt{3}}\frac{\varepsilon}{a^2} \qquad 1.6$$

Low index facets have low surface energy according equation 1.3.

Thermodynamically, materials are stable only when they are in a state with the lowest Gibbs free energy.

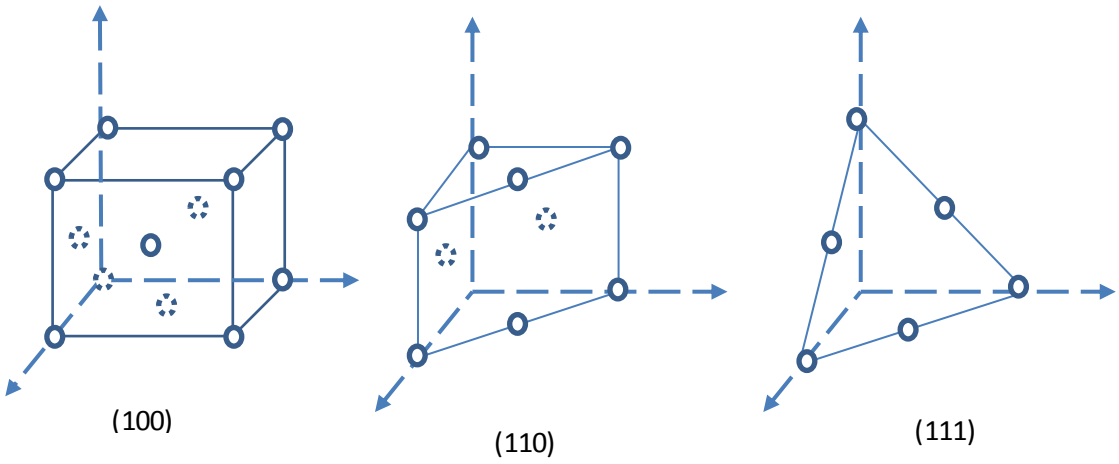

Figure 4. Schematic diagram of low index facets of face-centered cubic (FCC) crystal structure [11].

Several mechanisms that reduce the overall surface energy, and hence minimize the free energy, can be identified and can be grouped into atomic, individual structure, and the overall system mechanisms. Surface relaxation is an example of an atomic level mechanism. Surface relaxation shifts surface atoms or ions inward into the bulk. This mechanism for surface energy reduction occurs more readily in the liquid phase than in the solid surface. Surface restructuring occurs through combining surface dangling bonds into strained new chemical bonds. Surface adsorption through chemical or physical adsorption of terminal chemical species onto the surface by forming chemical bonds or weak van der Waals forces and composition segregation or impurity enrichment on the surface through solid-state diffusion both lead to surface energy reduction.

At the overall system level, mechanisms for reducing the overall surface energy include individual nanostructures combining to form large structures to reduce the overall surface area, if sufficient activation energy exists for such a process to occur and agglomeration of individual nanostructures without altering the individual

nanostructures. Specific combination mechanisms for getting individual nanostructures to form large structures include sintering, in which individual structures merge and Ostwald ripening, in which relatively large structures grow at the expense of small structures. Figure 5 illustrates the two processes.

Sintering is pronounced at temperatures above room temperature and it is significant when materials are heated to elevated temperatures of about 70% of the melting point of the given material. Ostwald ripening occurs over a wide range of temperatures, and proceeds at relatively low temperatures when nanostructures are dispersed in a solvent in which they have appreciable solubility.

Sintering must be avoided in the synthesis of nanomaterials. Though sintering is significant at high temperatures, the small size of a nanoparticle implies a high surface energy and sintering can be of great concern even when the nanomaterials are brought to moderate temperatures. Sintering involves solid-state diffusion, evaporation-condensation or dissolution-precipitation, viscous flow and dislocation creep.

The product of sintering is a polycrystalline material, whereas Ostwald ripening produces a single uniform structure. At the macroscopic level, the reduction in total surface energy is the driving force for both sintering and Ostwald ripening. Microscopically, the differential surface energy of surfaces with different surface curvature is the driving force for the mass transport during sintering and Ostwald ripening.

Agglomeration is another way to reduce surface energy. Many nanostructures associate with one another in what is called agglomerates through chemical bonds and physical attraction forces at interfaces.

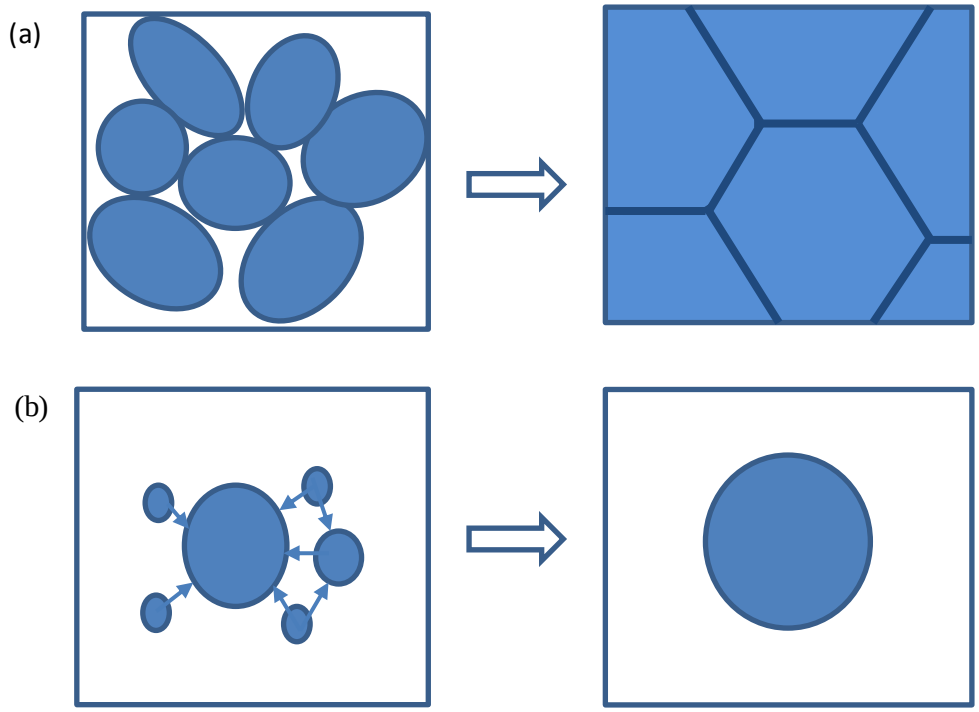

Figure 5. Schematic diagram demonstrating sintering and Ostwald ripening processes. (a) Sintering operates to combine individual particles to a bulk with solid interfaces to connect each other. (b) Ostwald ripening operates to merge smaller particles into a larger particle [11].

Chemical potential

The properties of surface particles differ from those of the interior particles due to the smaller number of bonds linking them to their nearest neighbours compared with the interior particles. Chemical potential is also dependent on the curvature of the particle surface. The transfer of material from an infinite flat surface to a spherical solid surface illustrates this.

If dn atoms are transferred from the flat solid surface to a particle of radius R, the volume change dV of the spherical particle is equal to the atomic volume Ω multiplied by dn; that is,

$$dV = 4\pi R^2 dR = \Omega dn \quad 1.7$$

The work per atom transferred, $\Delta\mu$, equals the change in chemical potential, and is given by

$$\Delta\mu = \mu_c - \mu_\infty = \gamma \frac{dA}{dn} = \gamma 8\pi R\Omega . \frac{dR}{dV} \quad 1.8$$

Combining the two equations 1.7 and 1.8 above leads to

$$\Delta\mu = \frac{2\gamma\Omega}{R} \quad 1.9$$

Equation 1.9 is known as the Young-Laplace equation. It describes the chemical potential of an atom in a spherical surface with respect to a flat reference surface. The equation can be generalized for all types of curved surfaces. Any curved surface can be described by two principal radii of curvature, R_1 and R_2 [10]. Equation (8) can therefore be written as

$$\Delta\mu = \gamma\Omega \left(R_1^{-1} + R_2^{-1}\right) \quad 1.10$$

The curvature is positive for a convex surface, thus the chemical potential of an atom on a convex surface is higher than that on a flat surface. Mass transfer to a convex surface from a flat surface brings about an increase in surface chemical potential. The surface chemical potential decreases when the transfer is from a flat surface to a concave surface. Thermodynamically, an atom on a convex surface possesses the highest surface chemical potential. This phenomenon is reflected by the difference in vapour pressure and solubility of a solid.

Let us assume the vapour of solid phase obeys the ideal gas law. For the flat surface we can write

$$\mu_v - \mu_\infty = kT \ln P_\infty \quad 1.11$$

where μ_v is the chemical potential of a vapour atom, μ_∞, the chemical potential of an atom on the flat surface, k, the Boltzmann constant, P_∞, the equilibrium vapour pressure of the flat solid surface , T, temperature.

In a similar manner, for a curved surface we have:

$$\mu_v - \mu_c = kT \ln P_c \quad 1.12$$

where μ_c, the chemical potential of an atom on the curved surface, and P_c, the equilibrium vapour pressure of the curved solid surface.

From equations (1.11) and (1.12) we obtain:

$$\mu_c - \mu_\infty = kT \ln \frac{P_c}{P_\infty} \quad 1.13$$

Combining with equation (1.10) and rearranging gives us:

$$\ln \frac{P_c}{P_\infty} = \frac{\gamma\Omega\,(R_1^{-1} + R_2^{-1})}{kT} \quad 1.14$$

For a spherical particle, equation (1.14) can be simplified as:

$$\ln \frac{P_c}{P_\infty} = \frac{2\gamma\Omega}{kRT} \quad 1.15$$

Equation 1.15 is generally and commonly called the Kevin equation and has been verified experimentally. [9]

The same relation can be derived for the dependence of the solubility on surface curvature:

$$\ln \frac{S_c}{S_\infty} = \frac{\gamma\Omega\,(R_1^{-1} + R_2^{-1})}{kT} \qquad 1.16$$

where S_c is the solubility of a curved solid surface, S_∞, the solubility of a flat surface. This equation is also known as Gibbs-Thompson relation. [10]

When two particles with different radii, assuming $R_1 \gg R_2$, are put into a solvent, each particle will develop an equilibrium with the surrounding solvent. According to equation (1.16), solubility of the smaller particle will be larger than that of the larger particle. There would be a net diffusion of solute from the region of the smaller particle to the region of the larger particle. For the equilibrium to be maintained, solute will deposit unto the surface of the large particle, whilst the small particle will have to continue dissolving to compensate for the amount of solute diffused away. This leads to the small particle becoming smaller, while the large particle gets larger.

This is Ostwald ripening, which occurs also in the forms of solid-state diffusion and evaporation-condensation. Assuming there is no other change between the two particles, then the change of the chemical potential of an atom transferring from a spherical surface of radius R_1 to R_2 is given by:

$$\Delta\mu = 2\gamma\Omega(R_2^{-1} - R_1^{-1}) \qquad 1.17$$

Depending on the target parameters, Ostwald ripening can have either positive or negative influence on the material synthesized. It can narrow or widen the size distribution, based on the control of the process conditions. Ostwald ripening has been explored in the preparation of nanoparticles. It is used to narrow size distribution of nanoparticles.

Ostwald ripening is promoted by varying processing temperatures. During the preparation of nanoparticles from solution, after the initial nucleation and subsequent growth, when temperature is raised, the solubility of solute in solvent rises to promote Ostwald ripening.

1.2.2 Electrostatic Stabilization

Surface charge density

A solid emerging from a polar solvent or an electrolyte solution will develop surface charge through one or more of the following mechanisms:

1. Preferential adsorption of ions

2. Dissociation of surface charged species

3. Accumulation or depletion of electrons at the surface

4. Physical adsorption of charged species onto the surface

5. Isomorphic substitution of ions.

A fixed surface electrical charge density (electrode potential), E, is established for a given solid surface in some liquid medium. The electrical charge density E is given by the Nernst equation:

$$E = E_0 + \frac{RT}{n_i F}\ln(a_1) \qquad 1.18$$

where E_0 is the standard electrode potential when the concentration of ions is unity, n_i is the valence state of the ions, R is the gas constant , T is temperature, and F is Faraday's constant.

From equation (1.18), it is obvious that the surface potential of a solid varies with the concentration of the ions in the surrounding solution, and can either be positive or negative.

The surface charge in oxides is mainly derived from preferential dissolution or deposition of ions. [11] In the oxide systems typical charge determining ions are protons and hydroxyl groups and their concentrations are determined by pH (pH = -log $[H^+]$). As the concentration of the charge determining ions varies, the surface charge density changes from positive to negative and vice versa. The concentration of charge determining ions corresponding to a neutral or zero-charged surface is called point of zero charge (*p.z.c*) or zero-point charge (*z.p.c*). At pH > *p.z.c*, the oxide surface is negatively charged, since the surface is covered by hydroxyl groups, OH^-, which is the electrical determining ion. At pH< *p.z.c*, the surface is positively charged and the determining ion is H^+.The surface charge density or surface potential, E, in volt, can then be simply related to pH and the Nernst equation can be written as [12]:

$$E = 2.303R_gT\frac{(p.z.c) - \mathrm{pH}}{F} \qquad 1.19$$

At room temperature, equation (1.19) can further be simplified:

$$E \approx 0.06[(p.z.c) - \mathrm{pH}] \qquad 1.20$$

1.3 Electric potential at proximity of solid surface

When the surface charge density of a solid surface is established, there will be a columbic force between the solid surface and the charged species in the proximity to segregate positive and negative charged species. There exist also Brownian motion and entropic force, which homogenize the distribution of various species in solution. In the solution there will always exist both surface determining ions (opposite charge) and counter ions. Although charge neutrality prevails in the system, distributions of charge determining ions and counter ions in the neighbourhood of the solid surface are inhomogeneous and very different. The distributions of both ions are controlled by a combination of the following forces.

1. Coulombic force

2. Entropic force

3. Brownian motion.

The concentration of counter ions is highest near the solid surface and decreases as the distance from the surface increases, with the concentration of determining ions changing in the opposite direction, assuming surface charge is positive. This kind of inhomogeneous distributions of ions, in the neighbourhood of the solid surface, leads to the formation of so called double layer structure shown in figure 7 below. The double layer comprises Stern layer and Gouy layer (diffuse double layer); these two layers are separated by the Helmholtz plane. [13]

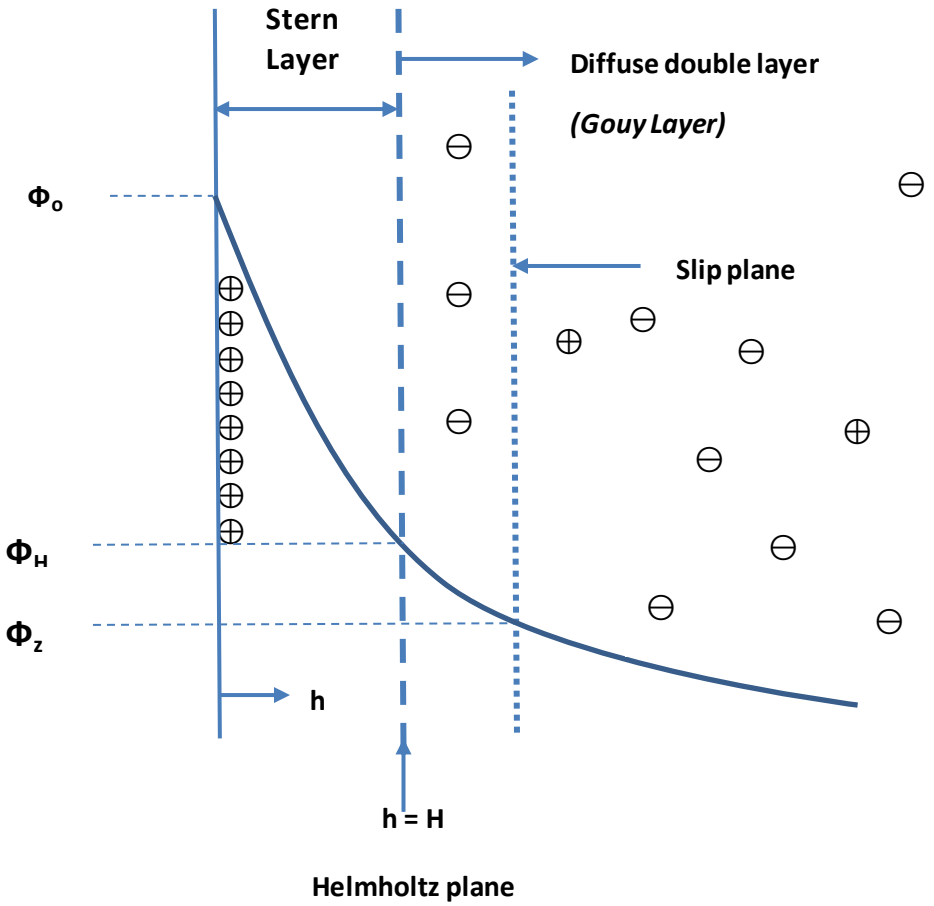

Figure 6. Schematic diagram illustrating electrical double layer structure and the electric potential near the solid surface with both Stern and Gouy layers shown. Surface charge is assumed positive.

Between the solid surface and the Helmholtz plane is the Stern layer, where the electric potential drops linearly through the tightly bound layer of solvent and counter ions. Beyond the Helmholtz plane until the counter ions reach average concentration in the solvent is the Gouy layer or diffuse double layer. In the Gouy layer, the counter ions diffuse freely and the electric potential does not reduce linearly. The electric potential drops approximately following:

$$E \propto e^{-\kappa(h-H)} \tag{1.21}$$

where $h \geq H$, which is the thickness of the Stern layer, $1/\kappa$ is known as the Debye-Hückel screening strength and is also used to describe the thickness of the double layer, κ is given by

$$\kappa = \left\{ \frac{F^2 \sum_i C_i Z_i^2}{\varepsilon \varepsilon_0 R_g T} \right\}^{1/2} \tag{1.22}$$

where F is Faraday's constant, ε_0 is the permittivity of free space, ε is the dielectric constant of the solvent, and C_i and Z_i are the concentration and valence of the counter ions of type *i*. Equation (1.22) clearly shows that the electric potential in the neighbourhood of the solid surface decreases with increased concentration and valence state of counter ions, and increases with an increased dielectric constant of the solvent exponentially. Higher concentration and valence state of counter ions results in a reduced thickness of both Stern layer and Gouy layer. [14]

The discussion above also holds for curved surfaces as well, assuming the surface is smooth such that the surface charge density is evenly distributed. For a smooth curved surface the surface charge density is constant, so the electric potential in the surrounding solution can be described by equations (1.21) and (1.22).

Interactions between particles are complex, one of these is directly associated with the surface charge and the electric potential adjacent to the interface. Electrostatic repulsion between two particles is as a result of the electric surface charges, which are attenuated to a varied extent by the double layers. When the separation between two particles is large enough, there will be no overlap of two double layers and electrostatic

repulsion between them is zero. When the particles approach each other, double layer overlaps and a repulsion develops. An electrostatic repulsion between two equally sized spherical particles is given by: [15]

$$\Phi_R = 2\pi\varepsilon_r\varepsilon_0 r E^2 \exp(-\kappa s). \qquad 1.23$$

1.31 Van der Waals attraction potential

When small particles, typically in the micrometer-range or less are dispersed in a solvent, van der Waals attraction force and Brownian motion are significant, whiles the effect of gravity becomes negligible. Van der Waals force is a weak force and it is only significant at very short distance. Brownian motion ensures that the nanoparticles collide with each other all the time. The effect of these two would result in the agglomeration of the nanoparticles.

Van der Waals interaction between two nanoparticles is the sum of the molecular interaction for all pair of molecules composed of one molecule in each particle, as well as to all pairs of molecules with one molecule in a particle and one in the surrounding medium such as solvent. Integration of all the van der Waals interactions between two molecules over two spherical particles of radius, r, separated by distance, S, as illustrated in figure 8. gives the total interaction energy or attraction potential. [16]

$$\Phi_A = -\frac{A}{6}\left\{\frac{2r^2}{S^2+4rS} + \frac{2r^2}{S^2+4rS+4r^2} + ln\left(\frac{S^2+4rS}{S^2+4rS+4r^2}\right)\right\} \qquad 1.24$$

where the negative sign indicates an attraction force between the two particles, and A is a positive constant termed the Hamaker constant, whose magnitude is of the order

of 10^{-19} to 10^{-20} J, and depends on the polarization properties of the molecules in the two particles and in the medium which separates them.

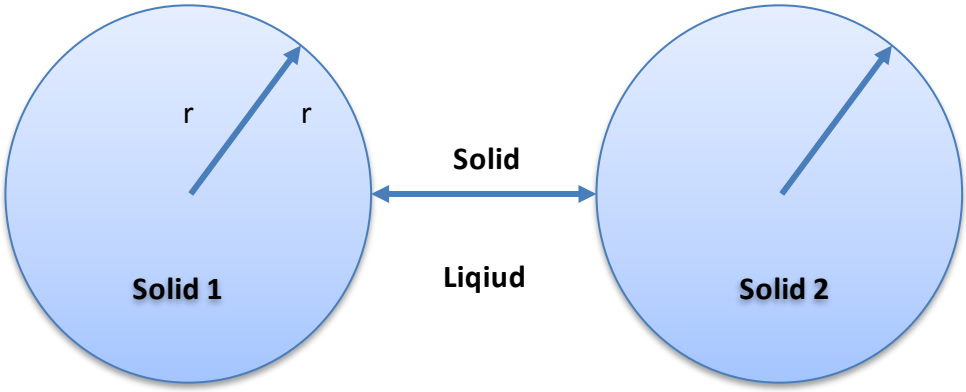

Figure 7. Pair of particles used to derive van der Waals interaction.

Under various boundary conditions, equation (1.24) can be simplified. For example, when the separation between two equal sized spherical particles is significantly smaller than particle radius, i.e., $S/r << 1$, the simplest expression for the van der Waals attraction could be obtained:

$$\Phi_A = \frac{-Ar}{12S} \qquad 1.25$$

The combination of van der Waal's attraction and electrostatic repulsion constitutes the total interaction between two particles which are electrostatically stabilized:

$$\Phi = \Phi_A + \Phi_R \qquad 1.26$$

The interaction between two particles in a suspension is considered to be the combination of van der Waal's attraction potential and electric repulsion potential.

As already pointed out, this thesis focuses on the synthesis of CuO nanoparticles. The rest of this chapter discusses the characterization of various synthesis routes that have been employed by previous researchers

Umer et al [82] categorise the approach to synthesis of nano materials into two main types; Chemical and physical approaches. Chemical reduction, micro emulsion (colloidal) technique [22], sonochemical reduction [23], electro chemical [24], microwave assisted [25], and hydrothermal [26] synthesis of nanoparticles are through the chemical approach. Biosynthesis [27] are also considered chemical processes. Physical methods for nanoparticle synthesis include; laser (pulse) ablation [28], vacuum vapour deposition [29], pulsed wire discharge (PWD) [30] and mechanical milling [31].

1.3.2 Synthesis routes

Various synthesis routes exist and have been used for the preparation of metal oxide nanoparticles, many methods have been reported for the synthesis of copper based nanomaterials[17-19].

These include the following

- sol-gel, flame spray
- vapour-phase reaction
- aqueous precipitation
- template method
- electrochemical route, sacrificial anode technique,
- laser ablation in vacuum .
- Laser ablation in liquid medium is the simplest and versatile a technique for the production of metal oxide nanomaterials [20, 21].

1.3.3 Particle size characterization of nanoparticles

The particle size and size distribution of nanoparticles induce their unique and often advantageous properties. For example, the melting point of nanoparticles is decreased when the size reaches the nanometer scale [32,33] Hence an all important task in property characterization is particle sizing [34]. In general, there are two basic methods of defining particle size[34]. One method inspects the particles and makes actual measurements of their dimensions. Microscopic techniques, for example, measure many dimensional parameters from the particle images. The second utilizes the relations between particle behaviour and its size. This often implies an assumption of equivalent spherical size developed using a size-dependent property of the particle and relating it to a linear dimension [35]. Equivalent spherical diameters are the diameters of spheres that have the same or equivalent dimensions as the irregular particles themselves. An example of this method is photon correlation spectroscopy (PCS) that the dynamic fluctuation of the scattered light intensity is the basis for the calculation of

the average particle size [36]. Particle sizes are not the same throughout the material, it is therefore required that information about the average size and the distribution of sizes about the average is obtained. The equipment used to investigate the particle size and size distribution in this study are: TEM, X-ray defractometer and reflective/ polarizing microscope.

1.4 Aims and outlook

The present work

As indicated earlier, the conventional silicon solar cells are very expensive and have rather limited efficiency. Efforts to make use of less expensive inorganic compound for the fabrication of solar cells have become the focus of intense research. These inorganic cells are more durable than the silicon cells because they do not degrade as fast with time.

The goal of this research is to contribute to obtaining durable inorganic material obtained from inexpensive sources for the fabrication of photovoltaic cells.

We have employed Cu_2SO_4 .$5H_2O$ and 30% Ammonia water for the synthesis of CuO nanoparticles using a simple chemical route in order to produce pure samples which will be suitable for PV applications.

Objectives of the work

The specific objectives of this work are;

- to synthesize CuO nanoparticles using an inexpensive simple chemical route

- to characterize the products of the synthesis by
    i. XRD
    ii. TEM
    iii. Optical absorbance
- To demonstrate through (1) absorption spectra, (2) bandgap determination and (3) voltage and current measurements that our sample can be used for the fabrication of PV cells.

The general goal of this thesis is to be able to contribute a great deal of understanding on using cheap and readily available materials to produce CuO nanoparticles, and to show that the potential exists for the use of CuO (a p-type material with narrow bandgap) nanoparticles to reduce the cost of solar cell applications since the conventional silicon cells are expensive. Inorganic solar cells are durable in that they do not degrade with temperature, it is therefore incumbent on researchers to find inexpensive suitable inorganic materials for fabricating solar cells that are more efficient and less expensive than silicon cells.

In that regard inexpensive materials that are easily obtained would be used in the synthesis of CuO nanoparticles under strict synthesis rules in order to produce pure sample which will be suitable for photovoltaic applications.

CHAPTER TWO

BAND THEORY, ELECTRICAL CONDUCTION AND THE SOLAR CELL

2.1 Electrons in a crystal

In order to understand the electrical properties of semiconductors, the behaviour of the electron in a crystal should be looked at together with the concept of energy bands.

Let us first understand how an electron behaves in a simpler environment; the classical case of the electron in a vacuum (free electron) and then the electron confined in a box-like potential well.

2.1.1 Free electron

This model looks at an electron which is not interacting with its environment: it travels in a medium where the potential is zero. This is a free electron. Let us take a look at a single crystal (one dimensional crystal), the time-independent Schrödinger equation can be written for a zero potential V;

$$-\frac{\hbar^2}{2m}\frac{d^2}{dx^2}\,\Psi(x) = E\,\Psi(x) \qquad 2.1$$

where E is the electron energy, and m the electronic mass.

Since the reference for potential is arbitrary, the potential can be set to be equal to zero $(V = 0)$ without losing generality [37]

The solution to equation (2.1) is

$$\Psi(x) = C_1 exp(ikx) + C_2 exp(-ikx) \qquad 2.2$$

where:

$$k = \sqrt{\frac{2mE}{\hbar^2}} \quad or \quad E = \frac{\hbar^2 k^2}{2m} \tag{2.3}$$

Equation (2.2) is an expression for two waves traveling in the opposite direction. The first part of the right side of the equation represents the motion of electron in the $+x$ direction, the second part of the same side gives the motion of electron in the $-x$ direction.

k is a vector belonging to the reciprocal space expressed in m^{-1} or cm^{-1}. However, in one- dimensional crystal, k can be considered as a scalar number for all practical purposes. [38]

The momentum operator, p_x , of the electron is given as

$$p_x = \frac{\hbar}{i}\frac{\partial}{\partial x}$$

For an electron moving in the $+x$ direction within a one dimensional crystal, the momentum operator is applied to the wave function $\Psi(x) = C_1 \exp(ikx)$ to obtain:

$$p_x \Psi(x) = \frac{\hbar}{i}\frac{d\Psi(x)}{dx} = C_1 \hbar k exp(ikx) = \hbar k \Psi(x)$$

The eigenvalues of the operator p_x are given by

$$p_x = \hbar k \tag{2.4}$$

The conclusion is that the number k, called the wave number, is equal to the momentum of the electron, with a factor $\hbar$.

In classical mechanics the electron has a speed v given $v = p/m$, which yields $v = \hbar k/m$. The electron energy given by equation (2.3) can thus be related to that derived from classical mechanics:

$$v = \hbar k/m \Rightarrow E = \frac{\hbar^2 k^2}{2m} = \frac{1}{2}mv^2 \qquad 2.5$$

The free electron takes any value of energy in a continuous manner in agreement with classical mechanics considerations.

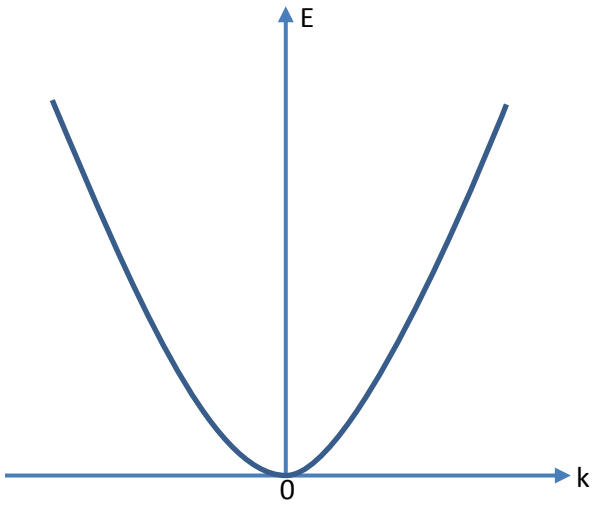

Figure 8: Showing the energy of the free electron as a parabolic function of its momentum k.

We may now consider a three dimensional crystal, in that case k is a vector of the reciprocal space. It is called the wave vector. The expression $\exp(i\boldsymbol{kr})$ gives the position of the electron, and represents a plane spatial wave moving in the direction of

k. The spatial frequency of the wave is equal to k, and the spatial wavelength is given by

$$\lambda = \frac{2\pi}{|\boldsymbol{k}|}$$

2.1.2 The particle in a box

We consider an electron that is confined by placing it in an infinitely deep potential well from which it cannot escape. The particle in a box scenario resembles, to a limited extent, an electron in an atom under attraction from the positive nucleus creating a potential well trapping the electron.

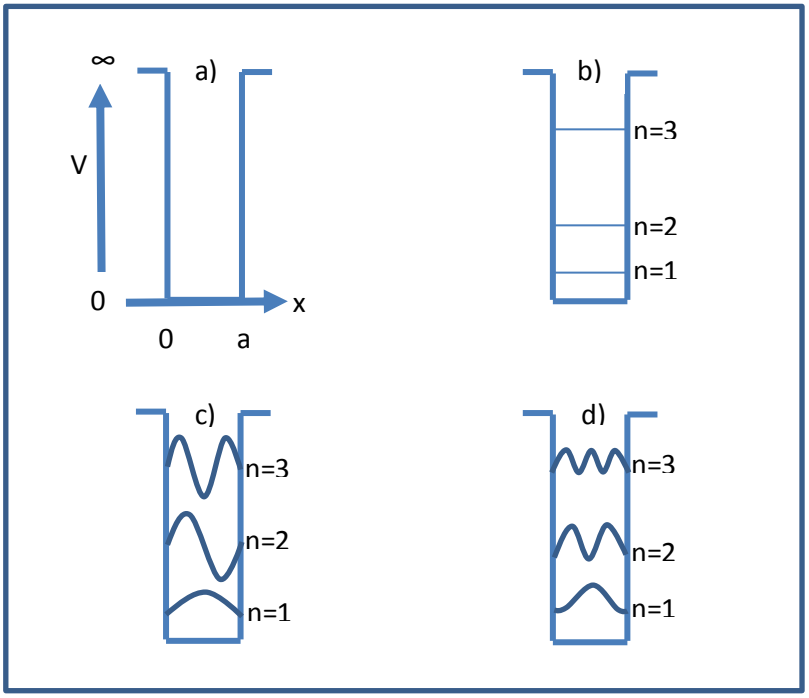

Figure 9: Particle in a box: a) Geometry of potential well; b) Energy levels; c) Wave functions; and d) Probability

The wave function of the electron confined inside the potential well, vanishes at the edges of the well. Therefore the boundary conditions to the problem are :$\Psi(x \leq 0) = \Psi(x \geq a) = 0$. Inside the potential well $(0 \leq x \leq a)$, where $V = 0$, the time independent Schrödinger equation can be written as:

$$-\frac{\hbar^2}{2m}\frac{d^2(x)}{dx^2} = E\Psi(x) \qquad 2.6$$

which can be rewritten in the following form:

$$\frac{d^2\Psi(x)}{dx^2} + k^2\Psi(x) = 0 \; with \; k = \sqrt{2mE/\hbar^2} \;\; or \; E = \frac{\hbar^2 k^2}{2m} \qquad 2.7$$

The solution to this homogenous, second-order differential equation is:

$$\Psi(x) = Asin(kx) + Bcos(kx) \qquad 2.8$$

From the first boundary condition $\Psi(x = 0) = 0$ we obtain $B = 0$, the second boundary condition $\Psi(a) = 0$ gives $Asin(ka) = 0$ thus:

$$k = \frac{n\pi}{a} \qquad 2.9$$

where $n = 1,2,3,....$

Hence the wave function is given by:

$$\Psi_n(x) = A_n sin\left(\frac{n\pi x}{a}\right) \quad 2.10$$

and the energy of the electron is:

$$E_n = \frac{n^2\pi^2\hbar^2}{2ma^2} \quad 2.11$$

This result is similar to that obtained for the free electron, the energy is a function of the squared momentum in both situations. It must be noted that the wave number *k* and energy *E* in the case of the free electron can take any value, while in the case of the particle-in-the box scenario, the values *k* and *E* take are discrete. These values are fixed by the geometry of the well.

However, if the width of the potential well becomes very large $(a \to \infty)$ the different values of *k* become very close to one another, to the extent that they do not remain discrete any more, rather they form a continuum, as in the case for the free electron.

Let us consider the values *k* can take in a finite crystal of macroscopic dimensions. We now look at the example of one-dimensional linear crystal with length L (Figure 11). If we impose $\Psi(x = 0) = 0$ and $\Psi(x = L) = 0$ as in the case of the particle-in-the-box scenario, equations (2.9) and (2.11) indicate that the permitted values for the momentum and for the energy of the electron will depend on the length of the crystal. This result is clearly unacceptable because the electrical properties of a macroscopic sample do not depend on its dimensions.

Employing the Born-von Karman boundary conditions, referred to as cyclic boundary conditions, leads to much better results. To obtain these conditions, we bend the crystal

such that $x = 0$ and $x = L$ become coincident. With the new geometry, for any value of x, we have the critical boundary conditions: $\Psi(x + L) = \Psi(x)$. Using the free electron wave function (equation 2.2), and taking into account the periodic nature of the problem, we can write:

$$\Psi(x + L) = Aexp(ikx)\, exp(ikL) = Aexp(ikx) = \Psi(x)$$

which imposes:

$$exp(ikL) = 1 \Rightarrow k = \frac{2\pi n}{L} \qquad 2.12$$

where n is an integer.

For a three dimensional crystal with dimensions (L_x, L_y, L_z), the Born-von Karman boundary conditions can be written as follows:

$$k_x = \frac{2\pi n_x}{L_x}, k_y = \frac{2\pi n_y}{L_y}, \text{and } k_z = \frac{2\pi n_z}{L_z} \qquad 2.13$$

where n_x, n_y, n_z are integers.

2.1.3. Valence band and conduction band

The bonds between atoms in a crystal and the electric transport phenomenon are all due to electrons from the outer most shell. In terms of energy bands the bonding electrons in atoms are found in the last occupied band, where electrons have the highest energy levels for ground-state atoms. However, there exists an infinite number of energy bands. The first contain core electrons such as the 1s electrons which are

tightly bound to the atom (nucleus) by strong electrostatic force. The highest bands contain no electrons. The last ground-state which contains electrons is called valence band.

The permitted energy band directly above the valence band is the conduction band. In a semiconductor the conduction band has no electrons at low temperature ($T = 0$ K). As the temperature increases, some electrons gain enough thermal energy to jump from the valence band into the conduction band, where they are free to move. The energy gap between the bottom of the conduction band and the valence band is called the forbidden gap or bandgap and is represented by E_g.

Generally, the following situations can occur depending on the position of an atom in the periodic table (Figure 12).

A: The last (valence) energy band is only partially filled with electrons, even at $T = 0\ K$.

B: The last (valence) energy band is completely filled with electrons at $T = 0\ K$, but the next (empty) energy band overlaps with it (i.e.: an empty energy band shares a range of common energy values; $E_g < 0$).

C: The last (valence) energy band is completely filled with electrons and no empty band overlaps with it ($E_g > 0$).

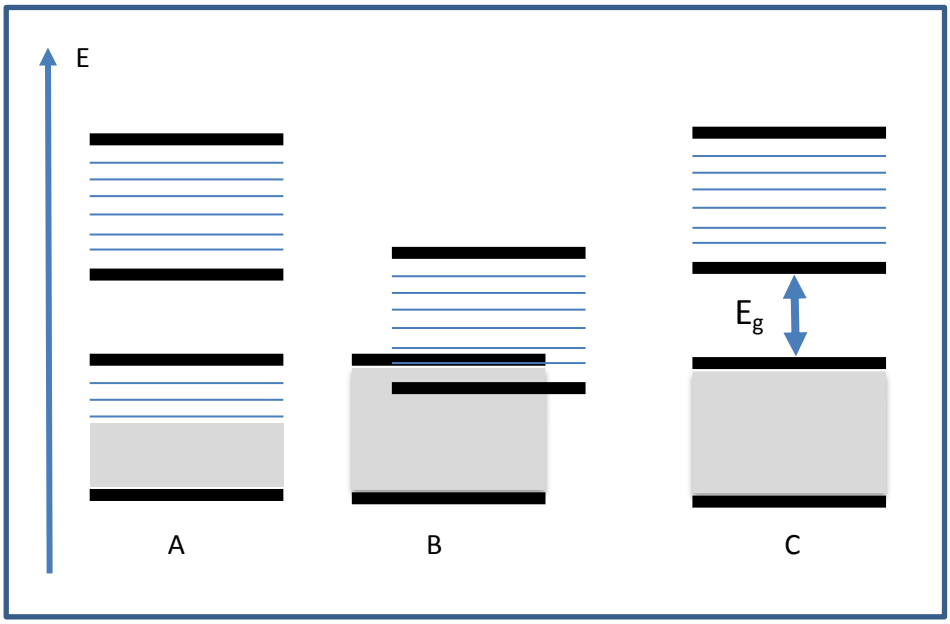

Figure 10: Valence band (bottom) and conduction band in a metal (A and B) and in a semiconductor or an insulator (C). [J.P McKelvey,

From figure 10, in both A and B, electrons with highest energies can easily jump to a slightly higher energy level and move through the crystal after acquiring an infinitesimal amount of energy. That is the electron can leave the atom and move in the crystal without receiving any energy. This is a typical property of metals. In C, a significant amount of energy has to be given to the electron for it to jump from the valence band to the conduction band to enable it leave the atom and move freely or become delocalized in the crystal. A material with such a property is either a semiconductor or an insulator. The difference between the two lies with the quantitative amount of the energy gap E_g. In some semiconductor materials, E_g is such that at room temperature thermal energy or excitation from visible light source can give that energy needed to jump from the valence band to the conduction band.

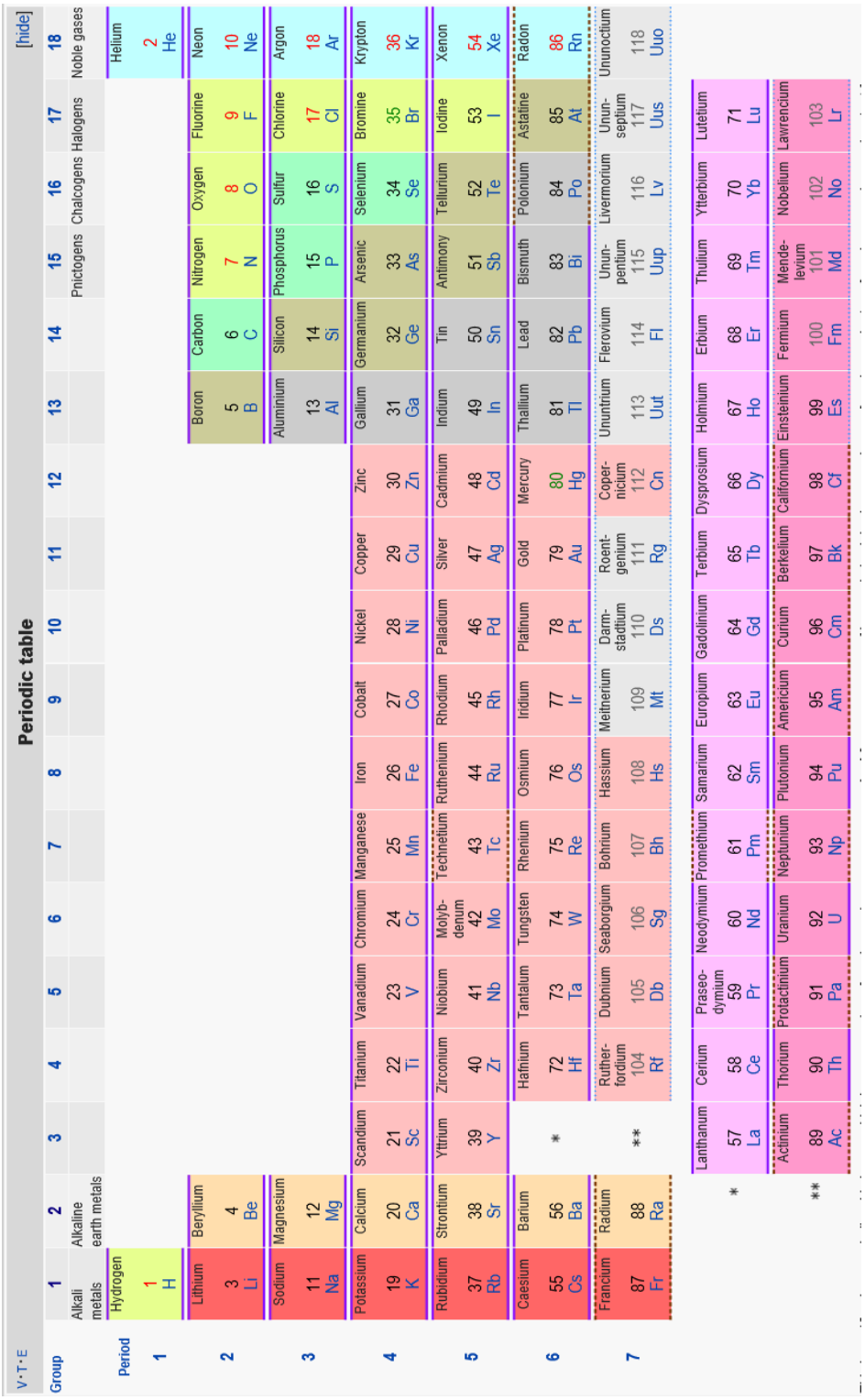

Figure 11: The periodic table

Apart from the elemental semiconductor elements such as silicon and germanium, compound semiconductors can be synthesized by combining some group IV elements such as silicon carbide (SiC) or combining elements from group III and group V such as aluminium arsenide (AlAs) or combining a transition element like copper (Cu) and a group VI element like oxygen (O).

Some non-crystalline materials also exhibit semiconductor properties. Such materials as amorphous silicon, where the distance between atoms varies in a random manner, can behave as semiconductors. The mode of transport of electric charges in these materials are quite different from those in the crystalline semiconductors. [38]

Let us represent the energy bands in real space instead of k-space. That will help obtain a diagram such as in figure 12, where the x-axis represents the physical distance in the crystal. The maximum energy of the valence band is denoted E_V, E_C the minimum energy of the conduction band and E_g the width of the energy bandgap.

The Fermi level, E_F, represents the maximum energy of an electron in the material at 0 K. At this temperature all the permissible energy levels below the Fermi level are occupied. The Fermi level can also be defined as an energy level that has a 50% probability of of being filled with electrons, even though it might reside in the bandgap. In an insulator or a semiconductor where there exists a band gap between E_V and E_C as shown in figure 13, the Fermi level lies somewhere in the bandgap. In a metal the Fermi level lies in an energy band due to the overlap between the valence band and the conduction band.

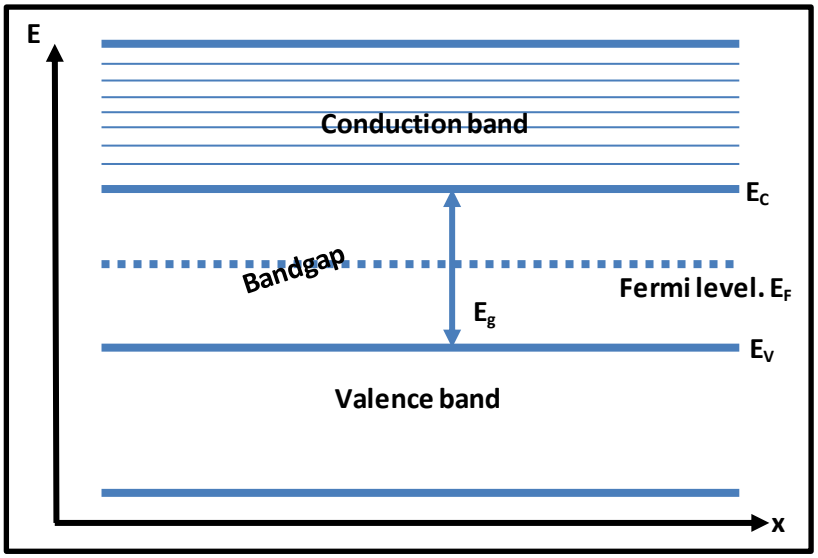

Figure 12: Valence and conduction band in real space

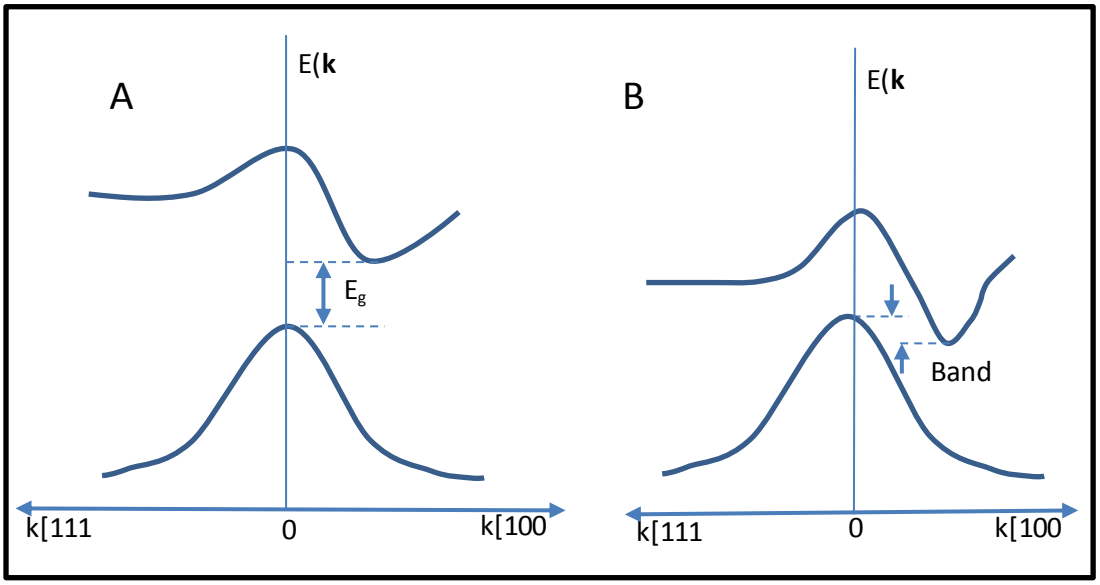

Figure 13: Examples of energy band extrema (minimum of the conduction band and maximum of the valence band in two crystals). In crystal A, E_g is the bandgap energy. There is no bandgap in crystal B because the conduction and the valence bands overlap.

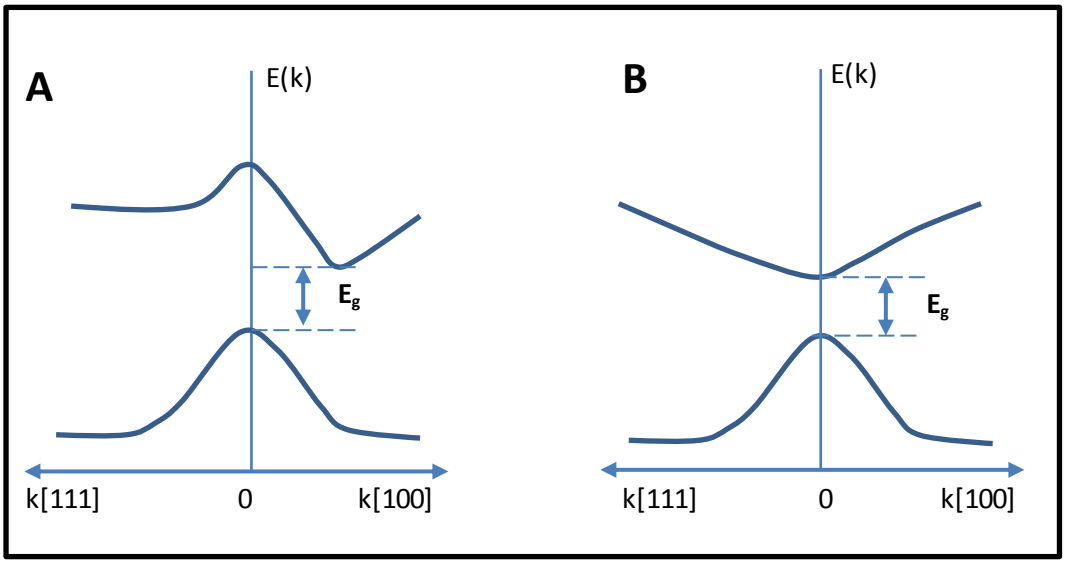

Figure 14: A: Indirect band gap semiconductor, B: Direct band gap semiconductor. [H.F. Wolf, Semiconductors, Wiley and sons, p. 51, 1971]

2.1.4 The hole concept

In electronics, a hole draws its existence from the absence of electron in a given crystal. It is the equivalence of a missing electron in the crystal valence band of a given crystal. Holes can move in a crystal through successive filling of the empty space left by a missing electron. The hole carries an opposite sign to that by an electron but they both have the same magnitude of charge $(1.6 \times 10^{-19}\ \mathrm{C})$.

2.1.5 Generation/Recombination phenomenon

There exist electrons in the conduction band and holes in the valence band in a given crystal of a semiconductor, as long as its temperature is above 0 K. The electron is free to move in the conduction band. It can also occupy a vacant space and in doing the

electron releases energy. This phenomenon in which a free electron and a hole both disappear is referred to as recombination.

An electron can also free itself from a covalent bond if it has enough energy. It jumps from the valence band into the conduction band and is free to move in the crystal. A free hole is created in the process, this leads to the generation of an electron-hole pair.

When there is thermodynamic equilibrium, generation and recombination events occur in equal proportions, such that the electron and hole equilibrium concentrations remain constant with respect to time. However, the carrier concentration can increase and reach a state of non-equilibrium when there is an external source of energy, for example; illumination with light.

2.1.6 Direct and indirect transitions

In some semiconductor materials such as gallium arsenide (GaAs) the conduction band minimum and the valence band maximum both occur at the same k-value. The k-value which is the wave vector represents the momentum of the carriers. It is shown in figure 17 below that the value of that momentum is zero. This means that when an electron from the conduction band recombines with a hole in the valence band, the law of conservation of momentum is obeyed. When the minimum of the conduction band and the maximum of the valence band occur at the same k-value, as illustrated in figure 14 (B) above, the semiconductor is called a direct band gap semiconductor. In this type of semiconductor, the electron jump from the conduction band into the valence band and this is called "band to band recombination".

In other semiconductor materials such as germanium, the minimum of the conduction band and the maximum of the valence band do not occur at the same *k*-value as

illustrated in figure 14 (A) above. Such a material is called an indirect-band gap semiconductor. In such a material an electron with a momentum $k = [k_m, 0, 0]$ recombines with a hole whose momentum $k = [0,0,0]$ (Figure 17). This occurs when a certain required momentum is transferred to the electron (or the hole) such that momentum is conserved. This happens through collision with a phonon or with phonons. A precise value of momentum ($-k_m$ in figure 17) has to be given to the electron , thus band-to-band recombination is an extremely unlikely process in indirect bandgap semiconductors. Instead recombination takes place via trap levels at various k-values within the band gap.

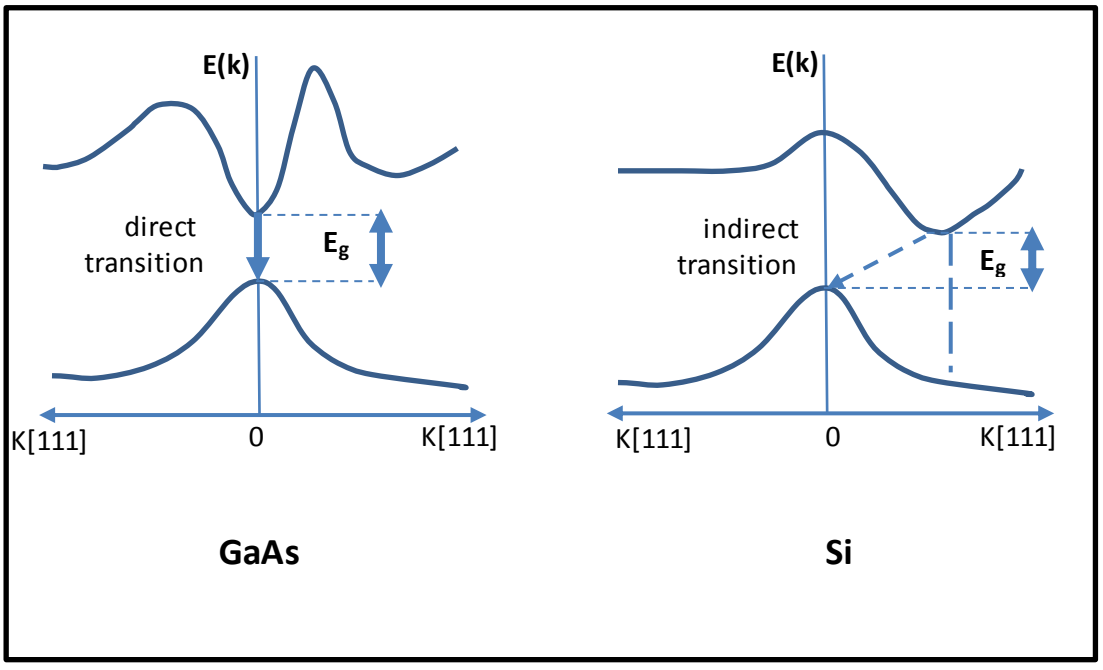

Figure 15: Band-to-band recombination in a direct-bandgap semiconductor (GaAs) and an indirect-bandgap semiconductor (Si)

Semiconductor materials are transparent to photons with energy hv smaller than their bandgap energy. Germanium is used in place of glass to make infrared (IR) lenses for wavelengths larger than 2 µm since its bandgap energy is larger than the energy of 2 µm IR photons. On the other hand, photons with energy equal to or greater than the bandgap energy of the semiconductor, when absorbed can generate electron-hole pairs. Absorption coefficient as a function of wavelength is the measure of the distance travelled by a light wave into a material before it is absorbed.

Apart from band-to-band recombination mechanisms, a free electron can recombine with a free hole through recombination centres located within the energy bandgap. These permitted energy levels are introduced by contaminants, impurity atoms or crystal defects. These centres act as catalyst enabling an electron to recombine at k values differing from the k_m of the conduction band. This is especially true for indirect-bandgap semiconductors, where band-to-band recombination events are unlikely to occur.

2.1.7 Generation/ recombination centres

Semiconductor materials may contain some crystal defects such as interstitials (excess semiconductor atoms in the crystal lattice), vacancies (missing semiconductor atoms in the crystal lattice) and dislocations (imperfections in the crystal structure), as well as traces of impurity elements such as atoms or oxygen. These create permitted levels within the energy bandgap. If one of these permitted levels has energy E_t within the bandgap, it can receive an electron from the conduction band (case A in figure 16), lose an electron to the valence band (case C in figure 18), receive an electron valence band (case D in figure 18) or lose an electron to the conduction band (case B in figure 16). A level that is neutral if filled by an electron and positive if empty is called a

"donor level", and a level that is neutral if empty and negative if filled by an electron is called an "acceptor level". Permitted levels inside the bandgap are called generation-recombination centers, or "recombination centres" . In figure 18 transitions A and C correspond to recombination events, while transitions B and D correspond to generation events. These transitions involve energies that are smaller than the bandgap energy, thus are much more likely to occur than band-to-band transitions, especially in indirect bandgap semiconductors.

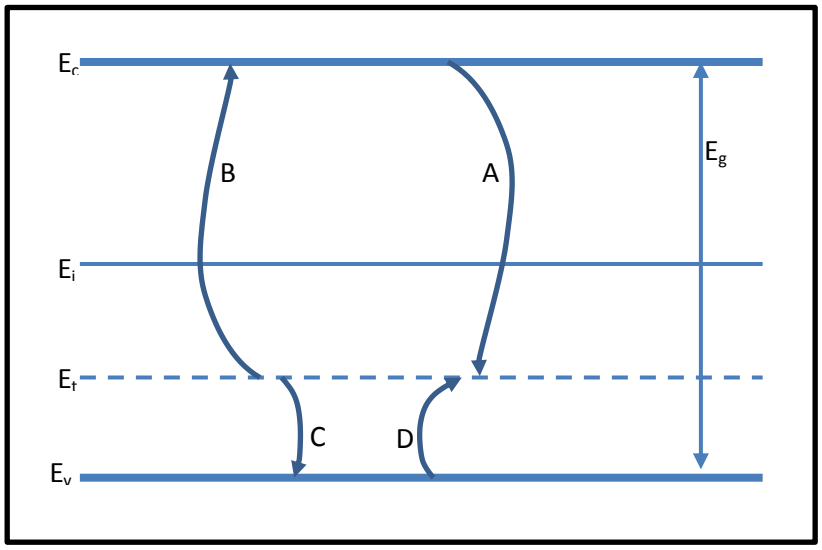

Figure 16: Electron Transitions via a recombination centre at energy E_t.

The terms G_n and G_p in the continuity equations below represent electron-hole pair generation events caused by an external source of energy, such as sunlight penetrating the semiconductor.

$$\frac{\partial n}{\partial t} = \frac{1}{q} div\, J_n + (G_n - U_n) \qquad 2.14$$

$$\frac{\partial p}{\partial t} = -\frac{1}{q} div J_p + (G_p - U_p) \qquad 2.15$$

Natural, intrinsic generation in a semiconductor material arising from thermal agitation at any temperature above 0 K, is encompassed in the intrinsic recombination-generation rate terms in the continuity equations, U_n and U_p. The notations from figure 18 establishes that $U_n = A - B$ and $U_p = C - D$. If U_n (or U_p) is positive a net recombination of carriers is taking place. If it is negative, a net generation of carriers occurs.

During a recombination event, the energy released can bring about different phenomena:

- In a band-to-band radiative recombination event, the energy released is in the form of a photon.
- In an indirect recombination event via an energy level within the bandgap, energy is transferred to the crystal lattice in the form of heat (or phonons).
- In an Auger recombination event the energy released is transferred to another electron (or hole), which becomes excited to a higher energy level.

Recombination of carriers takes place not only within the bulk of the semiconductor crystal, but also at its surface. The surface is the place where the periodicity of the lattce crystal is uninterrupted, and where contac with other substances is made.

- Within the bulk of the crystal a recombination-generation rate (recombination rate), is defined. The recombination rate for electrons is denoted by $U_n$and that for holes, U_p. U_n and U_p are accounted for in the continuity equations and

represent the number of holes and electrons created or annihilated by intrinsic generation/ recombination processes per cm^3 and per second.

- In a similar fashion, a surface recombination velocity is defined for the surface of the semiconductor crystal. The surface recombination rate for electrons is represented by S_n and that for holes S_p. S_n and S_p are boundary conditions for the continuity equations and represent the number of holes and electrons created or annihilated by intrinsic generation/ recombination processes at the surface of a semiconductor crystal per cm^2 per second.

2.1.8 Excess carrier lifetime

At thermodynamic equilibrium, the generation rate and the recombination rate are equal, such that $U_n = U_p = 0$ and $S_n = S_p = 0$. If for one reason or the other, the carrier concentrations are different form their equilibrium value, generation/ recombination mechanisms will tend to force them back to equilibrium. Actually, U_n, U_p, S_n and S_p are directly proportional to how much the carrier concentrations depart from equilibrium:

Generation/ Recombination rate:

$$U_n = \frac{n - n_0}{\tau_n}$$

and

$$U_p = \frac{p - p_0}{\tau_p}$$

where τ is measured seconds

Surface Recombination Rate:

$$S_n = s_n(n - n_0)$$

and

$$S_p = s_p(p - p_0)$$

where; S = surface recombination rate; measured in $\text{cm}^{-2}\ \text{s}^{-1}$

s = surface recombination velocity; measured in $\text{cm}\ \text{s}^{-1}$

n (or p) are the electron (or hole) concentration and n_0 (or p_0), electron (or hole) equilibrium concentration.

If the electron concentration is higher than its equilibrium value, recombination events reduce the number of electrons. On the other hand, if the electron concentration is below its equilibrium value generation events will occur.

By definition τ_n and τ_p are the lifetime of the excess (or missing) electrons or holes respectively, the equilibrium concentrations being considered as reference. Lifetime is the average time span that excess charge carriers (free electrons or holes) will "survive" before recombining, or the average time that missing electrons will be "missing" before being "regenerated" through a generation event.

2.1.9 Shockley-Read-Hall recombination (SRH)

In many instances and in silicon in particular, generation/ recombination events occur through recombination centers located in the energy bandgap. Recombination events of such nature are referred to as SRH recombination events.

One can obtain an analytical expression for the recombination rate for electrons and holes, U_n and U_p, when there are recombination centers at an energy E_t within the bandgap. Let us look at a case of electron generation / recombination assuming that the recombination centers are of the acceptor type. Thus the centers are neutral or negative. Let N_t be the density of the recombination centers and n_t $(n_t \leq N_t)$ the concentration of electrons occupying the centers.

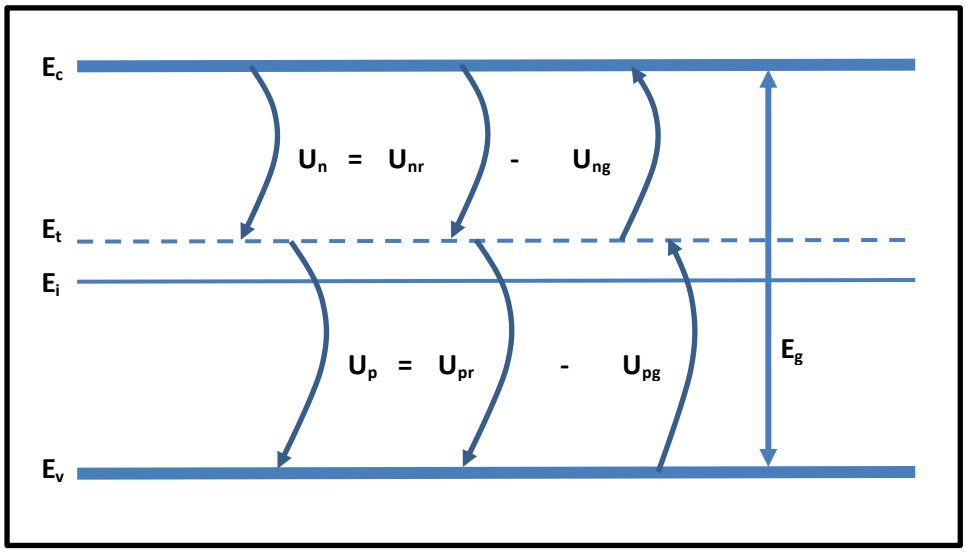

Figure 17: Recombination via an acceptor recombination center.

For easy formulations, the electron generation/ recombination rate U_n, is split into U_{nr} and U_{ng} representing recombination and thermal generation respectively as indicated in figure 17. The recombination rate due to the centers, U_{nr}, is proportional to the concentration of electrons in the conduction band, n, and to the concentration of empty (or neutral) recombination centers, $N_t - n_t$.

Hence one can write:

$$U_{nr} = v_{th}\sigma_n n(N_t - n_t) = v_{th}\sigma_n N_t\left(1 - \frac{N_t}{n_t}\right) = v_{th}\sigma_n n N_t(1 - f(E_t)) \qquad 2.16$$

where v_{th} is the thermal velocity of electrons, defined by

the relationship $v_{th} = \sqrt{3kT/m}$ cms^{-1}, σ_n is called the " electron capture cross section" and is measured in square centimeters (cm^2). The capture cross section is a measure of how close an electron must be to a center to be captured by it, while the thermal velocity is the average speed of electrons due to Brownian-like or random motion at a given temperature ($\frac{1}{2}mv_{th}^2 = \frac{3}{2}kT$, where kT is the thermal energy).[39] It is noted that $f(E_t)$ is the probability that a center with energy E_t is occupied by an electron. The function $f(E_t)$, is the Fermi-Dirac distribution evaluated at the energy of the center , at thermodynamic equilibrium. [40]

The thermal equilibrium rate, U_{ng}, is the process by which electrons can jump from the recombination centers into the conduction band. It is proportional to the concentration centers occupied by an electron, $n_t = N_t f(E_t)$:

$$U_{ng} = e_n N_t f(E_t) \qquad 2.17$$

where $e_n$is a proportionality coefficient which represents the probability of electron emission by the generation/ recombination centers.

In a similar fashion, the recombination rate for holes between the recombination center and the valence band is given by:

$$U_{pr} = v_{th}\sigma_p p n_t = v_{th} N_t f(E_t) \qquad 2.18$$

The thermal generation rate, U_{pg}, is the process by which holes can jump from neutral recombination centers into the valence band. It is proportional to the concentration of centers not occupied by an electron, $n_t = N_t(1 - f(E_t))$:

$$U_{pg} = e_p N_t(1 - f(E_t)) \qquad 2.19$$

where e_p is a proportionality coefficient which represents the probability of hole emission by the generation/ recombination centers.

We can obtain expressions for calculating the proportionality coefficients e_n and e_p.

For a semiconductor in thermal equilibrium, the regeneration and the recombination rates are equal to zero:

$$U_n = U_p = 0 \qquad 2.20$$

The number of negatively charged centers, that is filled centers, is given by the relationship $n_t = N_t f(E_t)$, or :

$$n_t = \frac{N_t}{1 + exp\left[\frac{E_t - E_F}{kT}\right]}$$

At thermodynamic equilibrium, again $U_n = U_{nr} - U_{ng} = 0$. Applying Boltzmann relationship

$$n(x, y, z) = n_i exp\left[\frac{E_F - E_{i0}}{kT}\right] exp\left[\frac{q\Phi_0(x, y, z)}{kT}\right]$$

In the absence of internal potential $(\Phi_0 = 0)$, $U_{nr} = U_{ng}$ can be written as follows:

$$v_{th}\sigma_n n\, N_t(1-f(E_t)) = e_n N_t f(E_t)$$

Using

$$n = n_i exp\left[\frac{E_F - E_i}{kT}\right]$$

the equation above becomes

$$v_{th}\ \sigma_n n_i exp\left[\frac{E_F - E_i}{kT}\right]\left(N_t - \frac{N_t}{1+exp\left[\frac{E_t - E_F}{kT}\right]}\right) = e_n \frac{N_t}{1+exp\left[\frac{E_t - E_F}{kT}\right]}$$

$$\Rightarrow \qquad e_n = v_{th}\ \sigma_n\ n_i\ exp\left[\frac{E_t - E_i}{kT}\right] \qquad 2.21$$

Similarly the hole coefficient can be written as:

$$e_p = v_{th}\ \sigma_p\ n_i\ exp\left[\frac{E_i - E_t}{kT}\right] \qquad 2.22$$

Next, we obtain an expression for the electrons trapped in the generation/ recombination centers, using the continuity equation, under steady state conditions, the generation/ recombination rate:

$$\frac{\partial n_t}{\partial t} = U_n - U_p + G_n - G_p = 0 \qquad 2.23$$

External generation creates equal amounts of electrons and holes, therefore; $G = G_n = G_p$, From equation (2.23) we obtain $U_n = U_p$. Using equations (2.16) to (2.19), one obtains:

$$U_n = U_p \Rightarrow U_{nr} - U_{ng} = U_{pr} - U_{pg}$$

$$\Rightarrow \quad v_{th}\,\sigma_n\,n\,N_t(1-f(E_t)) - e_n\,N_t f(E_t) = v_{th}\,\sigma_p\,p\,N_t f(E_t) - e_p\,N_t\big(1-f(E_t)\big) \tag{2.24}$$

Substituting equations 2.21and 2.22 into 2.24 and solving for $f(E_t)$ gives:

$$f(E_t) = \frac{\sigma_n n + \sigma_p n_i exp\left[\frac{E_i - E_t}{kT}\right]}{\sigma_n\left(n + n_i\, exp\left[\frac{E_t - E_i}{kT}\right]\right) + \sigma_p\left(p + n_i exp\left[\frac{E_i - E_t}{kT}\right]\right)} \tag{2.25}$$

The generation/ recombination rate can be calculated now:

$$U = U_n = U_p = U_{nr} - U_{ng} = v_{th}\sigma_n n\,N_t\big(1-f(E_t)\big) - e_n\,N_t f(E_t)$$

Substituting 2.25 into the above expression gives

$$U = \frac{\sigma_n\sigma_p v_{th} N_t(pn - n_i^2)}{\sigma_n\left(n + n_i exp\left[\frac{E_t - E_i}{kT}\right]\right) + \sigma_p\left(p + n_i exp\left[\frac{E_i - E_t}{kT}\right]\right)}$$

which further reduces into

$$U = \frac{pn - n_i^2}{\tau_p\left(n + n_i exp\left[\frac{E_t - E_i}{kT}\right]\right) + \tau_n\left(p + n_i exp\left[\frac{E_i - E_t}{kT}\right]\right)} \tag{2.26}$$

where

$$\tau_n = \frac{1}{N_t v_{th}\sigma_n} \quad \text{and} \quad \tau_p = \frac{1}{N_t v_{th}\sigma_p} \tag{2.27}$$

τ_n and τ_p are called "lifetime" of electrons and holes in the steady-state regime, respectively.

From equation (2.26) one can see that the recombination rate U is directly proportional to $pn - n_i^2$. The recombination rate represents a force which tends to bring the product pn back to its equilibrium value, n_i^2. We see that:

$$\begin{cases} U = 0 \; if \; pn = n_i^2 \; (\text{equilibrium}) \\ U > 0 \; if \; pn > n_i^2 \; (\text{recombination}) \\ U < 0 \; if \; pn < n_i^2 \; (\text{generation}) \end{cases}$$

The recombination rate is highest when the recombination centers have an energy close to E_i.

If we assume that both the hole and the electron cross sections are the same, then equation (2.26) can be written as:

$$U = \frac{pn - n_i^2}{\tau_o \left(p + n + 2n_i cosh\left[\frac{E_t - E_i}{kT}\right]\right)} \qquad 2.28$$

where

$$\tau_o = \frac{1}{N_t v_{th} \sigma_o} \qquad 2.29$$

2.1.10 Minority carrier lifetime

The lifetime of the minority carriers is very crucial for the efficiency of certain semiconductor devices whose operation depends on the injection of minority carriers. We consider equation (2.26) in a situation where the excess carrier concentrations, $\delta_n = n - n_o$ and $\delta_p = p - p_o$ are small compared to equilibrium concentrations: $\delta n << n_o$ and $\delta p << p_o$. This is low-level injection. We can write:

$$pn = (p_o + \delta p)(n_o + \delta n)$$

$$\Rightarrow pn - n_i^2 \cong p_o \delta n + n_o \delta p \qquad 2.30$$

Equation (2.26) can be rewritten as:

$$U = \frac{p_o \delta n + n_o \delta p}{\tau_p \left(n + n_i exp\left[\frac{E_t - E_i}{kT}\right]\right) + \tau_n \left(p + n_i exp\left[\frac{E_i - E_t}{kT}\right]\right)} \qquad 2.31$$

For centers where the recombination rate is highest $(E_t \cong E_i)$:

$$U = \frac{p_o \delta n + n_o \delta p}{\tau_p (n + n_i) + \tau_n (p + n_i)} \qquad 2.32$$

but $n = n_o + \delta n$ and $p = p_o + \delta p$ and $\delta n << n_o$ and $\delta p << p_o$:

$$U = \frac{p_o \delta n + n_o \delta p}{\tau_p (n_o + n_i) + \tau_n (p_o + n_i)} \qquad 2.33$$

Recombination rate

For a p-type semiconductor, $p_o > n_i > n_o$, therefore:

$$U = \frac{\delta n}{\tau_n} = \frac{n - n_o}{\tau_n} \qquad 2.34$$

For an n-type semiconductor, $n_o > n_i > p_o$, therefore:

$$U = \frac{\delta p}{\tau_p} = \frac{p - p_o}{\tau_p} \qquad 2.35$$

2:1:11 Surface recombination

Recombination of excess carriers also occurs at the surface of the semiconductor crystal. The surface of a semiconductor material acts as the interface between the material and another material. At the surface of the semiconductor material the periodicity of the atoms is disrupted to a very large extent. This and other factors contribute to the usually higher rate of recombination at the surface than in the bulk of the material.

Let us define the surface recombination rate for electrons and holes, S_n and S_p, as the number of carriers disappearing per unit area per second on the semiconductor material surface due to recombination process. The S_n and S_p can thus be used as boundary conditions for the continuity equations (2.14) and (2.15).

A derivation of the surface recombination will result in the equation (2.36) below:

$$S = \frac{\sigma_n \sigma_p v_{th} N_{st} (p_s n_s - n_i^2)}{\sigma_n \left(n_s + n_i exp\left[\frac{E_{st} - E_i}{kT}\right]\right) + \sigma_p \left(p_s + n_i \, exp\left[\frac{E_i - E_{st}}{kT}\right]\right)} \qquad 2.36$$

where n_s and p_s are the electron and hole concentrations (measured in cm^{-3}) at the surface respectively, N_{st} is the concentration of surface recombination centers (measured in cm^{-2}), and E_{st} is their energy. Similar to bulk recombination, the most efficient recombination centers are those located at midgap energy.

If we assume that $\sigma_n \cong \sigma_p = \sigma_o$, equation (62) becomes:

$$S = \frac{\sigma_n v_{th} N_{st}(p_s n_s - n_i^2)}{p_s + n_s + 2\, n_i cosh\left[\frac{E_{st} - E_i}{kT}\right]} \qquad 2.37$$

We can write the pn product at the surface as:

$$p_s n_s = (p_o + \delta p_s)(n_o + \delta n_s) \Rightarrow p_s n_s - n_i^2 \cong p_o \delta n_s + n_o \delta p_s$$

The recombination rate at the surface of a given semiconductor crystal is larger than the rate inside the crystal. Introducing the surface recombination rate into the continuity equation in the following way:

$$A\frac{J_n(x_o)}{-q} = AS_n = As_n\,(n_s - n_o) \qquad 2.38$$

for electrons, and :

$$A\frac{J_p(x_o)}{-q} = AS_p = As_p\,(p_s - p_o) \qquad 2.39$$

for holes.

The surface recombination rate can be infinite in such cases as at the metal-semiconductor contact.

2.2 Photovoltaic Conversion

The direct conversion of radiant energy into electrical energy can occur through the use of semiconductor materials, whose conductivity is strongly enhanced by electron excitation, caused by impinging light quanta.

Electrical energy is only produced when the excited electrons are not only able to move freely but are made to move in a directed way. A certain force would have to act on these free electrons for them to move. This force will come from an electrical potential gradient, such as is in a p-n junction of doped semiconductor materials. A p-n junction provides an electrical field that will cause the electrons excited by radiation (such as solar) to move in the direction from the p-type to the n-type material and cause the vacancies (holes) left by the excited electrons to move in the opposite direction. [41] An electrical power can be delivered to an external circuit if and only if the electrons and the holes are able to reach the respective edges of the semiconductor material. There is competition from recombination processes which hampers the motion of the charge carriers (electrons and holes) thus factors such as overall dimensions and electron mobility in the material used become paramount in considering materials for conversion of radiant energy directly into electrical energy.

There is a large number of materials which exhibit photovoltaic characteristics, however the number of materials that are able to make conversion of solar radiation into electrical energy with efficiency of the order of 20% and with high stability under operation is small. There is substantial amount of research effort aimed at finding

materials which make the threshold properties required to generate affordable electricity from solar radiation.

2.2.1 The p-n junction

When a p-type and n-type semiconductor materials are joined together such that there exists a common surface between them, they are said to have formed a p-n junction. This will result in electrons flowing at the initial stages. The electron density in the conduction band of the n-type is higher, just as the hole density in the valence band of the p-type is high because there is a surplus of positive charge in the n-type material around the junction, and surplus of electrons in the p-type material. There is the formation of a dipole layer creating an electrostatic potential difference preventing further unidirectional flow of electrons until an equilibrium situation occurs in which the potential difference is such that no net transfer takes place.

Let us state the equilibrium condition in terms of Fermi Energy. If μ_p and μ_n are the Fermi energies of p-type and n-type materials respectively, $\mu_p \neq \mu_n$ at the initial stage, but at equilibrium $\mu_p = \mu_n$. The change in relative positions of the conduction (valence) bands in the two types of materials with respect a non-doped semiconductor material must be equal to the electron charge $-e$, times the equilibrium electrostatic potential. [41]

The number of electrons in the conduction band may be written as

$$n_c = \int_{E_c}^{E_c'} n'(E') f(E) dE \qquad 2.40$$

where E_c and E_c' are the lower and upper energy limit of the conduction band, $n'(E)$ is the number of quantum states per unit energy interval, and $f(E)$ is the Fermi-Dirac distribution. If the electrons in the conduction band are regarded as free, elementary quantum mechanics gives [41]

$$n'(E) = 4\pi h^{-3}(2m)^{3/2}E^{1/2} \qquad 2.41$$

where h is the Planck's constant and m is electron mass.

The corrections for electrons moving in condensed matter, rather than being free, may to a first approximation, be included by replacing the electron mass by an effective value.

If the Fermi energy is not close to the conduction band,

$E_c - \mu \gg kT$,

the Fermi-Dirac distribution may be replaced by the Boltzmann distribution,

$$f_B(E) = \exp(-(E-\mu)/kT). \qquad 2.42$$

Evaluating the integral, equation (2.40) then gives an expression of the form

$$n_c = N_c \exp(-E_c - \mu)\ /kT) \qquad 2.43$$

The number of holes in the valence band is found in an analogous manner,

$$n_v = N_v \exp(-(\mu - E_v)/kT), \qquad 2.44$$

where E_v is the upper limit energy of the valence band.

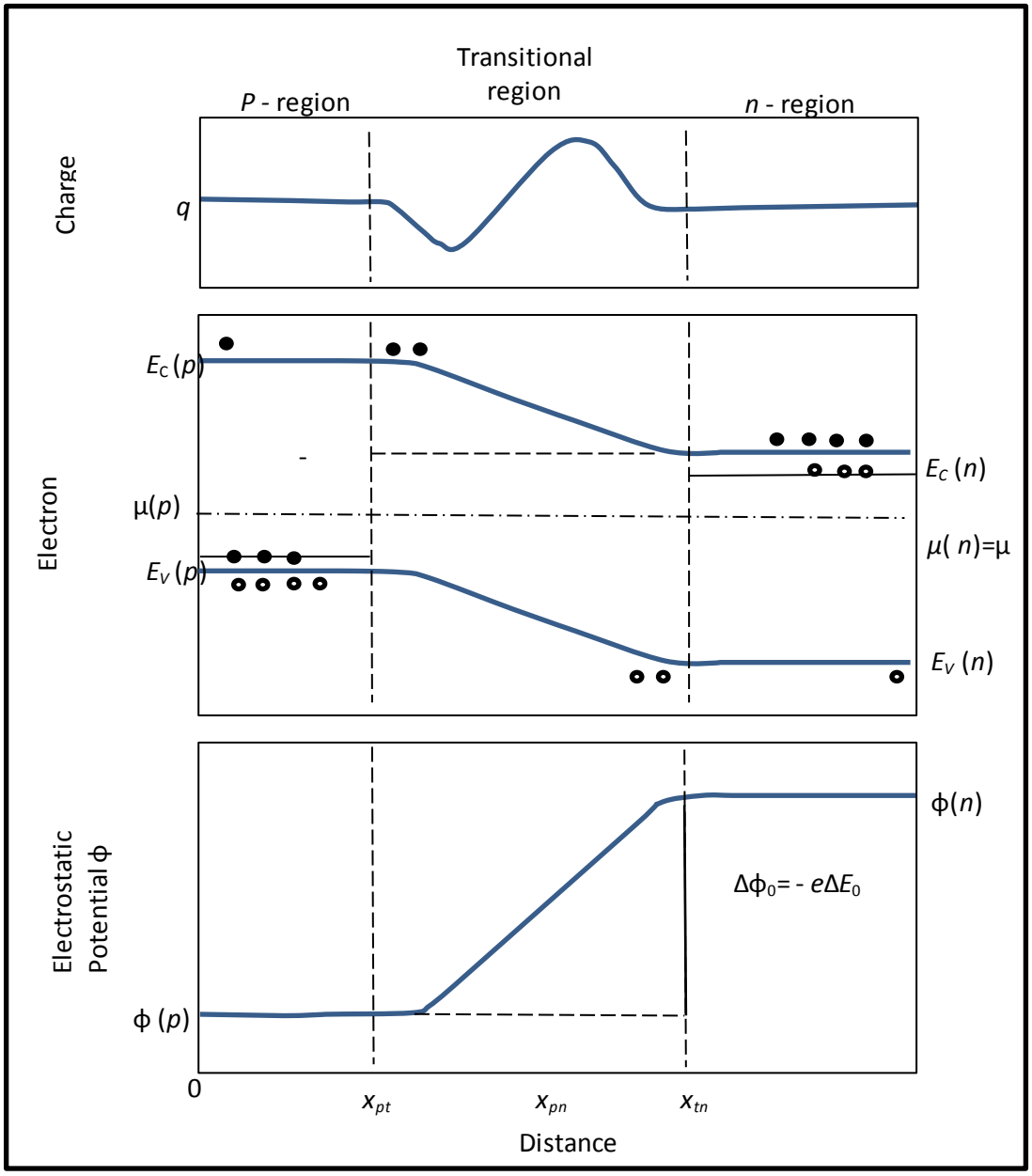

Figure 18: Schematic picture of the properties of a p-n junction in an equilibrium condition. The x-direction is perpendicular to the junction (all properties are assumed to be homogenous in the y- and z-directions). The charge (top) is the sum of electron charges in the conduction band and positive hole charges in the valence band, plus

charge excess or defect associated with the acceptor and donor levels. In the electron energy diagram (middle), the abundance of minority charge carriers (closed circles for electrons and open circles for holes) is schematically illustrated.

The equilibrium currents in a p-n junction such as illustrated in figure 18 above can be calculated. Let us firstly consider the electron currents in the conduction band, the thermal electrons in the conduction band in the p-type region can freely flow into the n-type material. The resulting current $I_0^-(p)$, may be considered proportional to the number of electrons in the conduction band in the p-region, $n_c(p)$, given by equation (2.43),

$$I_0^-(p) = \alpha N_c \exp(-(E_c(p) - \mu(p))/kT) \qquad 2.45$$

where the constant α depends on the electron mobility in the material and on the electrostatic potential gradient , grad ϕ. The electrons excited into the conduction band in the n-type region will have to climb the potential barrier to enable them move into the p-region. The fraction of electrons capable of overcoming this potential barrier is given by a Boltzmann factor of the form (2.43), but with additional energy barrier $\Delta E_0 = -\Delta\phi_0/e$ ($-e$ being the electron charge),

$$n_c = N_c \exp(-(E_c(n) - \mu(n) - \Delta E_0)/kT$$

.

Applying $-\Delta E_0 = E_c(p) - E_c(n)$ and considering the current $I_0(n)$ as being proportional to $n_c(n)$, the corresponding current may be written as

$$I_0^-(n) = \alpha' N_c \exp(-(E_c(n) - \mu(n))/kT \qquad 2.46$$

where α'depends on the diffusion parameter and on the relative change in the electron density, $n_c^{-1}\text{grad}(n_c)$, looking at the electron motion against the electrostatic potential as a diffusion process. The statistical mechanical condition for thermal equilibrium demands that $\alpha = \alpha'$ [42], so equations (2.45) and (2.46) show that the net electron current,

$$I_0^- = I_0^-(p) + I_0^-(n),$$

becomes zero when

$$\mu(p) = \mu(n),$$

which is the condition for thermal equilibrium. The same is true for the hole current,

$$I_0^+ = I_0^+(p) + I_0^+(n).$$

Applying an external voltage source to the p-n junction, such that the n-type terminal receives an additional electrostatic potential $\Delta\phi_{ext}$ relative to the p-type terminal, the junction is no longer in thermal equilibrium, and the Fermi energy in the p-region is no longer equal to that of the n-region, but satisfies

$$\mu(p) - \mu(n) = e^{-1}\Delta\phi_{ext} = \Delta E_{ext}, \qquad 2.47$$

if the Boltzmann distribution of electrons and holes are to maintain their shapes in both p-and n-regions. In a similar fashion, $E_c(p) - E_c(n) = -(\Delta E_0 + \Delta E_{ext})$, and assuming the proportionality factors in equations (71) and (72) still bear the relationship $\alpha = -\alpha'$ in the presence of the external potential, the currents are connected by the expression

$$I^{-}(n) = -I^{-}(p)\exp(\Delta E_{ext}/kT)$$

.

The net electron current in the conduction band then becomes

$$I^{-} = I^{-}(n) + I^{-}(p) = -I^{-}(p)\left(\exp\left(\frac{\Delta E_{ext}}{kT}\right) - 1\right). \qquad 2.48$$

The contributions to the hole current , I^{+}, behave in a like manner to those of the electron current, and the total current I across p-n junction with an external potential $\Delta\phi_{ext} = -e\Delta E_{ext}$ may be written as:

$$I = I^{-} + I^{+} = -I(p)(\exp(\Delta E_{ext}/kT) - 1) \qquad 2.49$$

The relationship between current and potential is called the "characteristic" of the device, and the relation (2.49) for the p-n junction is illustrated in figure 19 by the curve labelled "no light". The constant saturation current $I(p)$ is sometimes called "dark current".

2.3.2 Solar cell

A solar cell is constructed when the p-n junction is shaped in such a way that the p-type semiconductor material can be reached by incident solar radiation, eg. by placing a thin layer of p-type material on an n-type semiconductor material. In the dark and when there is no external potential (voltage), the net current across the junction is zero, ie. the intrinsic potential difference is unable to do work against an external load.

When light of energy $E_{light} = hv = hc/\lambda$, which is larger than the band gap of the semiconductor material, is incident on the device then photo excited electrons move

into the conduction band from the valence band. The absorption of the light energy produces as many holes in the valence band of the p-type semiconductor material as electrons in the conduction band. In the dark there is fewer number of electrons in the conduction band of the p-type semiconductor material than holes in the valence band, therefore a dramatic increase in the number of conduction band electrons can occur and not significantly change the number of holes in the valence band. If the excess electrons are sufficiently close enough to the p-n junction to be able to reach it by diffusion before recombination with holes can occur, then the current in this direction exceeds $I_0^-(p)$ by an amount I_s, which is the net current through the junction in case there is a short circuit from the n-type to the p-type material.

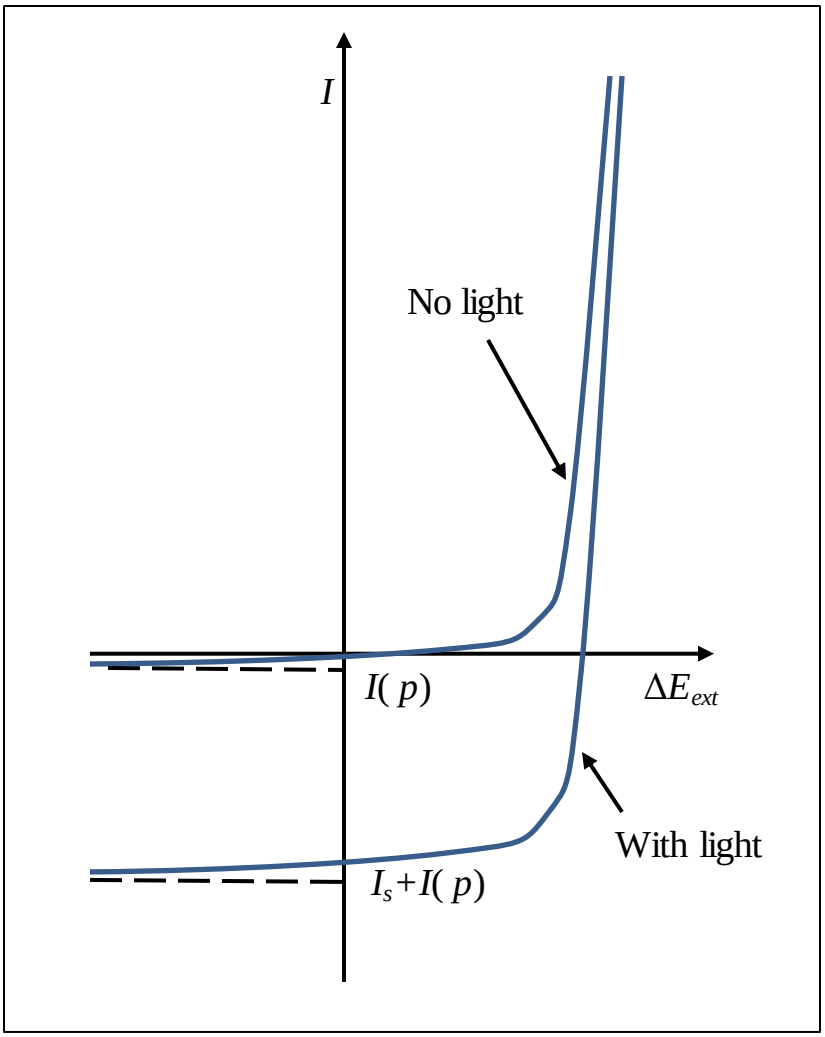

Figure 19: IV characteristics of a p-n junction, without light and with light. The magnitude of the short-circuit current, I_s, is a function of light intensity and spectral distribution.

The other alternative n-p type of solar cell may consist of a thin n-type semiconductor layer exposed to solar radiation on top of a p-type base. Here the excess holes in the n-type valence band produce the photo-induced current I_s.

The total current resulting from light absorption in the p-type semiconductor material and with an external potential drop is given by

$$I = I_s - I(p)(\exp(-\Delta\phi_{ext}/kT) - 1) \qquad 2.50$$

The incident light should possess frequencies sufficient enough to excite electrons into the conduction band. The short circuit current depends on the amount of light with such frequencies, the fraction absorbed and the conditions for transporting the excess electrons created in the conduction band, competing with electron hole pair recombination. The short circuit current I_s, may be written as the sum of a conduction and diffusion-type current, both related to the number of excess electrons in the conduction band, n_c^{ind}, induced by the absorption of light.

$$I_s = e(m_c E_c n_c^{ind} + k_c dn_c^{ind}/dx) \qquad 2.51$$

where e is the electronic charge, m_c, the mobility of conduction band electrons, E_c, the local electric field and k_c, the diffusion constant. x is the depth below the surface of the cell, assumed to be the only significant co-ordinate.

At a depth x the excess electron density $n_c^{ind}(x)$ changes when additional electrons are photo-excited, when electrons are carried away from x by the current I_s, and when electrons recombine with holes. The rate of change of $n_c^{ind}(x)$ is given by

$$\frac{\partial n_c^{ind}(x)}{\partial t} = \int \sigma(v) n_{ph}(v) \exp(-\sigma(v)x)\, \mathrm{d}v + \frac{I}{e}\frac{\partial I_s}{\partial x} - n_c^{ind}(x)\frac{1}{\tau_c} \qquad 2.52$$

where $\sigma(v)$ is the cross section for absorption of photons in the p-type material, and $n_{ph}(v)$ is the number of photons at the cell surface ($x = 0$) per unit time and unit

interval of frequency v. The last parameter, τ_c, is the average lifetime of an electron excited into the conduction band before recombination. The most energetic light quanta in visible light could theoretically excite more than one electron per photon. [41]

For an open ended solar cell, the difference in the electrical potential between the terminals, $V_{oc} = \Delta\phi_{ext}(I = 0)$, is obtained by equating I to zero in equation (2.50),

$$V_{oc} = kTe^{-1}(\log(I_s/I(p)) + 1) \qquad 2.53$$

The electrical power delivered by the cell receiving radiation of the required frequencies to the external circuit is obtained by multiplying equation (2.50) by the external voltage.

$$E = (\Delta\phi_{ext})I = \Delta\phi_{ext}(I_s - I(p)(\exp(-e\Delta\phi_{ext}/kT) - 1)) \qquad 2.54$$

In order to determine the maximum value of power, E_{max}, the external voltage V_{opt} should be determined from $\partial E/\partial(\Delta\phi_{ext}) = 0$. V_{opt} is a slowly varying function of incident radiation and the corresponding current denoted by I_{opt}.

The efficiency of conversion of the solar cell is the ratio of the power E delivered, to the incident energy E_+^{sw}, $\eta = E/E_+^{sw}$.

In terms of the flux of photons of given frequency incident on the solar cell

$$E_+^{sw}(1 - a) = \int_0^\infty hvn_{ph}(v)\mathrm{d}v \qquad 2.55$$

where a is the albedo (fraction of the incident radiation reflected), h is Planck's constant.

The maximum fraction of energy that can be absorbed by a given semiconductor material is

$$\int_{hv=E_c(p)-E_v(p)}^{\infty} hvn_{ph}(v)\mathrm{d}v.$$

The part of the integral from zero to the energy gap represents a fundamental loss. The same applies to the energy of each light quantum in excess of the semiconductor energy gap $E_c(p) - E_v(p)$.

The energy flux available for photo-conversion can therefore be given by

$$\left(E_c(p) - E_v(p)\right)\int_{hv=E_c(p)-E_v(p)}^{\infty} n_{ph}(v)\mathrm{d}v = E^{avail} \qquad 2.56$$

2.2.2.1 Characterization of Solar cells

One of the most important parameters of a solar cell is its conversion rate or efficiency. This depends on how much of the radiation with required threshold frequency of radiation equivalent to the energy band gap of the cell can be converted into electrical energy by the cell. The efficiency depends on the open circuit voltage, short circuit current and the fill factor of the cell.

It is useful to create a model of an electrical circuit based on discrete electrical components whose behaviour is well known. This model should mimic the behaviour of the solar cell.

The solar cell can be modeled as a current source in parallel with a diode. The equivalent circuit of a solar cell is shown in figure 20.

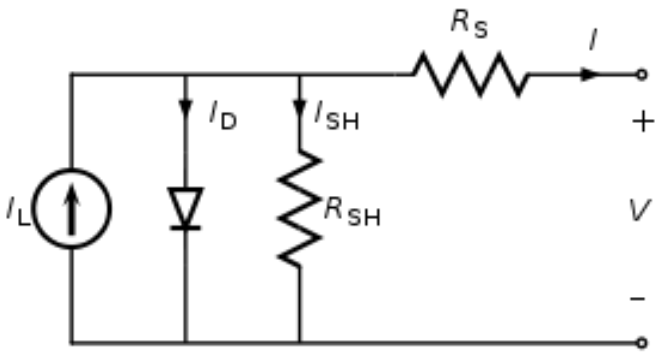

Figure 20: Equivalent electrical circuit of a solar cell

The current produced by the solar cell can be calculated from equation 2.27 derived from the circuit diagram in figure 20

$$I = I_L - I_D - I_{SH} \qquad 2.57$$

where

I is the output current

I_L is the light-generated current

I_D is the diode current and

I_{SH} is the shunt current.

The respective voltages across each of the elements are related by the equation:

$$V_j = V + IR_s \qquad 2.58$$

where

V_j is voltage across both diode and resistor R_{SH}

V is voltage across output terminals

I output current

R_s is the series resistance.

The current going through the diode I_D can be obtained from the relation:

$$I_D = I_0 \left\{ exp\left[\frac{qV_j}{nkT}\right] - 1 \right\} \quad 2.59$$

where

I_0 is the reverse saturation current

n is the diode ideality factor

q is the electronic charge

k is the Boltzmann's constant

T is the absolute temperature.

The current through the shunt can be obtained by

$$I_{SH} = \frac{V_j}{R_{SH}} \quad 2.60$$

where

R_{SH} is the shunt resistance.

Putting equations (2.58), (2.59), and (2.60) into equation (2.57) gives the characteristic equation of a solar cell, relating solar cell parameters to the output current and voltage:

$$I = I_L - I_0 \left\{ exp\left[\frac{q(V + IR_S)}{nkT}\right] - 1 \right\} - \frac{V + IR_S}{R_{SH}} \quad 2.61$$

When numerical values for I and V are obtained the the percentage conversion of the cell can be determined.

At open circuit, $I = 0$ and the voltage across the output terminal is defined as the open-circuit voltage. For a high resistance shunt, the final term in equation (2.61) becomes negligible, the open circuit voltage

$$V_{OC} \approx \frac{nkT}{q} ln\left(\frac{I_L}{I_0} + 1\right) \qquad 2.62$$

In a similar fashion when the cell is operated at short circuit, $V = 0$ and the current I through the terminals is defined as short circuit.

A semiconductor material suitable for photovoltaic application should possess properties such as the ability to conduct; its resistance to the flow of charge carriers should change when light of suitable frequency is incident on it, and the resistance should also change with temperature. Investigating a semiconductor material to ascertain the response of the material to temperature and light in terms of its resistance to the flow of electric charges is potentially a sure way of determining the suitability of such a material for photovoltaic application [71]. The ability of CuO to absorb strongly throughout the visible spectrum makes it a good candidate for photovoltaic applications. It is therefore worthwhile for the synthesized CuO nanoparticles to be exposed to light and its electrical conductivity evaluated to ascertain its suitability for solar cell fabrication [72].

2.3 Schottky Junction

2.3.1 Schottky diode

It is expected that charge carriers will move across the interface when a metal and an n-type semiconductor are in contact with each other. In a metal there are electrons at the Fermi energy level but it is not so with a semiconductor. In thermodynamics, it is required that for thermal equilibrium within the semiconductor, a certain amount of all the electrons in the semiconductor material should be in the conduction band (CB) at a given temperature above absolute 0 degrees.

For thermal equilibrium to be maintained, whenever an electron is removed from CB, an electron has to be excited from the valence band (VB) to CB. This transition involves taking heat from the environment. Therefore the amount of energy required to remove an electron from the valence band of the semiconductor is not just equivalence of electron affinity. However, the minimum energy required to remove an electron from the valence band of a semiconductor at any temperature (beyond the absolute zero) is the electron affinity. We consider the situation of semiconductor in contact with a metal, the more energetic electrons in the conduction band of the semiconductor can tunnel into the metal to locate empty lower energy levels just above the Fermi energy level in the metal and accumulate near the surface of the metal.

The tunneling electrons from the semiconductor create an-electron depleted region of width W where positive charges (donors) as a result of electron deficiency bring about net positive space charge. A built-in potential V_o , also known as contact potential develops between the metal and the semiconductor. This potential is associated with a built-in-electric field E_o from the positive charges to the negative charges on the

surface of the metal. This in-built potential at some point reaches a value where further accumulation of electrons at the surface of the metal is prevented and equilibrium is reached. The depleted region contains exposed positive donors and forms a space charge layer where there is nonuniform internal field directed from the semiconductor to the metal surface.

In a situation where the Fermi level is not uniform in equilibrium throughout the entire metal semiconductor, a change in the Fermi level ΔE_F going from one end to the other can do an external work.

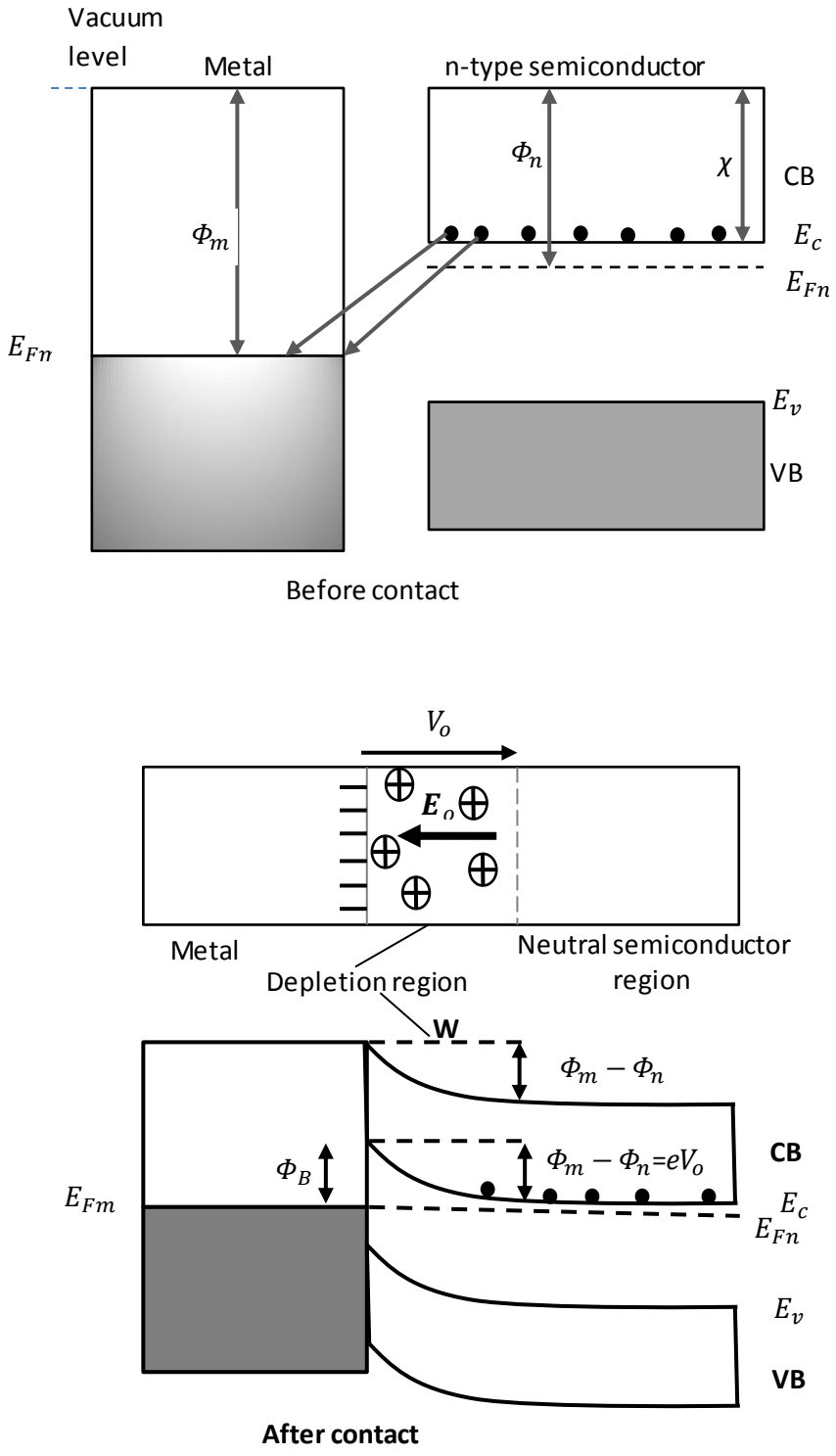

Figure 21: Formation of Schottky junction between a metal and n-type semiconductor

The potential energy barrier for electrons moving from the metal to the semiconductor is called Schottky barrier height Φ_B and is given by

$$\Phi_B = \Phi_m - \chi = eV_o + (E_c - E_{Fn}) \quad 2.63$$

where Φ_m is the work function of the metal, χ the electron affinity of the semiconductor, and E_{Fn}, the Fermi energy within the n type semiconductor.

No net current flows through the metal – semiconductor junction for an open circuit condition. The number of electrons thermally emitted over the potential barrier Φ_B from the metal to the semiconductor is equal to the number of electrons emitted thermally across eV_o from the semiconductor to the metal. The current due to electrons flowing through the junction has two components. Electrons that are thermally emitted from the metal to the conduction band of the semiconductor constitute current given by

$$J_1 = C_1 exp\left(-\frac{\Phi_B}{kT}\right) \quad 2.64$$

and the current due to thermally emitted electrons from the conduction band of the semiconductor to the metal is given by

$$J_2 = C_2 exp\left(-\frac{eV_o}{kT}\right) \quad 2.65$$

where C_1 and C_2 are some constants which differ from each other.

Emission probability depends on the potential energy (PE) barrier for emission through the Boltzmann factor.

For open circuit conditions in the dark, the currents are equal but opposite in sign:

$$J_{open\ circuit} = J_2 - J_1 = 0$$

To forward bias the arrangement, the semiconductor end of the semiconductor metal junction is connected to the negative terminal. Almost all the voltage drop is across the depletion region due to the fact that the depletion region W has much larger resistance than the neutral n-region (outside W) and the metal end of the arrangement. The applied bias is in the direction opposite to that of the built-in voltage V_o. V_o is thus reduced by V but Φ_B remains unchanged. The electrons in the conduction band of the semiconductor can easily overcome the small potential energy barrier and enter the metal.

For the reverse bias situation, the semiconductor end of the junction is connected to the positive end of the battery or the voltage source. The applied bias is in the same direction as the built in voltage V_o , V_o is increased by V_r, it is therefore difficult for electrons in the metal to overcome the potential energy barrier Φ_B and enter the semiconductor. The IV characteristics of Schottky junction exhibits rectifying properties.

For the forward bias, the potential energy barrier for thermal emission of electrons from the semiconductor to the metal is $e(V_o - V)$. This makes it easier for electrons in the conduction band to overcome the potential barrier to the metal.

The forward bias current due to emission from the semiconductor to the metal becomes

$$J_2^F = C_2 exp\left[-\frac{e(V_o - V)}{kT}\right] \qquad 2.66$$

Φ_B remains the same therefore J_1 remains unchanged. Thus the net current is given by

$$J = J_2^F - J_1 = C_2 exp\left[-\frac{e(V_o - V)}{kT}\right] - C_2 exp\left(-\frac{eV_o}{kT}\right)$$

simplifying

$$J = C_2 exp\left(-\frac{eV_o}{kT}\right)\left[exp\left(\frac{eV}{kT}\right) - 1\right]$$

giving

$$J = J_o\left[exp\left(\frac{eV}{kT}\right) - 1\right] \qquad 2.67$$

where J_o is a constant that depends on the material and the surface properties of the two solids.

For a reverse bias Schottky junction, the positive terminal of the voltage source is connected to the semiconductor. There is a drop in the applied voltage V_r across the depletion region due to the less number of carriers making it highly resistive. There is increase in the built-in voltage from V_o to $V_o + V_r$. The potential energy barrier for thermal emission of electrons from the conduction band of the semiconductor to the metal is now $e(V_o + V_r)$ leading to the corresponding current component giving by

$$J_2^{rev} = C_2 exp\left[-\frac{e(V_o + V_r)}{kT}\right] \ll J_1 \qquad 2.68$$

$J_2^{rev} \ll J_1$ because V_o generally is typically a fraction of a volt and the reverse bias creates more than a few volts, therefore the reverse bias current is limited by J_1 and is very small. It can be said that the current generated under the reverse bias conditions, is basically due to the thermal emission of electrons over the barrier Φ_B from the metal to the conduction band of the semiconductor as shown by equation (2.64).

The I-V characteristics then exhibits rectifying properties, which fact makes the device a diode called Schottky diode.

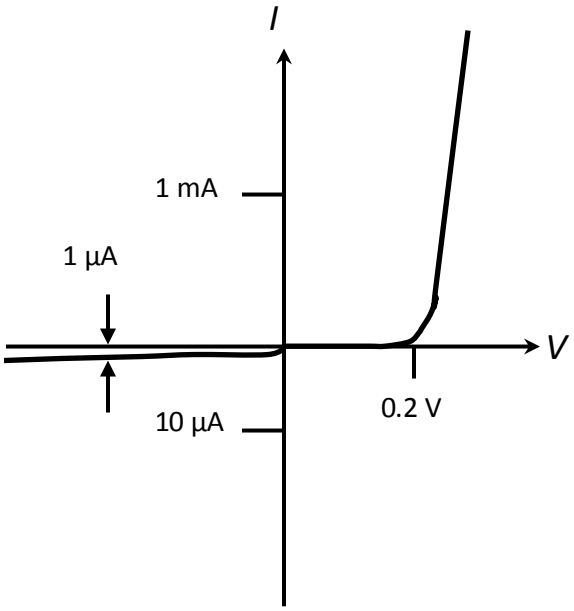

Figure 22: I-V characteristics of a Schottky junction exhibiting rectifying properties

The Schottky junction can also be obtained between a metal and a p-type semiconductor under the condition $\Phi_m < \Phi_p$, where Φ_p is the work function of the p-type semiconductor.

CHAPTER 3

MATERIALS AND EXPERIMENTAL TECHNIQUES

In this chapter we discuss the materials used for the synthesis of the CuO nano crystals. We also discuss the experimental techniques adopted in the synthesis and characterization of the nanoparticles.

3.1 Materials

In selecting a synthesis method the end use of the substance must be of prime concern and most important determining factor. In preparing CuO nanoparticles for photovoltaics, the cost factor plays an overriding role [43]. The cost factor must influence the selection of materials for the preparation of the targeted substance.

Most readily available chemical materials are inexpensive, therefore in looking at obtaining less expensive material for photovoltaic purposes, materials that can easily be obtained from the shelf of almost any Scientific chemical retail shop should become the obvious choice.

Wen et al [47], have used Cu^{2+} in synthesizing $Cu(OH)_2$ and CuO nano ribbons by solution and heat treatment processes. Simple chemical processes have been used in synthesizing CuO and Cu_2O nano materials. R. S. Patil et al [48], prepared Cu_2O thin film by modified chemical bath deposition using $CuSO_4$ and $Na_2S_2O_3$ with NaOH providing the needed pH and with heat treatment (70^oC).

In situations where heat treatment has been used in synthesizing oxides of copper, higher temperature treatment has produced Cu_2O, while lower temperature treatment has yielded both Cu_2O and CuO or CuO [46, 47]. J. Wang et al prepared cupric oxide

thin film from copper nitrate ($CuNO_3.3H_2O$), hexamethylenetetramine; HMTA ($C_6H_{12}N_4$) and hexadecyl-trimethyl-ammonium bromide; CTAB ($C_{16}H_{33}$ $(CH_3)_3Br$) with NaOH used to adjust the pH [47]. Yunling Zou et al also used CTAB assisted process to produce flower-like CuO nanoparticles [54].

If thin film of CuO could be produced from these reagents then one would want to look at varying the reaction conditions the molar concentrations so as to produce the powder. However the quest to produce CuO nanoparticles, keeping the cost of production low makes it imperative to look for reagents that are readily available. The CTAB and HMTA are not very common in our part of the world and if they were they would be expensive to procure.

M.R. Johan et al have prepared cupric oxide (CuO) thin films from copper sulphate ($CuSO_4 \cdot 5H_2O$), sodium thiosulphate ($Na_2S_2O_3$) and sodium hydroxide (NaOH) [55]

In this work copper sulphate, sodium thiosulphate and sodium hydroxide were used to synthesize CuO nanocrystals. These are all chemicals that are easily obtainable in scientific chemical shops in Ghana and are relatively inexpensive.

Among the oxides of transition metals cupric oxide has attracted huge interest due to its numerous applications in various fields, which include ; catalysis, metallurgy, high temperature super conductivity, heat transfer applications, direct solar energy conversion, field emission, magnetic storage, gas sensing, drug delivery, magnetic resonance imaging etc.

Cupric oxide for photovoltaic application ought to have competitive cost advantage over the use of nonrenewable sources for energy delivery. The first step in the

comparative cost advantage should come from the synthesis approach, ie the availability and selection of startup materials and the physical treatment of the materials to obtain the target material [48, 49].

In obtaining material for photovoltaic applications, the question of toxicity is paramount in that disposal after usage is an environmental issue. Cupric oxide is nontoxic and therefore becomes a good choice. Another important physical property of cupric oxide in addition to its low cost of preparation is the relative stability it possesses [50].

K. Kannaki et al have produced cupric oxide nanostructure from copper sulphate and ethanol by a hydrothermal process, using ammonia water to control the pH of the mixture. Here, copper hydroxide precipitate was isolated and given heat treatment which eventually decomposed producing cupric oxide [56].

D.P. Volanti et al have prepared CuO flower-nanostructure using Cu^{2+} and ammonia water via hydrothermal and microwave process [57]

3.2 Methods of Synthesis

We have successfully synthesized CuO nanoparticles using two routes:

i. the first route involved the targeted end material of CuO
ii. the second route involved the targeted cupric oxide nanoparticles.

We discuss the experimental methodology for each of these routes in turn.

All the reactants for the synthesis of CuO nanoparticles were of high grade and were procured from a trusted chemical dealer.

3.2.1 First route

The first step was to prepare various molar concentrations of the reagent for a simple chemical route synthesis. 2.0 molar concentration of each reagent was prepared. Various volumetric ratios of the 2 molar reagents were used but the results did not match expectation. Then 0.5 molar and 1 molar concentration of the reagents were prepared and various volumetric ratios used. The rationale was to try other molar concentrations as well as that which had been used by Johan et al, 2011.

Several mixture volumetric ratios, and different molar concentrations were used but the one that showed the most interesting results is described below.

1 molar of $Na_2S_2O_3.5H_2O$ and 1 molar of $CuSO_4.5H_2O$ were prepared and mixed in a volumetric ratio of 4:1 and stirred vigorously with the help of a magnetic stirrer until a clear solution formed. 1 molar NaOH was prepared and heated to about 70 ^{o}. The 70^{o}C hot NaOH is added to the mixture of $CuSO_4.5H_2O$ and $Na_2S_2O_3.5H_2O$ in the volumetric ratio of 2:5.

The colourless aqueous $Na_2S_2O_3$ when mixed with the deep blue aqueous $CuSO_4$ became prussian blue clear solution. The ions present in the solution are shown in the reaction equation below.

$$2Cu^{2+} + 4S_2O_2^{3-} \Leftrightarrow 2[Cu(S_2O_3)]^{-} + [S_4O_6]^{2-}$$

The addition of the 70^{o}C hot NaOH initially introduced greenish brown colour which faded immediately but darkened the colour of the mixture.

The final mixture formed was placed on a preheated hot plate so as to minimize the effect of Ostwald ripening and stirred continuously with close observation. Heating

over a wide range of temperature during nucleation increases the chances of Otswald ripening occurring. The heating of the mixture was done for the temperature range from 50 ^{o}C to 90 ^{o}C at different times in order to be able to observe the process well. The hot plate was heated to about 60 ^{o}C and the final mixture in a pyrex beaker was placed on it. The temperature of the mixture was monitored with the help of a thermometer at the same time the temperature of the hot plate was also adjusted and monitored to ensure that the temperature of the mixture was just about 50 ^{o}C. The same process was followed increasing the temperature by 10 ^{o}C up to 90 ^{o}C. After about 2 hours and thirty minutes, brownish black precipitates were formed at the maximum temperature of about 90 ^{o}C. The brownish precipitates turned black suspended in a colourless liquid. The suspension was allowed to settle for twenty four hours. The colourless solution was carefully poured out. The precipitates were washed thoroughly four times with deionized water to ensure that no precursor or base remained as a contaminant. Each time the precipitates were left in deionized water for twenty four hours to allow the particles to settle again. The precipitates underwent open air drying on a hot plate at about 50 ^{o}C for 48 hours to ensure that all water present had been evaporated. Leaving it to dry at room temperature was going to consume a lot more time and was also going to increase the risk of contamination. It was dried at 50 ^{o}C which was lower than the final reaction temperature so as to avoid possible conversion to some new material or agglomeration.

3.2.2 Second route

A simple chemical route synthesis of cupric oxide nanoparticles was adopted.

The molar concentrations of the reagents were prepared using the digital balance for mass measurement and the beakers for the volume of deionised water required.

7.48806 g of $CuSO_4 \cdot 5H_2O$ was added to 300 ml of deionized water to produce 0.1 M concentration of the hydrated salt.

For 0.1 molar concentration of the $CuSO_4 \cdot 5H_2O$, 100 ml of it was added to 20 ml of 30% ammonium solution and the mixture stirred vigorously with the help of a magnetic stirrer. This resulted in a deep blue clear solution. Portions of the solution were placed and stirred on preheated hot plates at various temperatures and observed closely. Although colour change (deep blue to prussian) was observed for all the temperatures, the contrast was sharpest at solution temperature of about 74 ^oC. Black precipitate formed at the base of the beaker with the rest of the solution maintaining the prussian blue colour. Upon adding a lot more 30% ammonia water the solution became clearer and eventually colourless but the black precipitate remained. The clear colourless solution was poured out of the beaker and the precipitate washed with excess deionized water , five times to ensure that no trace of the reagents remained. The precipitate was dried on a preheated hot plate at about maximum temperature of 50 ^oC for 2 hours. Black fine powder was obtained.

The same concentrations and volumetric ratios and reaction conditions were used to produce the black powder at least on five occasions to ascertain whether the path could be reproduced.

The powder was kept for at least six months to investigate whether or not there will be a colour change. There was no colour change after the period giving an indication of a very stable compound produced.

The powder was prepared for XRD analysis, optical analysis using a UV-VIS equipment and particle size analysis using TEM.

3.3 Characterization

After employing the first synthesis route, the end product was analysed to ascertain the compounds present. XRD analysis was therefore done on the product.

After the XRD analysis the particles were found to have various compounds present. These included CuO, Cu_2O, CuS and Na_2SO_4. Absorbance measurements were made on the sample with the use of the Shimadzu UVmini-1240 in order to determine the energy band gap of the sample.

3.3.1 X-ray Diffraction

Some of the powder was ground in a mortal and poured onto a clean glass slide for powder diffraction. The glass slide was flat stage inserted into the holder of the EMPYREAN XRD and the powder scanned in the range of 10 -90^o (2θ) using Cu Kα radiation with a wavelength of 1.54060 Å. The scan was performed on two different portions of the sample, the same results were obtained in each case.

The peaks obtained were analysed to obtain the crystallite size using the Scherrer equation and the Williamson-Hall plot for the average crystallite size.

3.3.2 Absorption measurement

A clean cuvette three quarters filled with DI water was placed in the UV-VIS (Shimadzu UVmini-1240) and base absorption measurement done.

Some of the powder was dispersed in a DI water and sonnicated for about two hours to ensure even distribution of particles in the solvent. Some of the suspension was poured into a clean cuvette. The cuvette was then transferred into the UV-VIS machine (Shimadzu UVmini-1240) and absorption measurement done. The absorption spectra was recorded with the help of a computer. The cuvette with the suspension was left in a closed container to enable absorption measurement done at later times. Absorption measurement was done after every two hours five times. The absorption spectra obtained was about the same in each case. The analysis of the absorption curve was done using Tauc relation to obtain the band gap of the CuO nanoparticles produced.

3.3.3 TEM

Carbon coated copper grids were obtained from Nugouchi Memorial Institute. Some of the black cupric oxide nanoparticles were suspended in DI water and sonicatted for four hours. With the help of a clean clinical syringe and a needle some of the suspension was placed on the grid. The grids were allowed to dry for three days in a covered plastic container so as to avoid contamination from the atmosphere. The dry grids were then put into the electron microscope to be scanned. The images were shot and micrographs produced for the particles.

A table top microscope was used to look at the micrographs and the average particle size of the powder determined by individual measurements. About 500 individual

particles were counted for statistical analysis for mean particle size determination and particle size distribution.

3.3.4 Thin Film Deposition

The deposition techniques for producing thin films can be classified as (i) physical and (ii) chemical. Physical deposition techniques include: sputtering, laser ablation, vacuum evaporation, molecular beam epitaxy and pulsed laser deposition, while chemical deposition techniques include: sol-gel, chemical bath, dip coating , spin coating, spray pyrolysis and cathodic electrodeposition [73 – 77].

The choice of thin film deposition method should take into consideration the end use of the film.

The deposition method should be one which involves less energy consumption so that the risk of environmental pollution from the use of non-green energy sources can be reduced.

Chemical bath deposition was chosen for this work due to its inexpensive nature. An aqueous solution made from readily available and easy to acquire chemicals makes this method of thin film deposition cheap [78]. Additionally, it does not involve heavy machinery which requires high voltages to operate, and deposition can also take place at relatively low temperatures.

The Film deposition

In order to obtain quantitative information about the as prepared cupric oxide nanoparticles prepared by chemical solution method, a thin film of cupric oxide had to be made on a glass slide employing the same simple chemical route. In that regard a solution of 0.1M $CuSo_4.5H_2O$ and 30% NH_4OH in volumetric ratio of 5:1 was used.

A 7.5 cm by 2.5 cm glass slide was used as the substrate on which the film was deposited. The glass slide was placed in a dilute nitric acid for twenty four hours to degrease it and was subsequently washed with organic solvents, acetone, 2-propanol and methanol, and was finally washed thoroughly with deionized water. The substrate was allowed to dry and was heated to about 40 ^oC and was immersed in the solution of 0.1 M $CuSO_4 \cdot 5H_2O$ and 30% NH_4OH in a volumetric ratio of 5:1on a preheated hot plate with the help of retort stand arrangement a sketch of which is shown below in figure 23. The substrate was preheated to minimize the competition between the heterogeneous nucleation at the substrate and the homogenous nucleation that occurs within the solution which leads to deposition on the walls of the container [78]. A magnetic stirrer was used to stir the mixture. A stop clock was employed to time the process of deposition whiles a thermocouple and a liquid in glass thermometer were used to monitor the temperatures of the hot plate and that of the chemical bath respectively. The final temperature of the hot plate was 126 ^oC and that of the 30% NH_4OH and 0.1 $CuSO_4$ solution was 54 ^oC. The film deposition process took place in about 46 minutes. The glass slide with the thin film of CuO was removed from the solution and washed immediately with deionized water to ensure that remnant of the solution is removed. The film was allowed to air dry for 24 hours and afterward annealed in air for about 40 minutes at a temperature of 50 $^oC \pm 1$ ^oC.

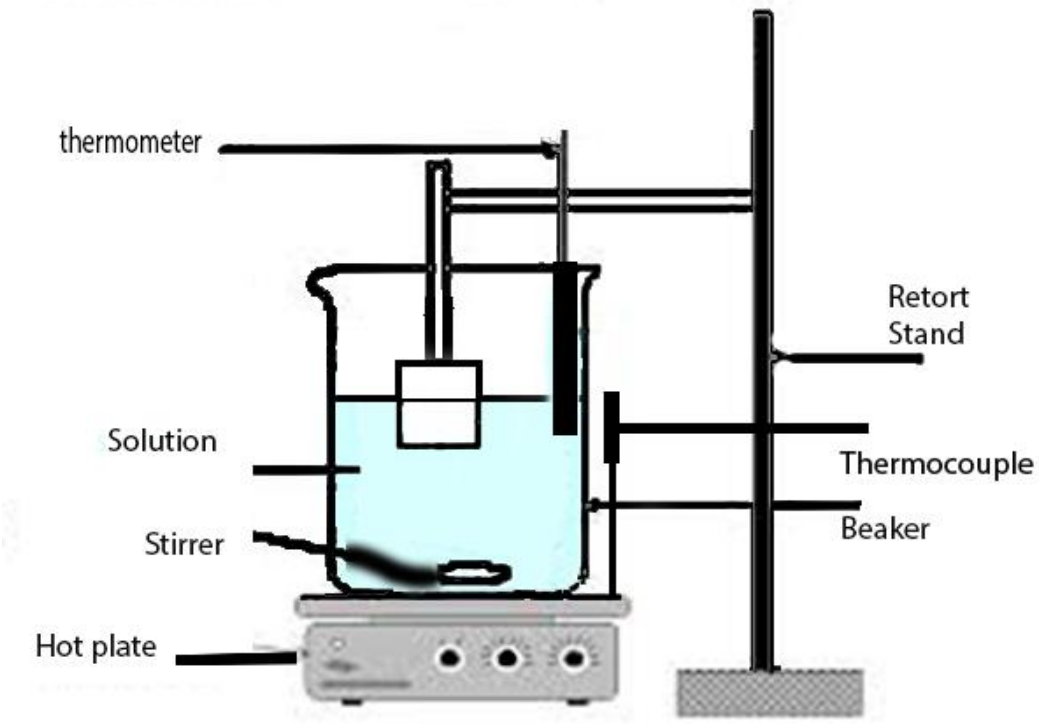

Figure 23: Set up for chemical bath deposition

3.3.5 Electrical conductivity and resistivity measurements

To be able to ascertain the suitability of the material deposited on the glass to be used in photovoltaic applications, voltage and current measurements were done on the thin film to ascertain the conductivity potential of the as prepared CuO nanoparticles. The thin film was connected in series to a power source and an ammeter, and had a voltmeter connected across it. The measurements were done first, in a dark environment at room temperature and then in a normal day light environment also at room temperature.

The film was subjected to a changing temperature environment by bringing a hot plate under it and turning it on. The current and voltage values were recorded for the changing temperature environment, the temperature values were also recorded.

Radiation of various wavelengths were incident on the thin film independently to monitor their individual influence on the values of current and voltage recorded from the arrangement. The variation in wavelengths of the incident radiation was achieved with the use of a uv-vis spectrophotometer (Shimadzu UVmini-1240) put in the photometric mode. The Shimadzu UVmini-1240 sample compartment provided the dark room environment required.

The thickness of the film was also determined using Fizeau fringes, an optical technique for measuring film thickness. The thin film was placed on a reflective reference plate, this arrangement receives light from and reflect it back through the beam spliter. Parrallel interference pattern is observed with a step at the edge of the film and the rest of the glass side carrying the film. The interference pattern or the fringes are seen in the eyepiece of a traveling microscope. A vernier scale attached to the traveling microscope is used to measure the fringe thickness and the displacement caused by the step introduced by the thin film substrate junction. The setup is illustrated in figure 24 below.

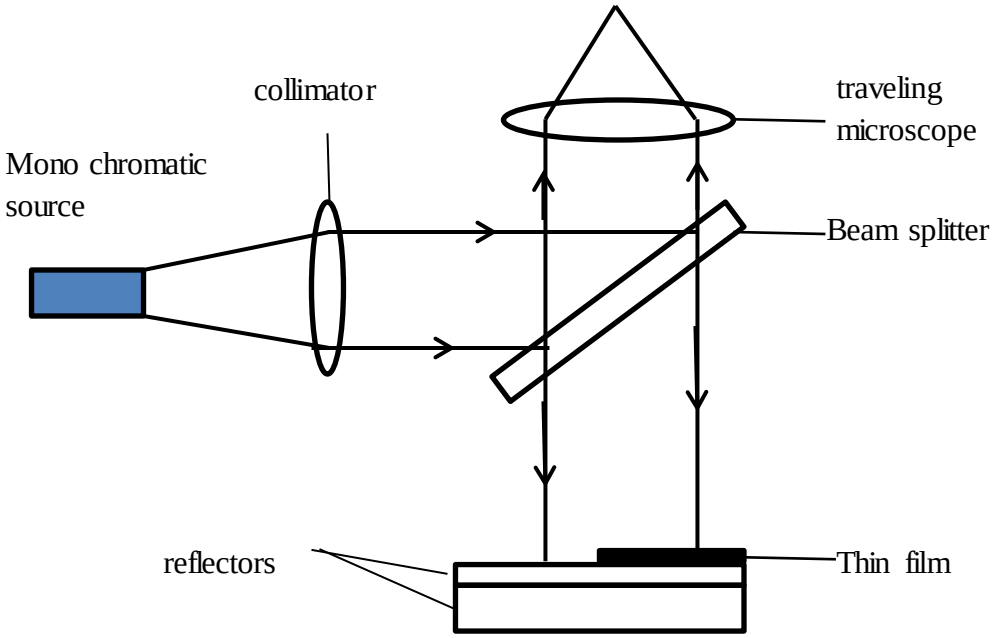

Figure 24: Set up for measurement of film thickness

From

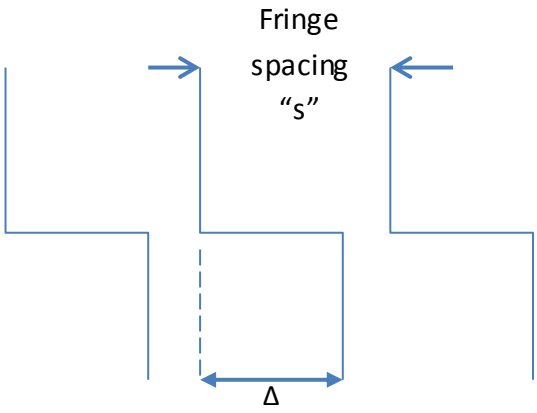

Film thickness d is given by

$$\boldsymbol{d = \frac{\Delta}{S} \cdot \frac{\lambda}{2}}$$

where s is fringe spacing, Δ fringe displacement and λ, the wave length of the monochromatic light obtained from sodium lamp. From several measurements, an average value of d was calculated to be $(1.47 \times 10^{-6} \pm 8 \times 10^{-8})$ m.

CHAPTER 4

RESULTS AND ANALYSIS

4.1 Band gap measurement

UV-visible absorption of as-synthesized cupric oxide nanoparticles produced by simple chemical reaction in an aqueous medium has been recorded in almost the entire visible to near infra- red region and they are illustrated below.

The spectrum has one peak centered around 314 nm, which indicates that the as-synthesized cupric oxide nanoparticles absorbs in the ultra violet region, a good optical property of a material that is needed for photovoltaic applications.

Several absorption measurements were carried out on the sample. In all samples, the peak in the absorption spectra centered around a mean wavelength value of 314 nm except that the absorbance dropped for situations where the cuvette and its content were left to stand for hours and days. Five absorbance graphs are presented below in figures 25 – 29, showing that the peak in all cases was just around 314 nm as stated above. The drop in absorbance could be attributed to the effect of gravity on the relatively more massive particles. In spite of that, the small size of the particles kept quite a large number suspended, enough to give a characteristic absorption spectrum each time measurements were made.

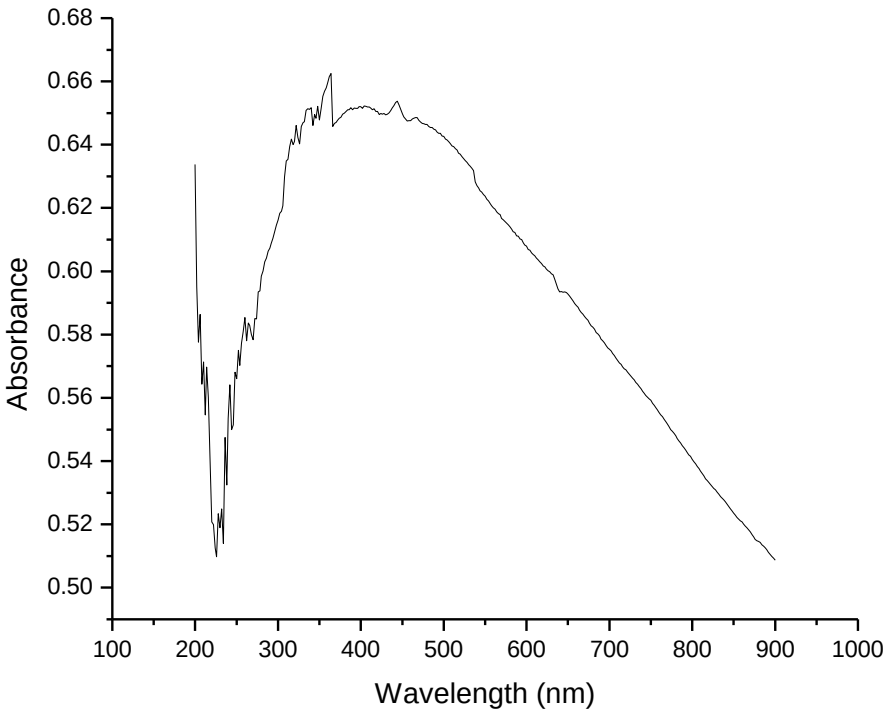

Figure 25: A UV-VIS absorption spectrum of as synthesized black cupric oxide nanoparticles. The scanning was done right after the suspension of sample in dionized water had been sonicatted.

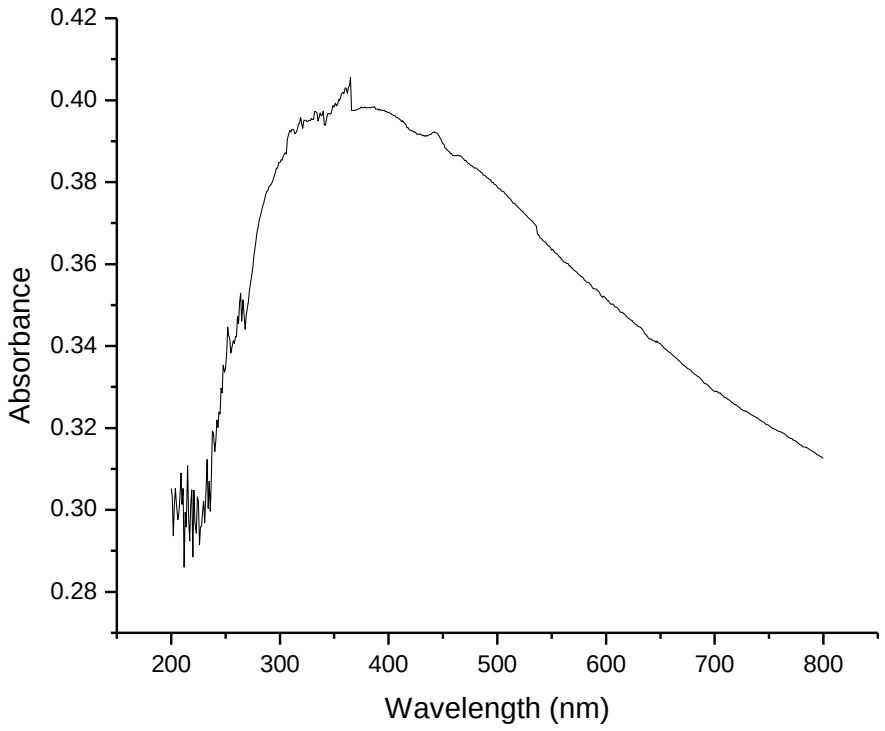

Figure 26: A UV-VIS absorption spectrum of as synthesized black cupric oxide nanoparticles obtained from suspension one hour after sonication.

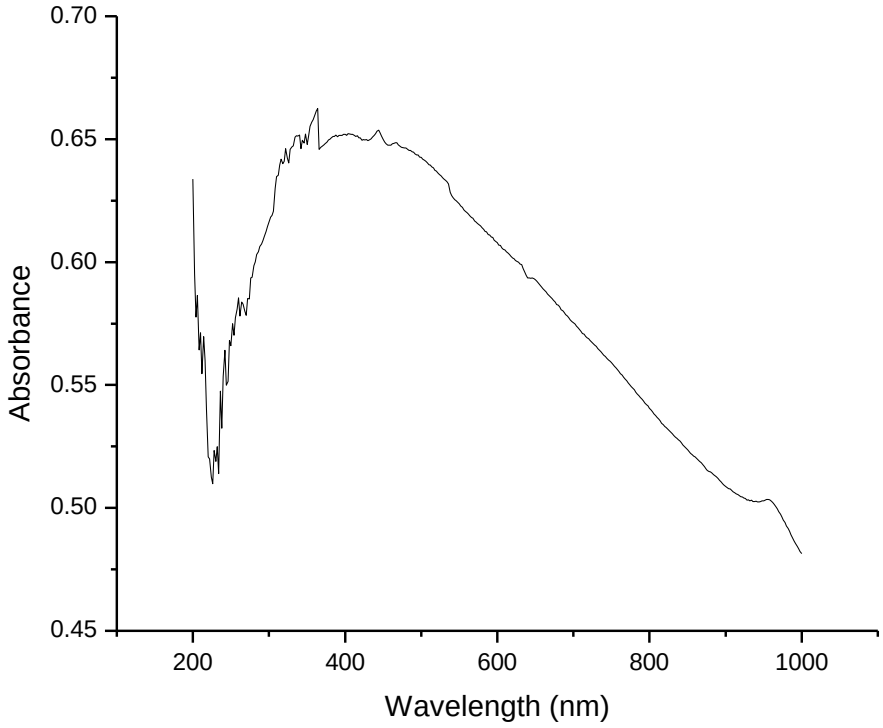

Figure 27: A UV-VIS absorption spectrum of as synthesized black cupric oxide nanoparticles obtained after the cuvette and its content had been allowed to stand for thirty minutes.

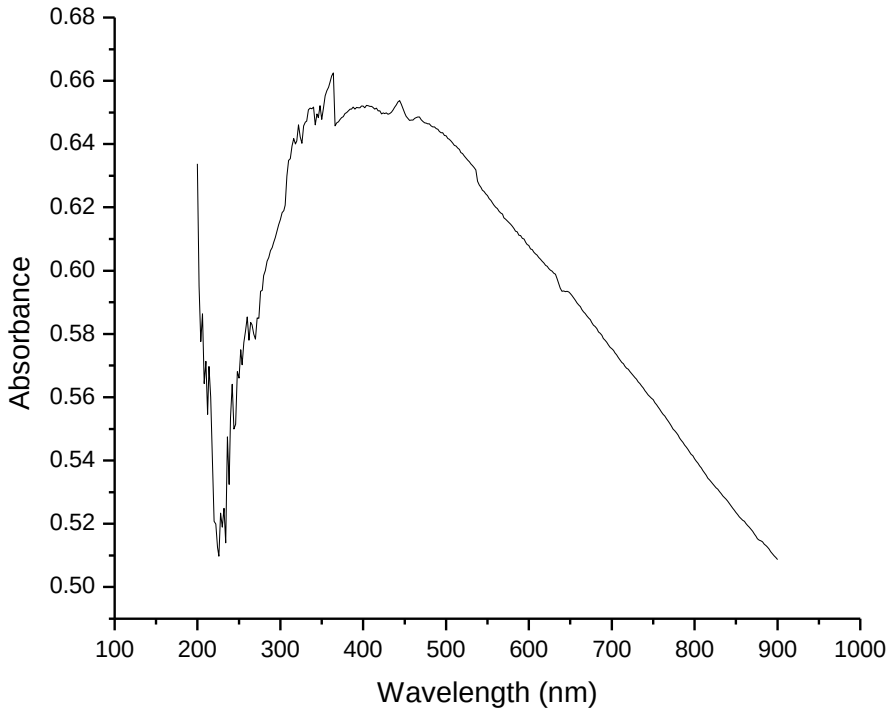

Figure 28: A UV-VIS absorption spectrum of as synthesized black cupric oxide nanoparticles obtained after cuvette and its content was allowed to stand for fifteen minutes.

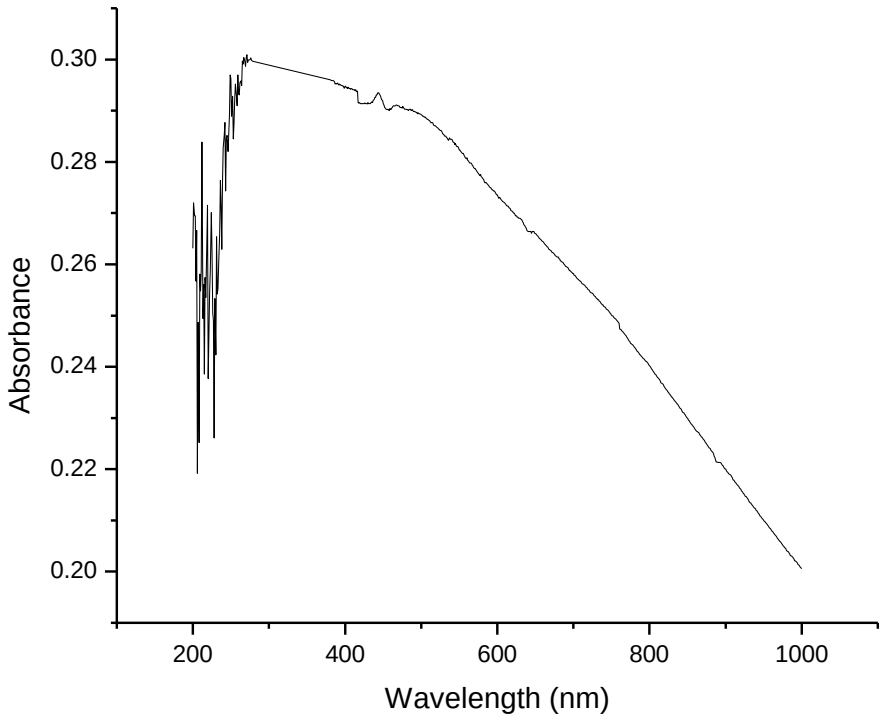

Figure 29: A UV-VIS absorption spectrum of as synthesized black cupric oxide nanoparticles obtained after the sample of the as prepared cupric oxide has been used to spin coat a microscope slide on one surface.

Peak absorbance wavelength (nm)	320	320	320	320	290	Mean (nm) 314
Deviation (nm)	6	6	6	6	-24	

Table2 : Tabulated Peak absorbance wavelengths obtained from absorbance measurements.

The standard error in the mean wavelength associated with the peak absorbance has been calculated to be ± 5.78 nm.

The band gap energy of a given material is an important determinant for a semiconductor material, whether it is p-type or n-type. The band gap energy of the as prepared cupric oxide has been determined with the help of the Tauc's relation [86]. This has been achieved by using several absorption measurements (five of which have been presented) and the mean value obtained for the band gap.

From Tauc's relation

$$\alpha hv = \left(hv - E_g\right)^n$$

where α is the absorption coefficient, v is the frequency of the incident photon, h is the Planck's constant and n is 0.5 or 2 for direct and indirect transitions respectively

a Tauc's plot, $(\alpha hv)^2$ versus hv, which provides the best linear relationship for direct transition, was used to obtain the optical band gap of the as-prepared cupric oxide nano particles. The numerical value of the band gap is obtained from the straight line drawn from the most linear part of the curve cutting the hv axis, where $\alpha = 0$. From the Tauc's plots in figures 30 to 34, the mean optical band gap of the as prepared cupric oxide was calculated to be about 1.48 ± 0.04 eV. This band gap value is slightly higher than the 1.37 eV obtained by Ooi et al [80] but lower than band gap values obtained by Pierson et al [84] and Ogwu et al [71] which were 2.11 and 2.05 eV respectively.

It also falls within the range of value for the bulk CuO, from 1.0-1.5 eV but is far less than the reported value of 2.4 eV [55].

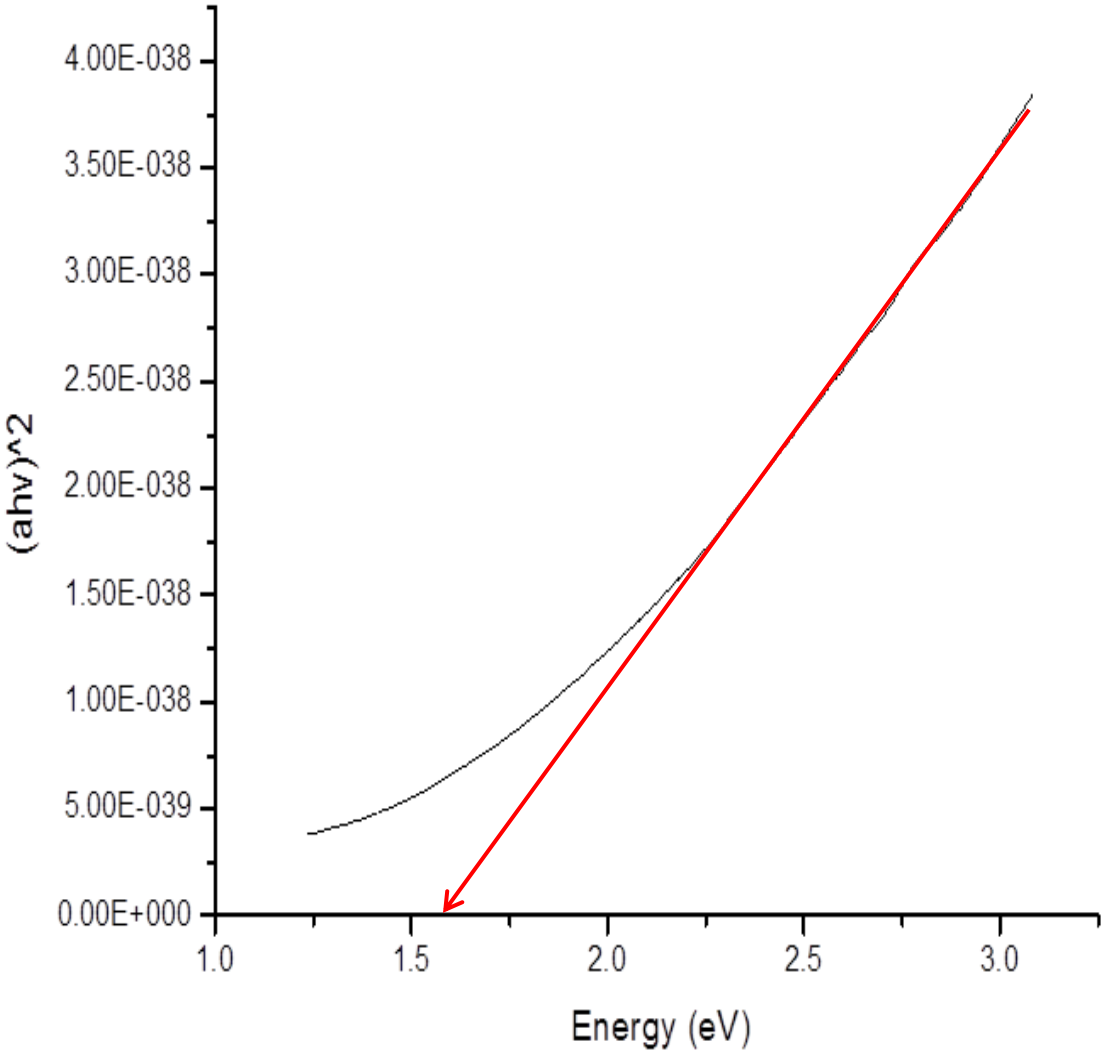

Figure 30: Tauc's plot (1) for as prepared CuO nanoparticles

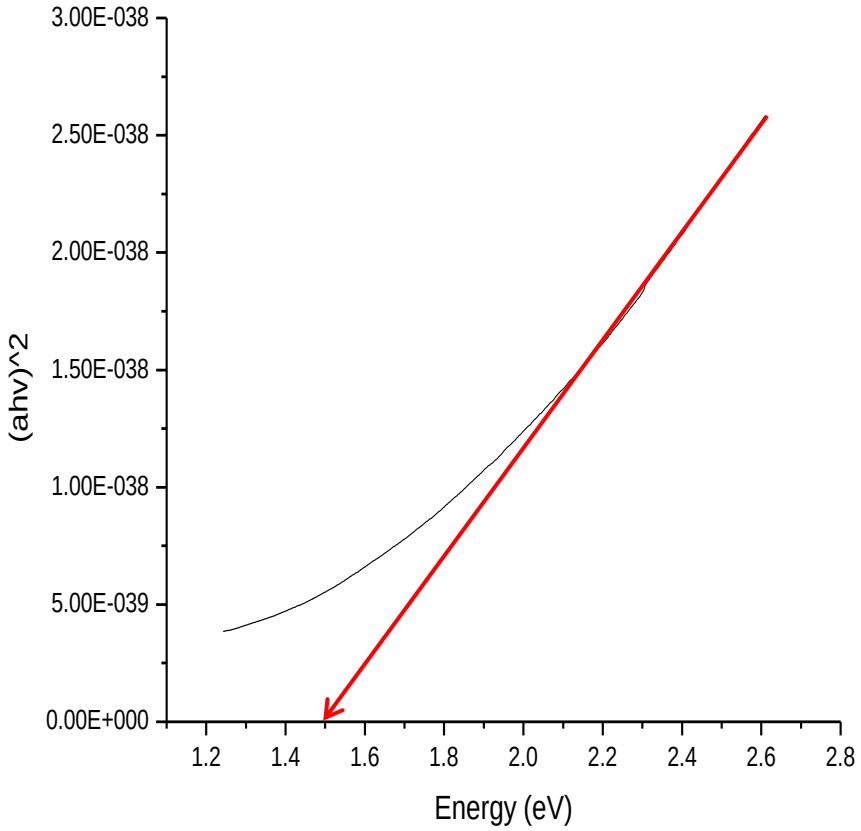

Figure 31: Tauc's plot (2) for as prepared CuO nanoparticles

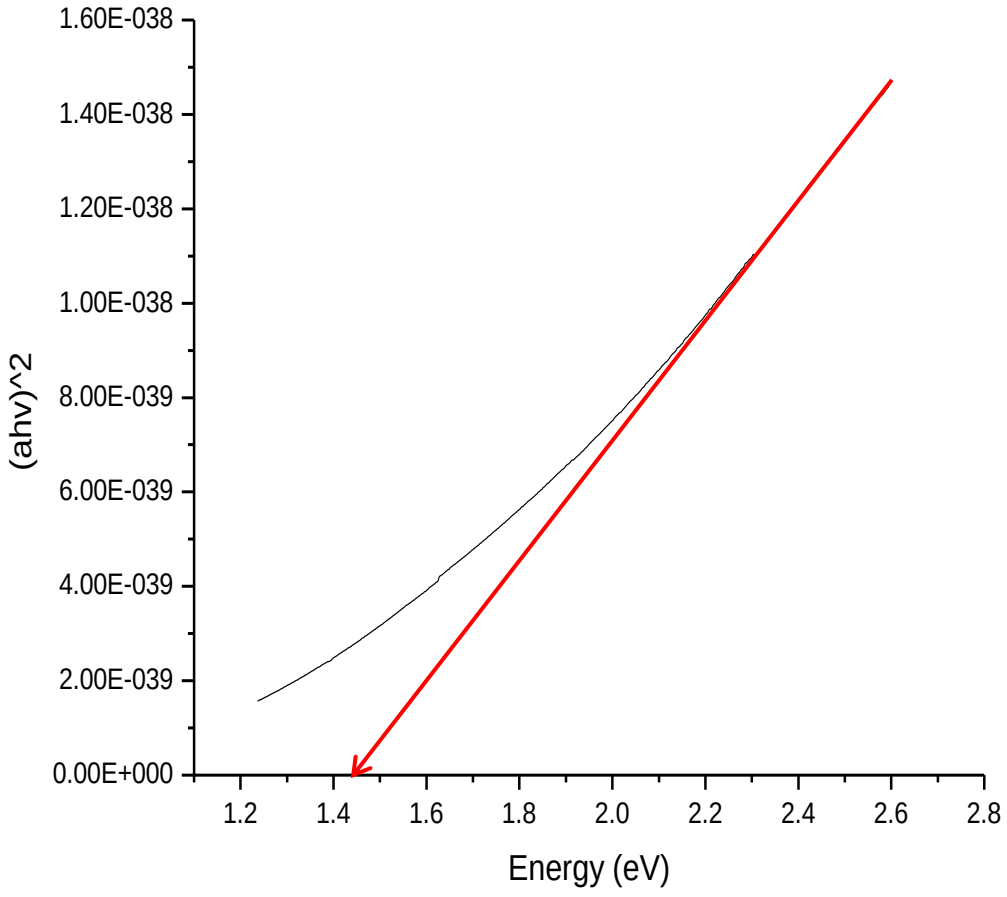

Figure 32: Tauc's plot (3) for as prepared CuO nanoparticles

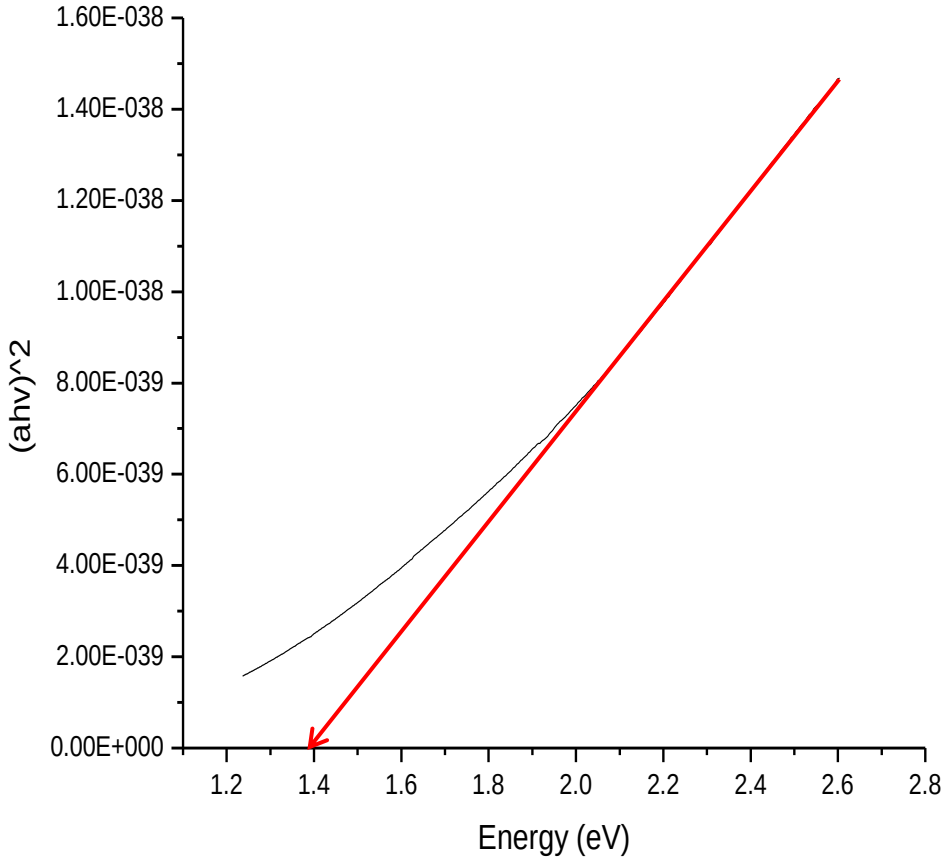

Figure 33: Tauc's plot (4) for as prepared CuO nanoparticles

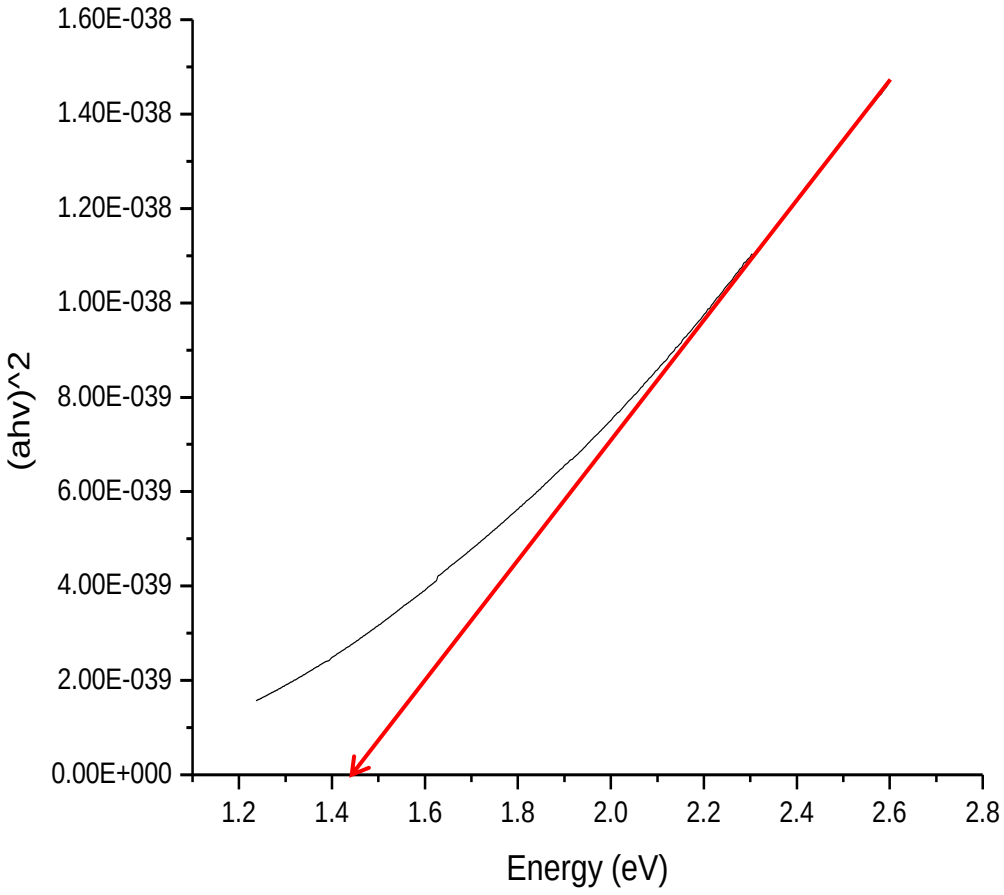

Figure 34: Tauc's plot (5) for as prepared CuO nanoparticles

Energy band gap values obtained from Tauc's plot (eV)	1.60	1.50	1.45	1.40	1.45	Mean (eV) 1.48
Deviation	-0.12	-0.02	0.03	0.08	0.03	

Table 3: Band gap energy values for the as prepared cupric oxide nanoparticles

The standard error in the mean energy band gap has been calculated to be ± 0.04.

4.2 XRD Analysis

4.2.1 X-ray Diffraction pattern Peak Broadening Analysis

In nanocrystalline materials, the random orientation of the crystals is responsible for the broadening of diffraction peaks.

XRD pattern of the as synthesized cupric oxide nano particles dried at 50 ^{o}C is shown in figure 35 below. The XRD data was analysed using the High Score software. The table 4 below provides the following information on the as synthesized cupric oxide nanoparticles; observed diffraction peaks positions (2θ), observed full width at half maximum (FWHM), as determined from the XRD data using the High score software, and d-spacing or the crystallite size related to the individual diffraction peaks obtained from the Scherrer equation. The grain or crystallite sizes for the various FWHM values have all been shown in the table. The High score software gave an indication of all cupric oxide crystals as per the diffraction by the Emperean, showing clearly that, the as prepared particles are cupric oxide nanoparticles.

Broadening of the peak has two sources; instrumental and observed which depends on the orientation of the crystals. The instrumental broadening can be determined by the use of the diffraction pattern of a standard material. The subtraction of the standard results from what is obtained from a given X-ray machine provides the instrumental broadening. [56]

The Scherrer Equation helps to obtain an approximated value for the crystallite size due to the fact that the broadening of the peaks due to sample dependent effects is not factored in the equation.

The d-spacing D according to Scherrer is given by the relation

$$D = k\lambda/\beta cos\theta$$

Where λ is the wavelength of the x-rays used, β is the full wave at half maximum of the reflection per peak, k is a constant (shape factor) with a numerical value of 0.9 [53]. The High Score software employed the Scherrer relation to obtain the d-spacing

for the individual peaks as indicated in table 4 below. The d-spacing ranged from 13.1 to 27.6 nm. From the Scherrer calculations, the average crystallite size is evaluated to be 18.4×10^{-9} nm.

4.2.2 The Williamson-Hall Plot

The Williamson-Hall plots which convolutes the Lorentz or the Gaussian profile enables the determination of the average grain or crystallite size.

With respect to the Bragg angle θ, the approximate formula for size broadening β_L differs from the strain broadening β_e, and represented respectively by the relations below.

$$\beta_L = \frac{K\lambda}{Lcos\theta}$$

and

$$\beta_e = C\varepsilon tan\theta$$

$$\beta_{tot} = \beta_L + \beta_e$$

$$= \frac{K\lambda}{Lcos\theta} + C\varepsilon tan\theta$$

$$\beta_{tot} cos\theta = \frac{K\lambda}{L} + \eta sin\theta$$

where ε is micro strain associated with the material and C is a constant

A graph of $B_{tot}Cos(\theta)$ against $Sin\theta$ gives a straight line with an intercept equal to

$$\frac{k\lambda}{L}$$

and the gradient equivalent to η.

In table 6, β_{tot} is represented as FWHM.

In that same table $\beta_{tot} cos\theta$ and $sin\theta$ have been computed.

Peak List

Pos.[°2Th.]	Height [cts]	FWHMLeft[°2Th.]	d-spacing [Å]	Rel. Int. [%]
32.4354	493(24)	0.5904	2.75809	7.87
35.4856	6097(47)	0.3444	2.52769	97.45
38.6838	6257(36)	0.6396	2.32575	100.00
48.8764	825(17)	0.8856	1.86192	13.19
53.5889	294(18)	0.5904	1.70877	4.69
58.2309	414(16)	0.7872	1.58312	6.62
61.4033	904(20)	0.5904	1.50871	14.45
66.0648	1171(17)	0.9840	1.41310	18.71
68.2960	630(17)	0.7872	1.37227	10.07
72.1657	23(12)	0.9840	1.30791	0.36

Table 4: Various parameters obtained from XRD measurements

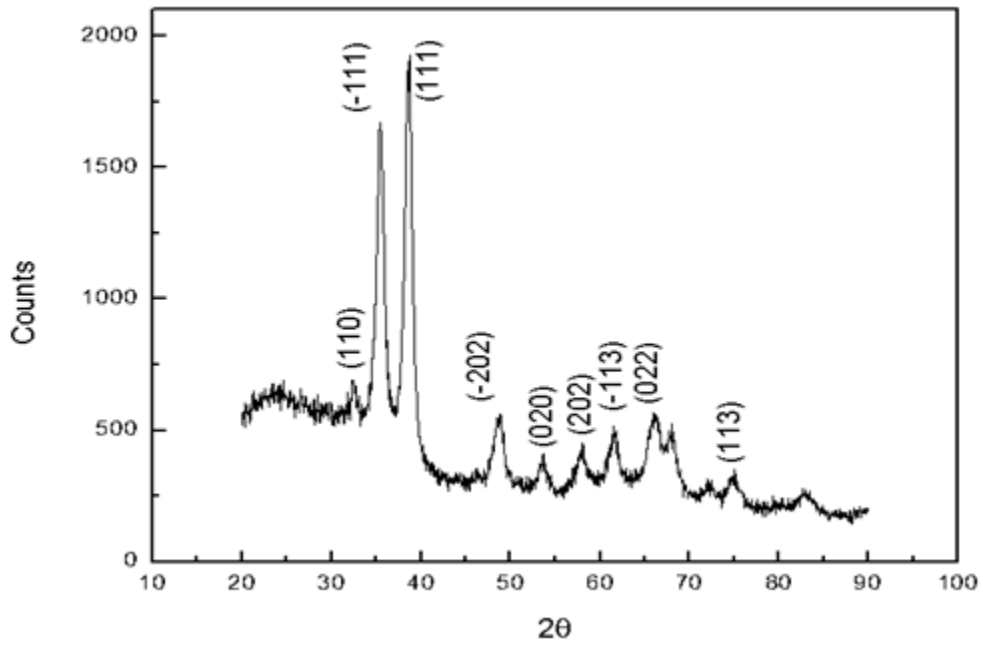

Figure 35: XRD spectrum of as synthesized cupric oxide nanoparticles

Peak List

Pos.[°2Th.]	Height [cts]	FWHMLeft[°2Th.]	d-spacing [Å]	Rel. Int. [%]
32.4354	493(24)	0.5904	2.75809	7.87
35.4856	6097(47)	0.3444	2.52769	97.45
38.6838	6257(36)	0.6396	2.32575	100.00
48.8764	825(17)	0.8856	1.86192	13.19
53.5889	294(18)	0.5904	1.70877	4.69
58.2309	414(16)	0.7872	1.58312	6.62
61.4033	904(20)	0.5904	1.50871	14.45
66.0648	1171(17)	0.9840	1.41310	18.71
68.2960	630(17)	0.7872	1.37227	10.07
72.1657	23(12)	0.9840	1.30791	0.36

Pattern List

Visible	Ref.Code	Score	Compound Name	Displ.[°2Th]	Scale Fac.	Chem. Formula
*	01-080-0076	77	Copper Oxide	0.000	0.994	Cu O

Table 5: Peak list and the corresponding Pattern list from XRD measurement.

2θ	FWHM°	FWHM (rad)	θ°	θ (rad)	Cosθ (rad)	FWHMcosθ (rad)	sinθ (rad)
32.4356	0.5904	0.010304	16.2178	0.120912709	0.99269896	0.01022877	0.120618303
35.4856	0.3444	0.00601	17.7428	0.132282431	0.99126343	0.005957493	0.131896975
38.6838	0.6396	0.011163	19.3419	0.14420461	0.989620521	0.011047134	0.143705341
48.8764	0.8856	0.015456	24.4382	0.182200358	0.983447382	0.015200163	0.181193947
53.5889	0.5904	0.010305	26.79445	0.199767511	0.98011274	0.010100062	0.198441471
58.2309	0.7872	0.013739	29.11545	0.217071855	0.976532273	0.013416577	0.215371122
61.0648	0.5904	0.010305	30.5324	0.227636004	0.974202612	0.010039158	0.225675145
66.0648	0.984	0.017174	33.0324	0.246274893	0.967766053	0.016620414	0.243792949
68.296	0.7872	0.013739	34.148	0.254592311	0.967766053	0.013296138	0.251850882
72.1657	0.984	0.017174	36.08285	0.269017693	0.964032444	0.016556293	0.265784589

Table 6: Data obtained from the original XRD measurements

From the data above the Williamson-Hall plot has been obtained from the Lorentz convolution giving a straight line represented by $Y = 0.045X + 0.0033$ as shown in the graph1 below.

The plot gives intercept on the FWHMcosθ (rad) as 0.0033 and a gradient of 0.0451. From these figures the average crystallite size or d-spacing and the strain were computed as shown below.

$$0.0033 = \frac{k\lambda}{L}$$

$$\Rightarrow L = \frac{k\lambda}{0.0033}$$

where k isconstant (shape factor, about 0.9), λ the wavelength of the Cu anode K-alpha x-ray used for the diffraction has a numerical value of 1.54060 Å.

$$L = \frac{0.9 \times 1.5 \times 10^{-10}}{0.0033}$$

$$L = 4.09 \times 10^{-8}\ \text{m}$$

$$L = 40\ \text{nm}$$

The strain was obtained from the gradient as

$$\eta = 0.0451$$

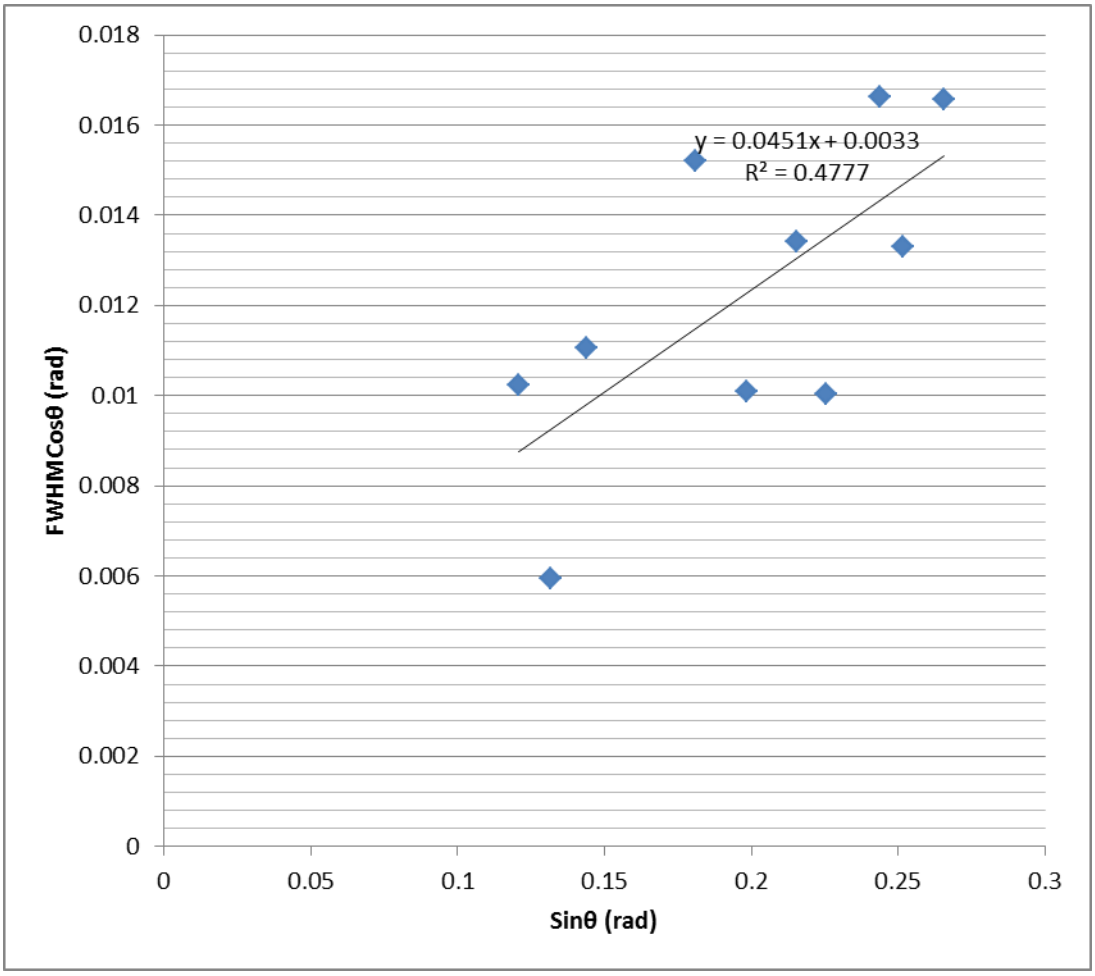

Figure 36: A graph of FWHMcosθ (rad) against Sinθ (rad)

4.3 Results From TEM measurements.

The micrograms were obtained from shots taken at various points during the TEM measurement were put under an optical microscope and the individual measurements made on the particles as they appeared on the microgram. These measurements were tallied and a histogram plotted for the determination of size distribution of the as-prepared CuO nanoparticles. The microgram is shown below in figure 37 below.

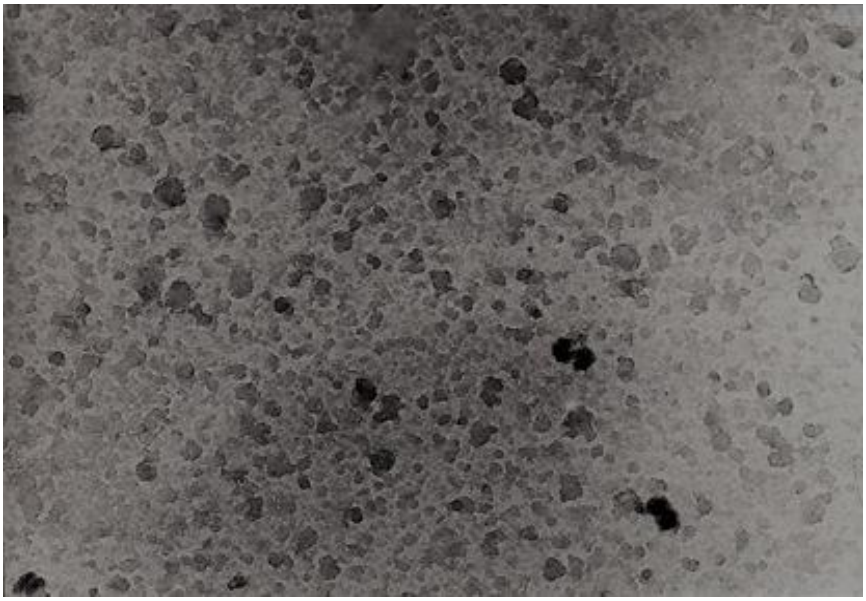

Figure 37: TEM image of CuO nanoparticles [×50,000]

The particle size distribution data obtained from the TEM image, counting more than 500 particles have been presented in both tabular and graphical form.

Mean (nm)	52.2
Median (nm)	25.0
Mode (nm)	22.2
Standard deviation	32.1
Range (nm)	50.0
Minimum (nm)	5.6
Maximum (nm)	55.6
Count	522

Table 7 : The particle size data extracted from the TEM micrograph

A number frequency histogram of the particle size data in a linear scale has been plotted. The histogram can give a valid size frequency curve drawn through it if and only if hundreds of particles say between 500 and 1000 are measured to give statistically useful mean size data. [66, 67]

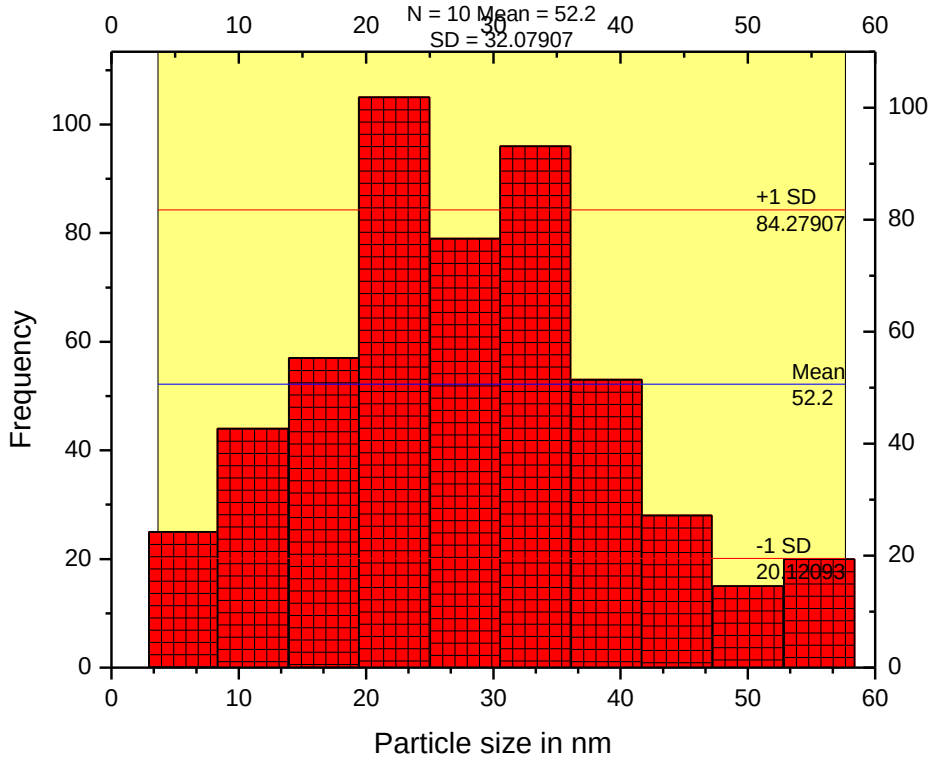

Figure 38: Number frequency histograms showing particle size distribution. The particle size data is collected from image analysis of more than 500 particles.

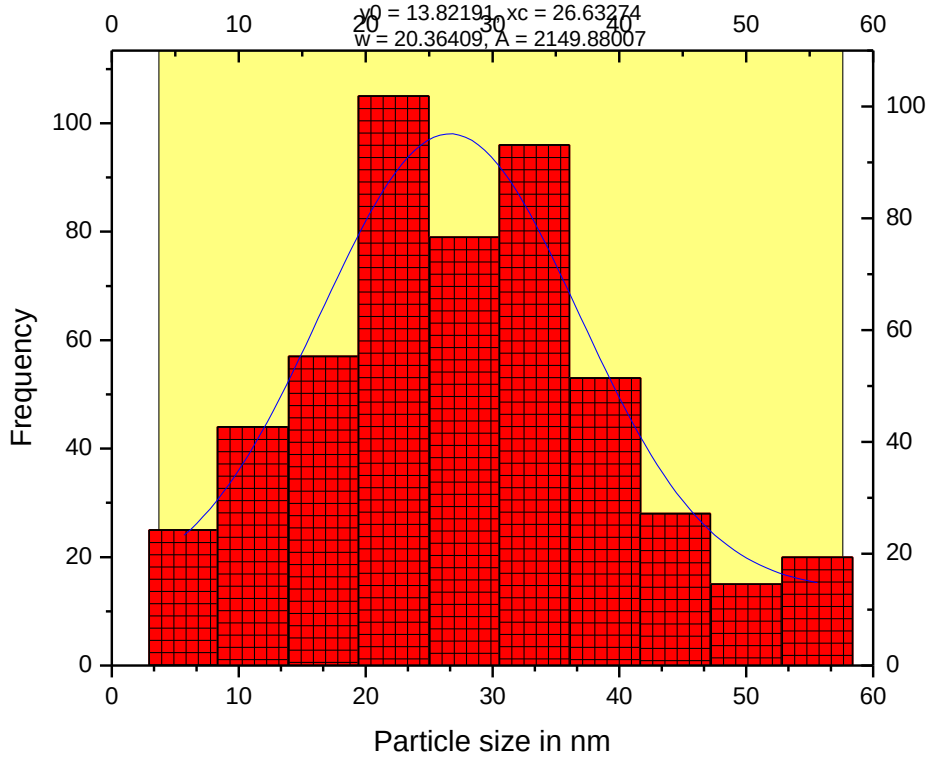

Figure 39: Number frequency histograms showing particle size distribution with a Gaussian fit line in blue. The particle size data is collected from image analysis of more than 500 particles.

From the histogram in figure 38, the particle size distribution is approximately even over the entire selected size population. The mean particle size as obtained for the histogram is 52.20 nm with a standard deviation of 32.07 . The histogram reveals the particle size range, however that is not enough for obtaining mathematical formula to fit the distribution due to shape changes with particle number. To investigate whether the particle distribution reflects Guassian and log-normal distribution, the results are

plotted also as cumulative percentage frequency curves with linear and logarithmic scales respectively. The advantages derived from these plots include the ease with which one can estimate median and standard deviation, and also obtaining a fiiting mathematical formula for the distribution.

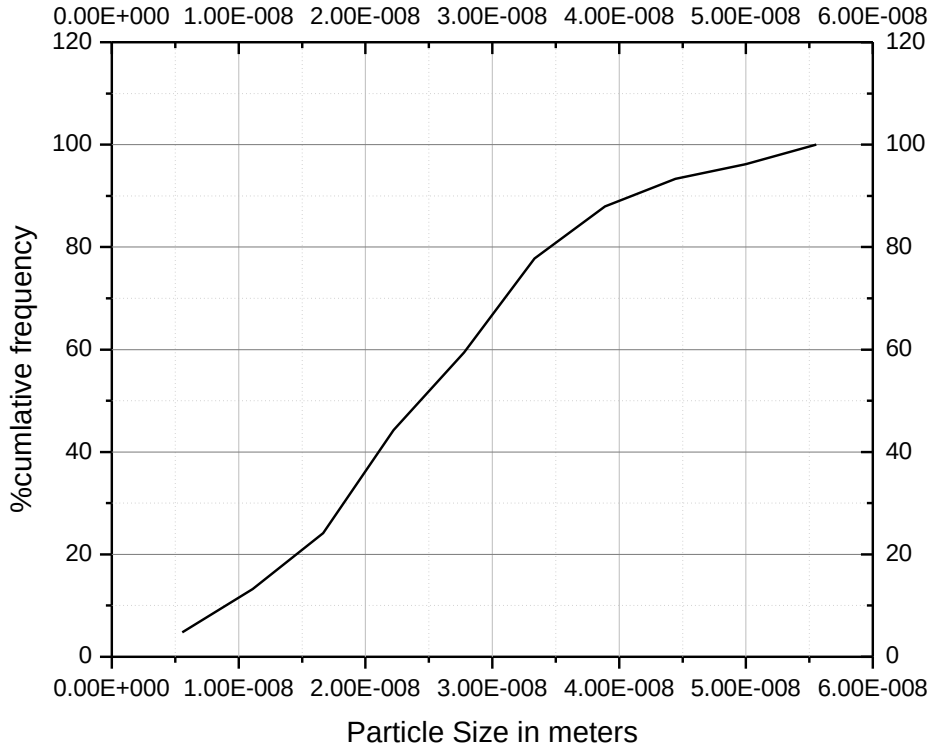

Figure 40: Cumulative percentage frequency curve with particle size axes in linear scale

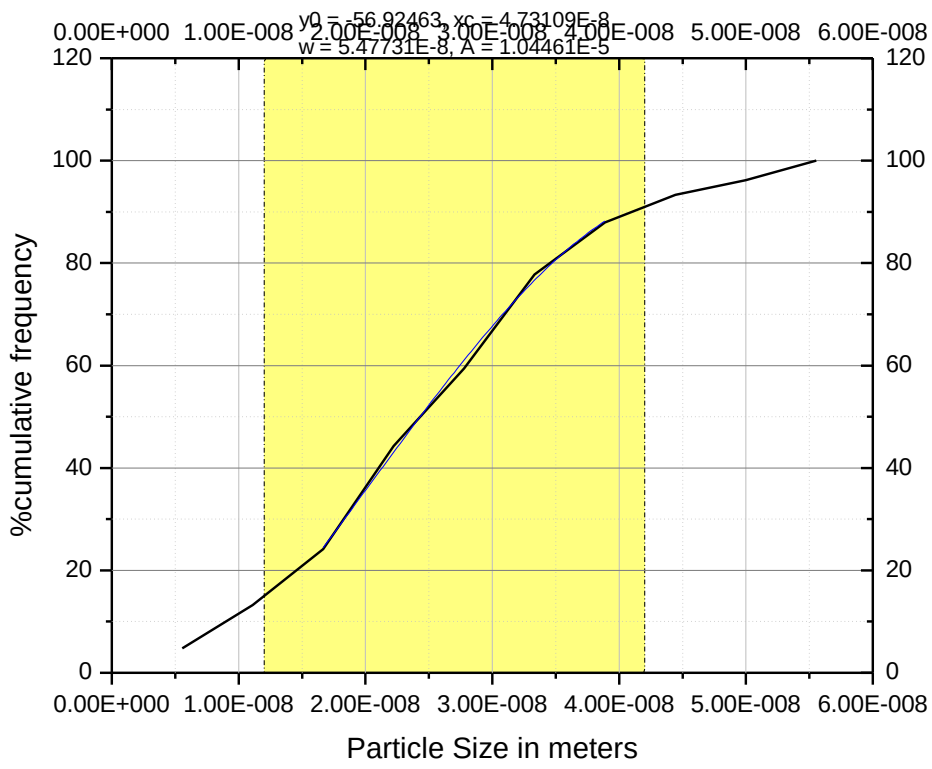

Figure 41: Cumulative percentage frequency curve with particle size axes in linear scale with the blue solid line reflecting Gaussian distribution.

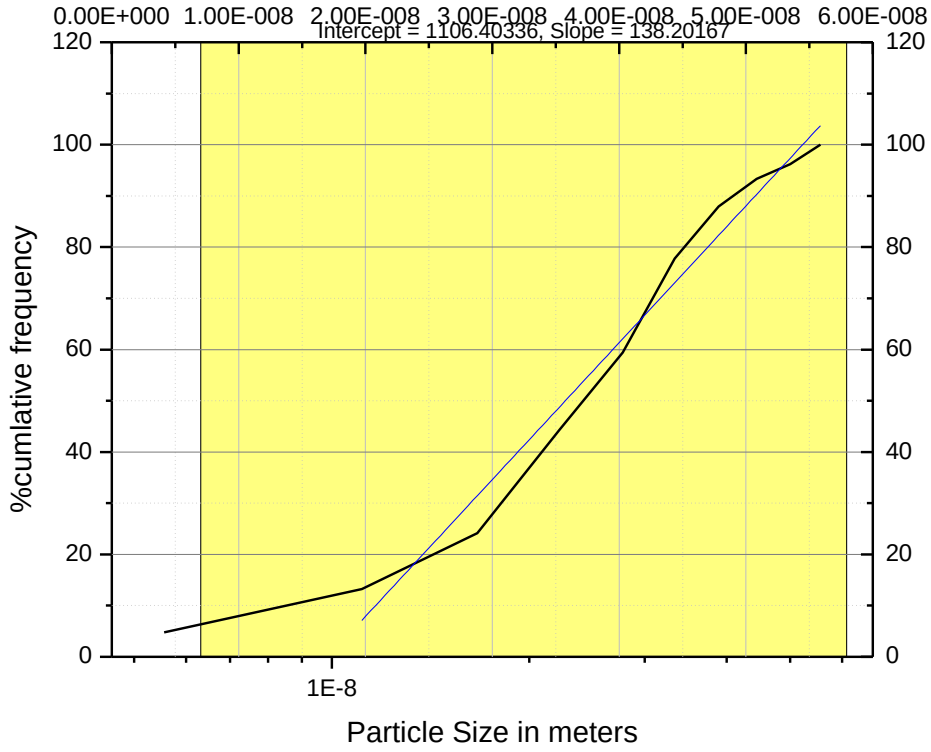

Figure 42: Cumulative percentage frequency curve with particle size axes in logarithmic scale with blue solid line reflecting log-normal distribution.

In figures 41 and 42, the blue lines represent the fitting for the particle distribution in the respective scenarios. A distribution should have a straight line fit if it is governed by a normal or Guassian distribution formula. In figure 41 the fitting is linear, and is better than what it is in figure 42. This means that the particle distribution is more

closely described by the Gaussian distribution formula more than the log-normal distribution formula.

4.3.1 Morphology

The morphology of the as-prepared CuO nanoparticles can be characterized by different factors. The irregularity parameter (IP) concept is applied to estimate the sphericity of the particles.[56, 57] The concept is used when the particle size is determined by microscopy. The as-prepared CuO nanoparticles were subjected to SEM analysis which helped with the determination of particle size and size distribution. From the SEM image it can be said that the particles are approximately spherical. For morphology such as wires and tubes, the IP can be determined as the ratio of major axis (length) to minor axis (thickness or diameter for wires with circular cross section)

$$IP = Major\ axis/Minor\ axis$$

For a sphere, the Major axis and the Minor axis are about equal in magnitude, therefore for a perfect sphere, the IP is 1.

4.3.2 Stability of as-prepared Cupric Oxide

The as-prepared black cupric oxide has been found to be very stable at room temperature, in that after the final preparation and the compound had been dried, the dry powder was kept for well over eight months. After the period the compound has been found to maintain its black colour and is still dry without absorbing moisture from the atmosphere.

4.3.3 I-V Characteristics; resistivity and conductivity of material

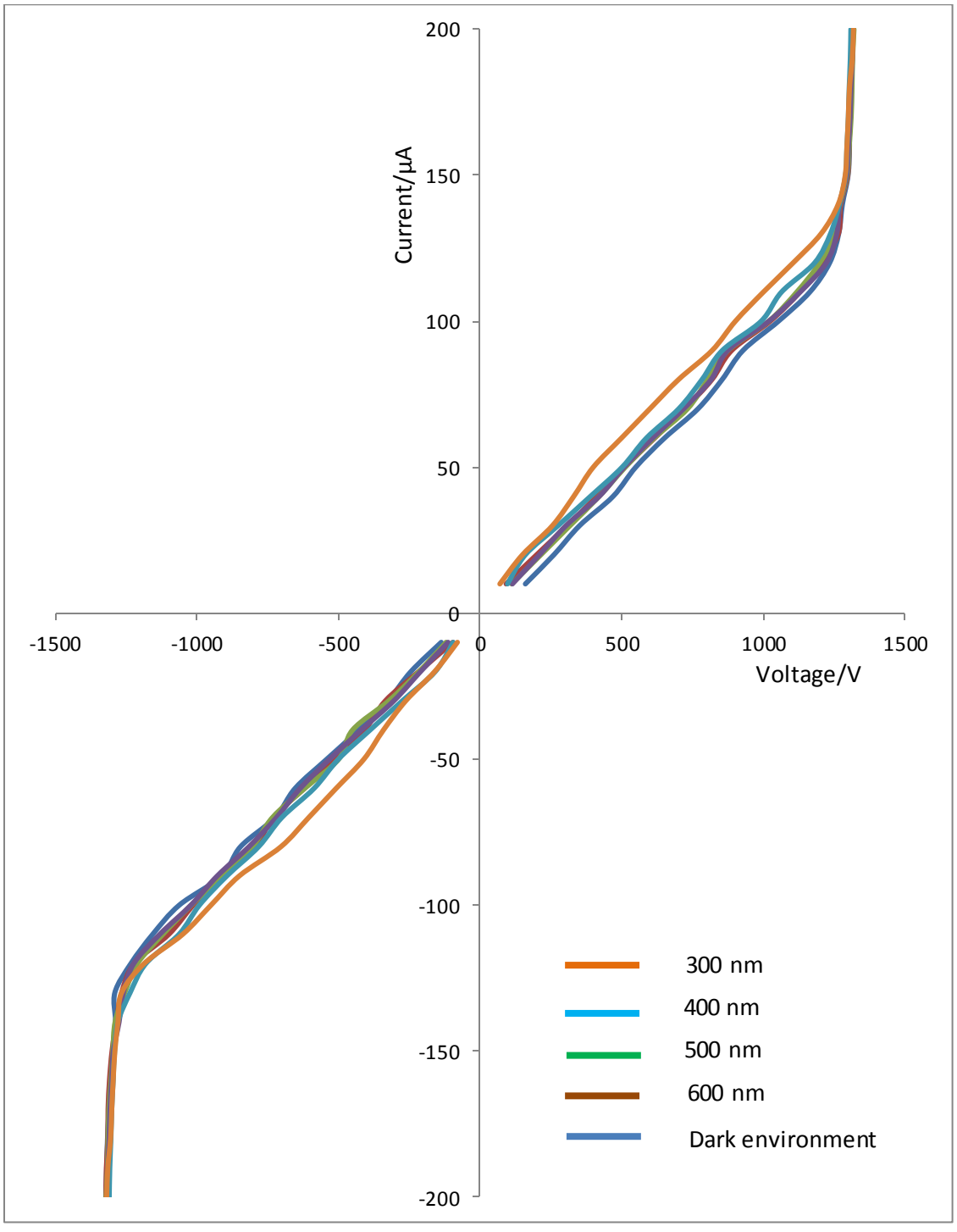

Figure 43: I-V characteristics of the CuO thin film in (i) dark environment and(ii) when 300 nm – 600 nm radiation is incident on it.

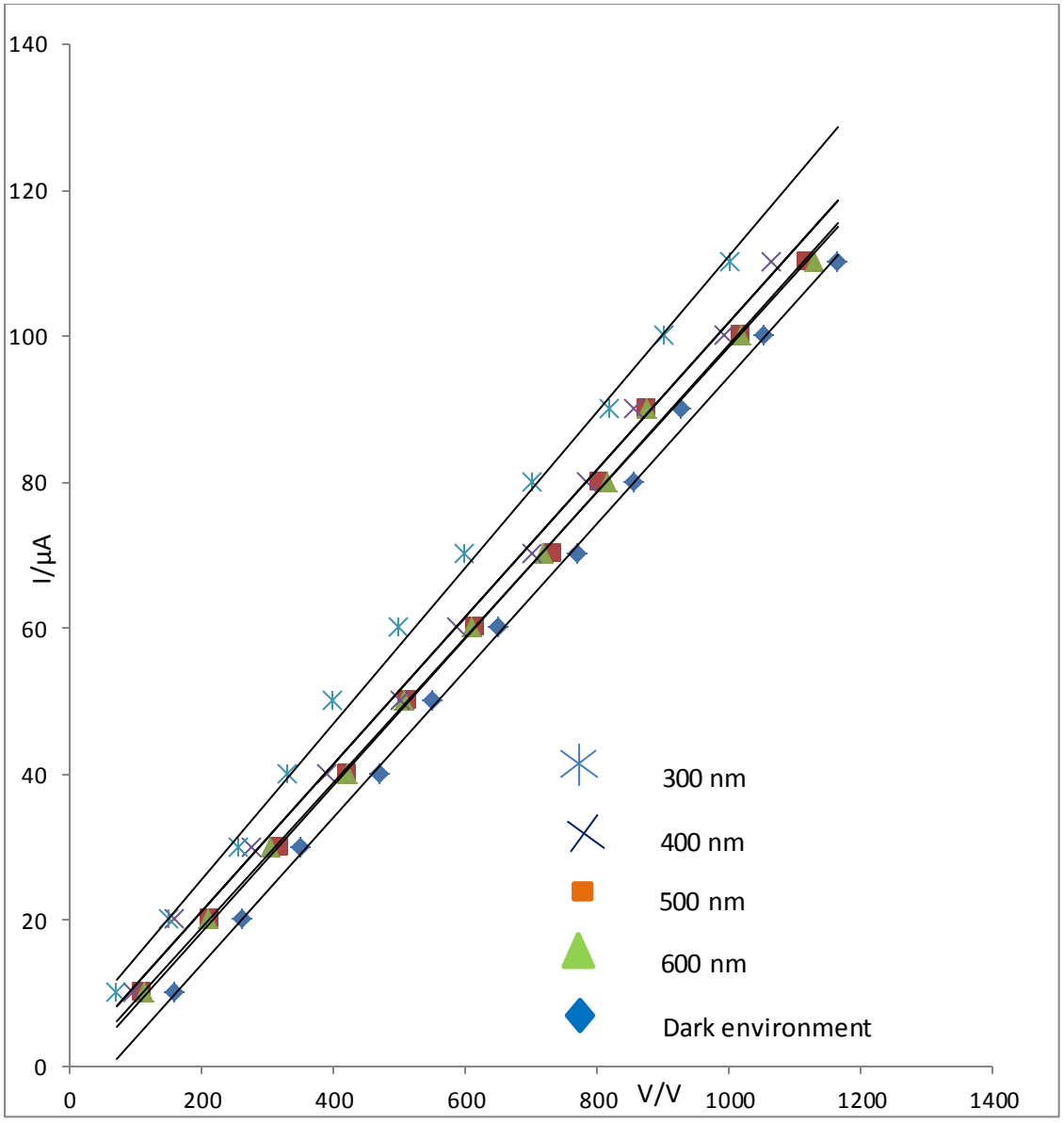

Figure44: I-V characteristics of the CuO thin film in (i) dark environment and(ii) when 300 nm – 600nm radiation is incident on it. This shows the linear part of the I-V used to dertermine the resistance of the material (i) in the dark environment and (ii) when the 300nm – 500 nm radiation was incident on the CuO nano particles.

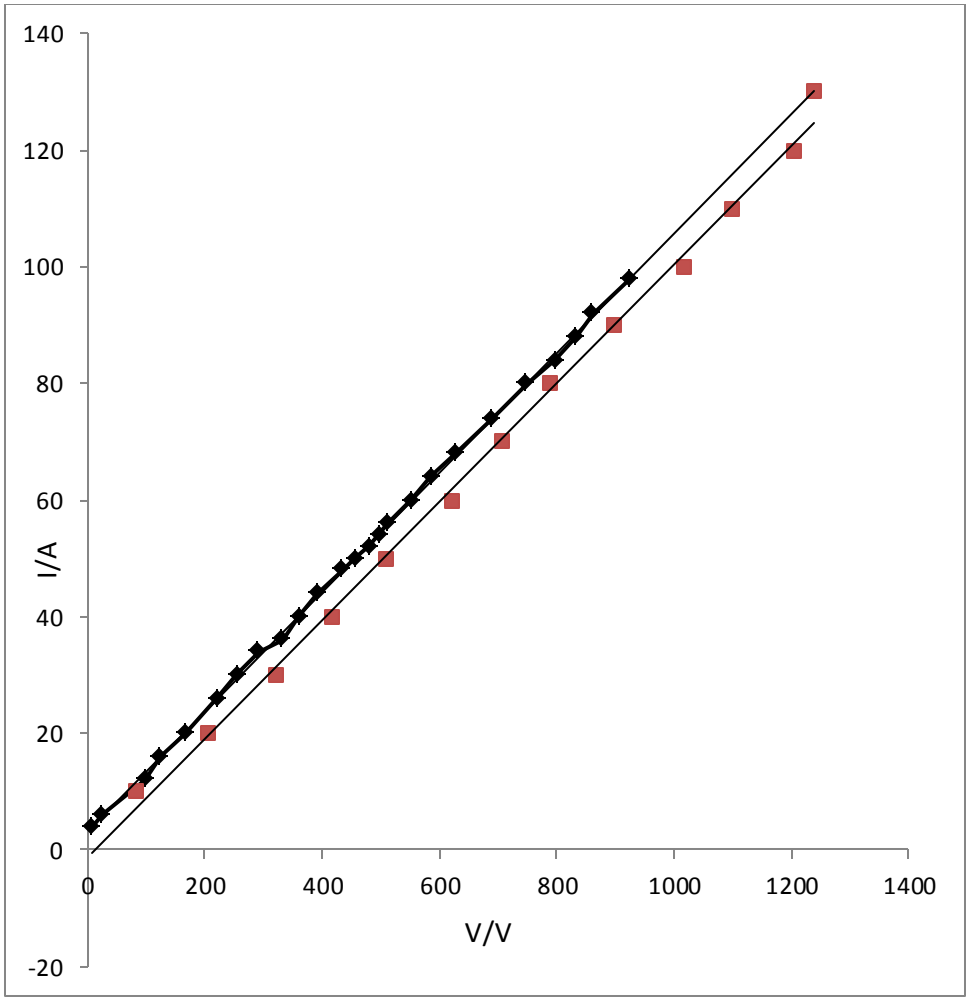

Figure45: I-V characteristics of the CuO thin film in (i) dark environment (22 ^{o}C) and(ii) when it is exposed to normal day light (28^{o}C). This shows the linear part of the I-V used to dertermine the resistance of the material (i) in the dark environment(22^{o}C) and (ii) when exposed to normal day light (28^{o}C).

From Figures44 and 45 the slope is the reciprocal of the sheet resistance of the CuO thin film. The reciprocal of the slope of the graphs therefore gives the resistance of the thin film.

$$\frac{1}{R_1} = 0.1027$$

$$R_1 = 9.737\ \text{MΩ}$$

$$\frac{1}{R_2} = 0.1021$$

$$R_2 = 9.794\ \text{MΩ}$$

$$R_1 - R_2 = 57.3\ \text{KΩ}$$

It should be noted that the current axis is in micro amps, that is what accounts for the final MΩ units of the final results for the resistance values from the graphs.

The film thickness: The film thickness was obtained by using Fizeau fringes as illustrated in the diagram in figure 24. The step at the junction between the film and the glass slide on which the film is deposited is replicated by the fringes. This method has an advantage over other means of finding film thickness in that there is only one source of error, which is in the reading of the vernier scale.

Several readings were taken and the average value determined to be the thickness of the film in order to reduce the margin of error associated with the reading of the vernier. The film thickness obtained would be used to calculate the resistivity and the conductivity of the film (CuO).

The resistance of the CuO thin film has been obtained from the IV plot and has been used to calculate the resistivity of the as prepared CuO nanoparticles using the formular [78];

$$\rho = \frac{R.b.t}{L}$$

where t is the thickness of the film, b is the copper electrodes width; L is the distance between the electrodes. Resistivity value obtained is $11.708\,\Omega$ cm . From the resistivity, the conductivity of the CuO nanoparticles was calculated to be

$$\sigma = 8.541 \times 10^{-2}\ \ \Omega^{-1}\text{cm}^{-1}$$

Current voltage measurements were also made on the CuO thin film in a dark environment to see how it compares with the IV characteristics of the same in light. The CuO thin film was illuminated with some wavelengths in the visible spectrum, that is, various wavelengths of visible radiation were selected and focused on the thin film, the corresponding current and voltage values were recorded accordingly. This would ascertain the suitability or otherwise of the material to be used for photovoltaic applications in addition to its absorbance properties. The IV characteristics of the sample for some wavelengths and the dark environment have been provided in figures 43 and 44.

From the I-V characterictics in figure 45, the resistance of the material to the flow of electric current of the material for the various incident wavelengths have been obtained and tabulated in table 8.

Wavelength /nm	Resistance / MΩ
300	9.52
400	9.54
500	9.73
600	9.76

Table 8: Table of incident wavelengths and the corresponding resistance values.

CHAPTER 5

DISCUSSION

The world energy need will be on the increase as long as the demand for the spread of modernization across the globe exists. Modernization and industrialization go hand in hand and both require reliable and sustainable energy systems. The cost of non-sustainable energy system is lack of economic growth which affects adversely the fight against poverty. An effective and efficient energy system should be one that is self-sustaining or with a source that is renewable [58, 59]. Disruptions in electricity supply takes a heavy toll on gross domestic product (GDP) in all economies. It is, therefore, imperative for identifying and inventing appropriate source and system(s) which have the potential of supporting constant supply of electricity for economic and social advancement.

The dependence of the world on traditional/ conventional sources of energy has brought about environmental pollution in proportions that are unprecedented in the history of human kind. In addition, these sources are non-renewable therefore making it inevitable for the world to look for alternative sources that hold the prospect of continuous and reliable power production for generations unborn[61]. The attempts at looking for alternative sources bring up opportunities in job creation adding to solving the unemployment situation that has bedeviled both the advanced and developing countries [59].

Solar energy has been identified as the most important renewable energy source in that it can be used in various ways to generate electrical power to promote various economic activities across the globe. Its use spans; open air drying, direct solar drying, indirect solar drying, solar cooking, solar water heating for domestic purposes, solar concentration for steam production, meant for turning steam turbines for electricity generation for industrial application, and photovoltaic application, where there is direct conversion of solar energy to electrical energy with the basic converting device being the solar cell.

There are different types of solar cells, these bear their names from the sort of materials used in the fabrication. Examples include; inorganic solar cells, organic solar cells, crystalline solar cells, amorphous solar cells, polycrystalline solar cells and monocrystalline solar cells.

Inorganic solar cells have been found to be more durable than organic solar cells. The former is able to withstand higher temperatures with very little or no degradation in a sharp contrast to organic solar cells which degrade with temperature. This characteristic of the inorganic solar cell has therefore induced so much interest among researchers in material science and renewable energy to identify inorganic materials which have the potential to be used in making solar cells and also come out with their synthesis routes.

In this work, CuO has been identified as an inorganic material with the potential of being used in the fabrication of solar cell. This is due to the fact that it has band gap range of between 1.0 – 1.5 eV which makes it suitable for photovoltaic applications

[61]. With a bad gap less than 2.0 eV and its photoconductivity and photochemical properties it is without a doubt a good candidate for solar cell fabrication.

The cost factor in the production of affordable energy which cannot be overemphasized has been the motivation for finding an inexpensive simple chemical route for the synthesis of CuO nanoparticles for photovoltaic applications. Nano particles and nanoparticle based devices have wide range of applications in industry due to their unique and overwhelming advantages they possess over their bulk counterparts. This to a very large extent is attributed to their large surface to volume ratio. [25]

Synthesis

A simple and inexpensive route has been used to prepare a black powder at a maximum temperature of 90 ^{o}C from copper sulphate and ammonium water, the reaction equation is as shown below. 0.01 M concentration of copper sulphate were mixed in volumetric ratio of 3: 1 and stirred vigorously with the help of a magnetic stirrer before placing the mixture on a preheated hot plate. Stirring continued throughout the two and half hour period when black precipitates were formed. The precipitates were dried on a hot plate at 50 ^{o}C after they had been thoroughly washed with ammonia water and then deionized water.

This powder has been subjected to various analysis techniques to ascertain whether or not the particles are of the nanoscale (10-100 nm) [62].

XRD measurements

Flat stage scanning of the powder has been done from 20^{o} to 90^{o} at 2θ using Empyrean Xray equipment at the Department of Physics.

The powder diffraction of the prepared sample produced acceptable results. These results point to the fact that the black powder produced is cupric oxide with crystallite size in the nano range. The high intensity peaks located at 35.5^{o} and 38.7^{o} corresponding to reflections from $\bar{1}11$ and 111 atomic planes compare well with data from literature as reported by ICSD, code: 67850. This points to the fact that the XRD measurements indicate a CuO phase for the sample. It is an indication that the as prepared sample is to a large extent pure cupric oxide, a material with a great potential for the photovoltaic industry.

Diffraction angle(θ^o) [2Th]		d-spacing Å		Atomic planes	FWHM	Grain size nm
Observed	Reported	Observed	Reported	Reported	Observed	Calculated
32.4354	32.480	2.75809	2.75440	1 1 0	0.5904	14.0601
35.4856	35.539	2.52769	2.52400	-1 1 1	0.3444	25.2954
38.6838	38.640	2.32575	2.30930	1 1 1	0.6396	13.7487
48.8764	48.852	1.86192	1.86280	-2 0 2	0.8856	10.2912
53.5889	53.355	1.70877	1.71570	0 2 0	0.5904	15.7442
58.2309	58.163	1.58312	1.58480	2 0 2	0.7872	10.5407
61.4033	61.517	1.50871	1.50620	-1 1 3	0.5904	14.052
66.0648	66.340	1.41310	1.40790	-3 1 1	0.9840	8.4327
68.2960	68.018	1.37227	1.377720	2 2 0	0.7872	12.7361
72.1657	72.339	1.30791	1.30520	3 1 1	0.9840	10.4338

Table 9: Presence of CuO phase in the synthesized sample and its comparative analysis of the diffraction angle, d-spacing between the observed and literature data calculated from ICSD using POWD-12++, (2004), collection code : 67850.

From table 9 above the grain sizes of the as-prepared cupric oxide nanoparticles as calculated using Scherer's formula, range from the minimum of 8.4327 nm to a maximum value of 25.2954 nm. The average grain size of the as-prepared cupric oxide nanoparticles has been calculated to be 13.53349 nm.

Absorbance measurements

Absorbance measurement done with the Shimadzu UVmini-1240 has shown that the as-prepared cupric oxide absorbs in the visible and the ultra violet region of the electromagnetic spectrum. The absorption peaks around 314 nm wavelength. This makes the as-prepared cupric oxide nanoparticle a good candidate for photovoltaic applications. From the absorbance measurements, the Tuac's relation has been used to determine the band gap energy for the as-prepared cupric oxide nanoparticles [86]. The estimated mean band gap energy for the as-prepared cupric oxide nano particles is 1.48 eV. This figure falls within the band gap range for the bulk (1.0 – 1.5 eV) as quoted by Koshy et al [61]. This value compares favourably well with the findings of [64, 65, 66, 67] who have reported bandgap values of CuO : 1.6 eV, 1.3 eV, 1.0-1.4 eV and 1.21-1.51 eV.

The band gap energy of 1.48 eV falls within the suitable energy range of 1.0 – 1.8 ev for photovoltaic applications. The as-prepared cupric oxide nanoparticles is therefore a good candidate for photovoltaic applications [68].

TEM measurements

The micrographs obtained have been used to estimate the average particle size range and the particle size distribution. The average particle size ranges from 5.6 – 55.6 nm, an indication of the fact the as-prepared cupric oxide is in the nanoscale [62].

A histogram of the particle size plotted against frequency shows that the size distribution is close to being normal with respect to the particle size scale. That notwithstanding is not enough to help with finding a mathematical formula to fit the distribution [34]. Cumulative percentage frequency curves have been constructed with linear and the logarithmic scales. It has been observed from the cumulative percentage frequency curves that the one with logarithmic scale is fairly straight in relative terms. This indicates that the particle size distribution of the cupric oxide nanoparticles is almost adequately described by Gaussian distribution. It then implies that the data acquired from the treatment of the microgram is not better described by a log-normal distribution formula as shown by the blue thick line in figures 41 and 42.

From the micrographs one of which has been shown in figure 37, the particles are fairly spherical

I-V characteristics

In order to ascertain the suitability of the as prepared CuO nanoparticles for photovoltaic applications, it became paramount for the resistive nature of the material to be investigated. For a material to be classified as semiconductor with the potential to be used to convert solar energy to electrical energy it should absorb strongly in the entire visible region or part of the visible region of the electromagnetic spectrum.

Such a material should also show rectifying property with metal in other words, it should form a Schottky diode with metal.

In attempting to investigate the above mentioned properties, a thin film of the material had to be prepared and connected in an electrical circuit for exposure to radiation and heat so that current and voltage measurements could be made. Various methods of

making thin film were employed: doctor blading, spin coating and chemical bath deposition. The chemical bath deposition gave the thin film suitable for the investigations. Though a lot of effort went into employing the other modes, they did not yield the desired results due to equipment failure and electrical power problems.

It was necessary to investigate the material at ambient temperature and also exposed to normal day light in the laboratory. Voltage and current measurements were made on the film under the above conditions and also when the material had been exposed to various frequencies in the visible region of the electromagnetic spectrum. Analysis of the results from the I-V characteristics gave very interesting outcomes. The film had a resistance of 9.741 MΩ at room temperature (28 ^{o}C) with normal day light which compares with Ooi et al [80] who obtained a resistance value of 120 MΩ under similar conditions. The resistivity value of 11.708 Ω.cm was also obtained, this falls within the range obtained by Kasim et al [83] who obtained these values: 4.1×10^{-6} Ω cm, 1.9×10^{-6} Ω cm, 127.51 Ω cm and 205.16 Ω cm. But it does not compare favourably with that obtained by Pierson et al [84] and Ooi et al [80] with a resistivity value of about 18 KΩ.cm. However, it is indicative of the fact that the CuO nanoparticles so obtained are resistive. The thin film of CuO was found to have a conductivity value of $8.541 \times 10^{-2}\ \Omega^{-1}\text{cm}^{-1}$.

It is also seen that the resistance values for the dark environment scenario was the highest followed by the 700 nm wavelength incident radiation. The lowest resistance value was obtained for 300 nm followed by 400nm wavelength incident radiation as seen in table 2. It is observed that the resistance values give an indication of strong absorption within the 300 nm and the 400 nm region agreeing with the absorption analysis of the as prepared CuO nanoparticles.

Apart from looking at the linear section of the I-V characteristic of the thin film, an attempt was also made to ascertain whether or not the film exhibit rectifying properties. The terminals of the power source were interchanged and current and voltage readings recorded. It appeared from figure 11 that there was a certain potential build up at the CuO thin film metal (copper) junction that had to be overcome. The I-V curve showed that after a certain point a small voltage corresponded to a large current pointing to the possibility of conquered potential leading to the avalanche of charge flow pointing to a rectifying situation. From the configuration used; two copper electrodes making contact with the thin film at the ends, suggest that both forward bias and reverse bias should provide similar results when the signs of current and voltage are reversed. The I-V curves in figures 43 and 44 agree with the anticipated outcome. From table 8, there is a clear trend of increasing resistance, from 300 nm incident radiation providing the lowest value through to 600 nm offering the highest value. This is an indication that the higher frequency radiation, frees more charge carriers and for that matter produce more current.

Chapter 6

CONCLUSION AND RECOMMENDATIONS

6.1 Conclusion

This work has successfully produced black cupric oxide nanoparticles with suitable properties an indication of its potential for photo electronic and photovoltaic applications from a simple chemical route. It has been shown that it is possible to synthesize inexpensive cupric oxide nanoparticles that are highly stable. The XRD analyses has shown that the black powder prepared has 100% CuO phase with the two highest peaks occurring at 35.5^{o} (2θ) and 38.7^{o} corresponding to reflections from the $\bar{1}11$ and 111 atomic planes of the crystallites..

From the XRD results and subsequent calculations, the average crystallite size ranges from 8.43 nm - 25.29 nm.

Samples of the prepared cupric oxide nanoparticles have average particle size range 5.5 nm – 55.6 nm, with the size distribution spreading almost evenly around the mean particle size on the particle size scale as shown by the analysis of micrograms from TEM measurements.

It has been determined that a log-normal function best describes, mathematically, the particle size distribution of the as-prepared cupric oxide nanoparticles.

The sample absorbs in the visible and ultra violet region peaking around 314 nm, making it a good candidate for photovoltaic applications. This value has a calculated standard error of ± 5.8.

The as prepared cupric oxide has a mean optical bandgap energy of 1.48 eV, with a calculated standard error of ± 0.05 eV which falls within the range of bandgap energies suitable for direct conversion of solar energy into electrical energy.

The sun delivers more energy to the earth than we require, therefore focusing a lot more attention on renewable energy is imperative. More so, in the context of fast depleting fossil fuel resources and global warming, with its attendant catastrophes, it makes sense to seriously consider solar power. This work has sought to make a contribution to the quest for finding suitable but inexpensive inorganic nanomaterials with the right properties for photovoltaic applications. The anticipated improved solar cell efficiency could make assess to green energy affordable to all in the nearest future.

The stable black thin film of CuO of 1.47 microns thickness was produced by the chemical bath deposition method at bath temperature of 54^{o}C in 46 minutes. The time for producing the film and the relatively low preparation temperature is a desired result that would assist in the production of green energy in an inexpensive way. Ray [78] produced CuO thin film at a preparation temperature of of between 450 ^{o}C and 500 ^{o}C by sol-gel-like dip technique. Niaval et al [79] prepared CuO thin film at a preparation temperature of about 500 ^{o}C by a sol-gel process. These processes were comparatively more energy intensive than ours. The thin film of CuO was used to determine the resistivity and the conductivity of the nanoparticles of CuO produced. These results show that the as-prepared material is resistive.

Resistance values obtained for the material in a dark environment and in normal day light in the laboratory showed that when photons are incident on the material it occasioned the decrease in resistance value from 9.931 MΩ to 9.741 MΩ.

The resistance values obtained for the thin film indicate that the material responds favourably to visible radiation especially between 300 nm and 400 nm, the region of highest absorption according to the absorption spectrum. Thin film has been used to obtain the resistivity of the material, $8.541 \times 10^{-2}\ \Omega^{-1}\text{cm}^{-1}$, indicative of the fact that the material is resistive. This makes the as- prepared CuO nanoparticles suitable for photovoltaic and photo electronic applications.

6.2 Recommendation

Scanning electron microscopy (SEM) measurements should be done on cupric oxide nanoparticles prepared using the simple chemical route, identified in this work, to confirm the spherical nature of particles and the particle size distribution. Comparison of XRD and SEM results would show whether or not the cupric oxide nanoparticles are single crystals.

Further investigations into the rectifying property and the resistivity of the as-prepared Cupric oxide nanoparticles by making hall effect measurements on the sample may help improve the preparation process which would result in producing quality semiconductor for improved solar cell efficiency.

Fabrication of an inorganic solar cell should be looked at from the as-prepared sample with an n-type material, say, ZnO, should be done, and I-V characteristic curve constructed for the cell so fabricated to determine the reliability or otherwise of the sample as a good candidate for photovoltaic applications. The solar cell so prepared should be made to undergo varying temperature exposure to verify its durability during operation.

REFERENCES

1. OpenStaxCollege, *CollegePhysics*, *OpenStaxCollege*, <http://cnx.org/content/col11406/latest/>, 2012, p. 253.
2. International Energy Agency, *Solar Energy Perspectives*, OECD Publishing, Paris, 2011.
3. International Energy Agency, *World Energy Outlook*, OECD Publishing, Paris, 2012.
4. D. R. Williams, Sun Fact Sheet. Available online: http://nssdc.gsfc.nasa.gov/planetary/factsheet/sunfact.html. Retrieved 26 November, 2014.
5. V. Smil, *Energy at the Crossroads: Global Perspective and Uncertainties*, MIT Press, Cambridge, MA, 2003, p. 240.
6. International Energy Agency, *World Energy Outlook*, OECD Publishing, Paris, 2013.
7. B. Das, S. Subramanium and M. R. Melloch, "Effects of electron-beam induced damage in back-gated GaAS/AlGaAs devices", *Semicond. Sci. Technol.* **8**, 1347 (1993).
8. C. Vieu, F. Carcenac, A. Pepin, Y. Chen. M. Mejias, L. Lebib, L. Manin Ferlazzo, L. Couraud, and H. Launois, "Electron beam lithography: resolution limits and applications ", *Appl. Surf. Sci.* **164**, 111 (2000).
9. A. N. Goldstein, C M. Echer, and A. P. Alivisatos, "Melting in semiconductor nanocrystals", *Science* **256**, 1425 (1992).
10. A. W. Adamson, *Physical Chemistry of Surfaces*, Wiley, New York, 1976.

11. G. Cao, *Nanostructures and Nanomaterials: Synthesis, Properties and Applications*, Imperial College Press, London, 2004.
12. L. R. Fisher and J. N. Israelachvili, "Experimental studies on the applicability of the Kelvin equation equation to highly curved concave menisci", J. Coll. Interf. Sci. **80**, 528 (1981).
13. J. C. Melrose, "Applicability of the Kelvin equation to vapor/liquid systemsin porous media" *Langmuir* **5**, 290 (1989)
14. R. W. Vook, "Structure and growth of thin films" *Int. Met. Rev*. **27**, 209 (1982)
15. A. C. Pierre, Introduction to Sol-Gel Processing. Kluwer, Norwell, M. A, 1998.
16. P. C Heimenz, *Principles of Colloid and Surface Chemistry*, Marcel Dekker, New York, 1977.
17. G. D. Partiff, in *Dispersion of Powders in Liquids with Special Reference to Pigments*, ed.G. D Parfitt, Applied Science, London, p.1, 1981.
18. C. J. Brinker and G. W. Scherer, *Sol-Gel Science: The Physics and Chemistry of Sol-Gel Processing*, Academic Press, San Diego, CA, 1990.
19. P. C. Hiemenz, Principles of Colloid and Surface Chemistry, Marcel Dekker, New York, 1977.
20. J. H. Gan, G. Q. Yu, B. K. Tay, C. M. Tan, Z. W. Zhao, Y. Q. Fu "Preparation and characterization of copper oxide thin films deposited by filtered cathodic vacuum arc," *J Phys D: Appl Phys* **37**, 81 (2004)
21. R. K. Swarnkar, S. C. Singh and R. Gopal " Synthesis of Copper/ Copper-Oxide Nanoparticles: Optical and structural characterizations," *AIP Conf. Proc*. **1147**, 205 (2009).

22. L. S. Huang, S. G. Yang, T. Li. B. X. Gu, Y. W. Du, Y. N. Lu, S. Z. Shi "Preparation of large scale cupric oxide nanowires by thermal evaporation method," *J Crystal Growth* **260**, 130 (2004).
23. S. C. Singh, R. K. Swarnkar, and R. Gopal " Synthesis of Titanium oxide Nanomaterial by Pulsed Laser Ablation in Liquid Media," *J nanosci. Nanotech.*, 9, 1, (2009).
24. S. C. Singh, R. K. Swarnkar, and R. Gopal, "Laser ablative approach for the synthesis of cadmium hydroxide-oxide nano-composite," *J nanopart. Res.*, DOI 10.1007/s11051-009-9696-9.
25. S. Panigrah, S. Kundu, S. K. Ghosh, S. Nath, S. Praharaj, B. Soumen and T. Pal, "Selective one-pot synthesis of copper nanorods under surfactantless condition" , *Polyhydron* 25, 1263 (2006).
26. J. Nikhil, L. W. Zhong, K. S. Tapan and P. Tarasankar, "Seed-mediated growth to prepare cubic copper nanoparticles", Curr. Sci. **79**, 1367 (2000).
27. C. J. Zhong, D. Mott, J. Galkowski, L. Wang and J. Luo, "Synthesis of size-controlled and shaped copper nanoparticles", *Langmuir* **23**, 5740 (2007).
28. S. Kapoor and T. Mukherjee, "Photochemical formation of copper nanoparticles in poly (N-vinylpyrrolidone)" *Chem. Phys. Lett.* **370**, 83 (2003).
29. H. H. Huang, F. Q. Yan, Y. M. Kek, C. H. Chew, G. Q. Xu, W. Ji and S. H. Tang, "Synthesis, characterization and nonlinear properties of copper nanoparticles" *Langmuir* **13**, 172 (1997).
30. C. M. Liu, L. Guo, H. B. Xu, Z. Y. Wu and J. Weber, "Seed-mediated growth and properties of copper nanoparticles, nanoparticle 1 D arrays and nanorods" *Microelectron. Engi.* **66**, 107 (2003).

31. R. Zhou, X. Wu, X. Hao, F. Zhou, H. Li, and W. Rao, "Influences of surfactant on the preparation of copper nanoparticles by electron beam irradiation" Nucl. Instrum. Method Phys. Res. B 266, 599 (2008).
32. I. Lisiecki and M. B. Pileni, "Synthesis of Copper metallic cluster using reverse micelles as microreactors", *J. Am. Soc.* **115**, 3887 (1993).
33. J. Tanori and M. P. Pileni, "Control of the Shape of Copper Metallic Particles by Using a Colloidal System as Template", *Langmuir* **13**, 639 (1997).
34. S. H. Wu and D. H. Chen, H. Zhou and H. Wan, *Mater. Sci. Eng. A* **415**, 156 (2006).
35. H. S. Nalwa, " Encyclopedia for Nanoscience and Nanotechnology", vol.1, American Scientific Publishers, 2004.
36. Z. L. Wang, " Characterization of Nanophase materials", Wiley-VCH Verleg GmbH, 2000.
37. B. Akbari, M. Pirhadi Tavandashti, and M. Zandrahimi, Particle size characterization of Nanoparticles – A practical Approach, *Iranian J. of Mat. Sci & Eng*. Vol. 8, Number 2, Spring 2011.
38. Engineered Materials Handbook: Ceramics and Glasses: Vol. 4, ASM International, 1991.
39. M. Staiger, M, P. Bowen, and J. Bohonek, " Particle size Distribution Measurement and Assessment of Agglomeration of Commercial Nanosized Ceramic Particles", J. Disper. Sci. Tech., 23,5,619, 2002.
40. J. L. Moll, *Physics of Semiconductors*, McGraw-Hill, pp. 32-52, 1964.
41. L. L. Kazmerski, *Polycrytalline and amorphous thin films and devices*, Academic Press, pp. 17-57, 1980.

42. R. F. Pierret, *Advanced semiconductor fundamentals*, Modular Series on Solid-State Devices, Vol. VI, Addison Wesley Publishing Company, p. 158, 1989.
43. A. S. Grove, Physics and technology of semiconductor devices, J. Wiley & Sons, pp. 129-134, 1967.
44. Bent Sorensen, Renewable Energy conversion, Transmission and Storage, Gilleleje, June, 2007
45. A. Einstien, Photoelectric effect, Annalen der Physik Scientific journal, 1905.
46. H. Kidowaki, T. Oku, T. Akyiyama, A. Suzuki, B. Jeyadevan and J. Cuya. "Fabrication and Characterization of CuO-based Solar Cells" *J. of Mat. Sc. Re.* Vol. 1, No. 1; Jan. 2012.
47. X. Wen, W. Zhang and S. Yang. Synthesis of $Cu(OH)_2$ and CuO Nanoribbon Arrays on a Copper Surface, *Langmuir* 19 (14) pp 5898 – 5903, ACS, 2003.
48. R. S. Patil *et al.* Photoluminescence properties of modified chemical bath deposited Copper Oxide thin film, Arch. Appl. Sci. Res., 3(2) pp 288-291, 2011.
49. L. Armelao et al. Thin Solid Films 442, Science Direct, pp 48 – 52, 2003.
50. A. Mateen. Some methodologies used for the synthesis of cuprous oxide- A review, J Pak Mater Soc. 2(1), 40 – 43, 2008.
51. V. Pandey, G. Mishra, S. K. Verma, M. Wan, and R. R. Yadav. *Synthesis and Ultrasonic investigations of CuO-PVA Nanofluid*, *Materials Sciences and Applications*, 3, 664 – 668, 2012.
52. K. Nithya, P. Yuvasree, N. Neelakandeswari, N. Rajasekaran, K. Uthayarani, M. Chitra and S. Sathiesh Kumar. *Preparation and Characterization of Copper Oxide Nanoparticles. Int. J. of ChemTech Research*. Vol. 6, No. 3, pp 2220 – 2222, may, 2014.

53. M. Suleiman, M. Mousa, A. Hussein, B. Hammouti, T. B. Hadda and I. Warad. J. Mater. Environ. Sci. 4(5), 792 – 797, 2013.

54. Y. Zou, Y. Li, N. Zhang and X. Liu. *Flower-like CuO synthesized by CTAB-assisted hydrothermal method*, Bull. Mat. Sci. No. 4, pp 967 – 971, July 2011.

55. M. R. Johan, M. S. M. Suan, N. L. Hawari and H. A. Ching. Annealing effects on the properties of copper oxide films prepared by chemical deposition, Int. J. Electrochem. Sci. 6, pp 6094-6104, 2011.

56. K. Kannaki, P. S. Ramesh and D. Geetha. *Hydrothermal synthesis of CuO nanostructure and their Characterizations*, Int. J. of Scientific & Engineering Research Vol. 3, Issue 9, 2012.

57. D. P. Volanti et al, *Synthesis and characterization of CuO flower-nanostructure processing by a domestic hydrothermal microwave*. Journal of Alloys and Compounds 459, pp 537 – 542, 2008.

58. J. Koshy, M. Soosen Samuel, A Chandran and K.C. George. Optical Properties of CuO Nanoparticles. AIP Conf. Proc.1391, 576-578, 2011.

59. P. Bowen, "Particle size Distribution Measurement from millimeters to nanometers and from Rods to Platelets" J. Disper. Sci. Tech, 5, 23, 631, 2002.

60. T. Allen., "Particle size Measurement, Chapman and Hall, 5th Edition", Vol. 1&2, 1997.

61. D. I. Stern, *The Role of Energy in Economic Growth*, CCEP Working papers, 2010.

62. World Economic Forum, Energy vision update, 2012

63. Renewable Energy.World.com

64. J. Koshy, S. Samuel, A. Chandran, and K.C. George. Phenomena, Materials, Devices and Characterization, AIP Conf. Proc. 1391, 576-578. 2011.

65. NANOSTRUCTURES AND NANOMATERIALS- Sythesis, Properties, and Applications (2nd Edition) World Scientific Publishing Pte Co Ltd.

66. T. X. Wang, S. H. Xu and F. X. Yang. Green synthesis of CuO nanoflakes from $CuCO_3.Cu(OH)_2$ powder and H_2O_2 aqueous solution, Powder Technology 228, 128-130, Elsevier, 2012.

67. I. A. Ezenwa. *Optical Analysis of Chemical bath Fabricated CuO Thin Films*, Res. J. Rescent Sci. Vol. 1(1), 46-50, 2012.

68. F. Marabelli, G. B.Paravicini, and F. Salghetti-Drioli, Optical gap of CuO, *Phys. Rev*. **B52**, 1433, 1995

69. D. Park and R. Sinclair, "Grain size analysis of longitudinal thin film media", J. Appl. Phys, 87,5687. 2000

70. D.T. Carpenter, J.M. Rickman, and K. Barmak, "A methodology for automated quantitative microstructural analysis of transmission electron micrographs", J. Appl. Phys. 84, 5843. 1998

71. A. A. Ogwu et al, "Electrical resistivity of copper oxide thin films prepared by reactive magnetron sputtering" JAMME, vol.24(1), Sept. 2007

72. T.J. Richardson, J. L. Slack, M. D. Rubin, Electrochromism of copper oxide thin films, Proceedings of the 4th International meeting on Electrochromism, Uppsala, 2000

73. Y. F. Chen, D. M. Bagnall, H. J. Koh, K.T. Park, K. Hiraga, Z. Q. Zhu and T. J. Yao. Plasma assisted molecular beam epitaxy of ZnO on c-plane sappire: growth and characterization, J. Appl. Phys., **84**, 3912, 1998

74. T. Minami, T. Yamamoto, and T. Miyata, Highly transparent and conductive rare earth-doped ZnO thin films prepared by magnetron sputtering, Thin Solid Films, 366, 63, 2000

75. F. Ren, C. Z. Jiang, and X. H. Xiao, Fabrication of single-crystal ZnO film by Zn ion implantation and subsequent annealing, Nanotechn.,18, 285609, 2007
76. Y. Ma, G. Du, J. Yin, T. Yang, and Y. Zhang, Influence of the processing conditions on the structural properties of ZnO layers obtained by PECVD, Semicond. Sci. Techn., 20, 1198, 2005
77. Y. Kokubun, H. Kimura and S. Nakagomi, Preparation of ZnO Thin Films on Sapphire Substrates by Sol-Gel Method, Jpn. J. Appl. Phys., 42, L904, 2003
78. S. C. Ray, Preparation of copper oxide thin film by the sol-gel-like technique and study of their structural and optical properties, Solar Energy Materials and Solar Cells 68, 307 – 312 , 2001
79. S. S. Niavol and F. E. Ghodsi, Effect of pH on the Properties of Nanocrystalline CuO Thin Films Deposited by Sol – Gel Process, Russian Journal of Physical Chemistry A, vol 87, No 1,84 – 87, 2013
80. P.K. Ooi et al, Characterizations of Cupric Oxide thin Films on Glass and Silicon Substrates by Radio Frequency Magnetron Sputtering, Sains Malaysiana 43 (4) 617 – 621, 2014
81. P.Mallick and S. Sahu, Structure, Microstructure and Optical Absorption Analysis of CuO Nanoparticles Synthesized by Sol-Gel Route, Nanoscience and Technology , DOI: 10.5923/j.nn,2(3) 71 – 74, 2012
82. A. Umer, S. Naveed, N. Ramzan and M. S. Rafique, Selection of Suitable method for the synthesis of copper nanoparticles. Brief Rep. Rev., 7: 1-18, 2012
83. Kasim et al, "Effect of temperature on the properties of copper oxide thin films prepared by thermally oxidized evaporated copper thin films" IOSR-JAP, Vol. 3, Issue 2, 61 – 66, 2013

84. J. F. Pierson, A. Thobor-Keck and A. Billard, "Cuprite, paramelaconite and teronite films deposited by reactive magnetron sputtering" Applied Surface Science, volume 210, issues 3- 4, 359 – 367, 2003

85. S. Tolansky " Multiple Beam Interferometry of Surface and Films" Oxford University Press, Fair Laun, NJ, 1948.

86. J. Tauc "Amorphous and liquid semiconductors" Plenum, New York, 159, 1974.